N° d'ordre : 473

École Doctorale Mathématiques, Sciences de l'Information et de l'Ingénieur

UdS – INSA – ENGEES

THÈSE

présentée pour obtenir le grade de

Docteur de l'Université de Strasbourg
Discipline : Electronique
Spécialité : Télédétection

par

Yuyun BI

Estimation de l'évapotranspiration de surface terrestre à partir des données satellitaires

Soutenue publiquement le 25 Janvier 2010

Membres du jury

Directeur de thèse :	M. Zhao-Liang Li, CR1, CNRS
Co-Directeur de thèse :	M. Bin Xu, Professeur, IARRP/CAAS
Rapporteur externe :	M. Xiaoguang Jiang, Professeur, GUCAS
Rapporteur externe :	M. Liangfu, Chen, DR, IRSA
Examinateur :	Mme. Françoise Nerry, CR1, CNRS
Examinateur :	M. Jihad Zallat, Professeur, UdS
Examinateur :	M. Guangjian Yan, Professeur, BNU
Examinateur :	M. Daolong Wang, DR, IARRP/CAAS

LSIIT **UMR7005**

Acknowledgements

As this thesis is approaching the end, I would like to express my sincere gratitude to all my supervisors, classmates, colleagues, and friends who have supported and helped me during the period of my study for a doctorate.

First, I would like to thank particularly my two supervisors – Dr. Li Zhao-Liang and Prof. Xu Bin who have had hard task to direct my doctoral work. Many exchanges with them have guided my first steps in the field of remote sensing, and then allowed me to appreciate their availability and kindness. A few lines here can not be enough to express my sincere gratitude to them.

I would like to express my gratitude to Prof. Jiang Xiaoguang and Prof. Chen Liangfu to have accepted the hard task of external reviewer of this thesis.

My gratitude then goes to my classmates, particularly to Dr. Tang Bohui, Mr. Tang Ronglin, Dr. Zhang Xiaoyu and Dr. Ma Lingling for having provided me a lot of valuable information and assistances. Many new ideas proposed and developed in this thesis are the fruits of the collaboration with them. Without their collaboration, this thesis would not be as it is.

I am very grateful to the head of TRIO (Télédétection Radiométrie Imagerie Optique) in University of Strasbourg, Dr. Françoise Nerry, for her helpful attitude in solving many administrative affaires and to Prof. Jihad Zallat, both for having accepted to travel so long distance from France to China to attend my doctoral defense.

Grateful thanks are given to Prof. Yan Guangjian for taking time out of his busy lives to attend my doctoral defense.

Thanks are given to my friends known in Strasbourg. I spent lots of happy time with them, and I will never forget them. I would like to thank especially Mr. Shen Qingfeng for having given me a lot of warm-hearted help during my stay in France and after I came back to China.

Then I would like to express my gratitude to the heads of all offices at the Institute of Agricultural Resources and Regional Planning (IARRP) for their supports and help that I can keep my work and study in balance. I am very thankful to Director of the IARRP - Prof. Wang Daolong for the moral and spiritual encouragements. Thanks are given to my Chinese colleagues Mr. Gao Chunyu, Dr. Wang Yajing, and Dr. Li Gang. During my stay in France, they have helped me with a great deal of routine work and certain research tasks. Gratitude is also expressed to Director Chen Yinjun and all my colleagues of the Resource Management and Utilization Research Office for having showed me the warmth of a big family through team work.

I would also say thanks to all of my friends. It is difficult to quote everyone here. I simply make a point of saying that I appreciate everyone who helped me or gave me spirit supports.

Finally, I need to thank my family members. All I have belongs to you. I love you all.

This work was partly supported by the project EAGLE (Exploitation of AnGular effects in Land surfacE observations from satellites) through contract No.: SST3 CT2003 502057 in the Sixth Framework Program (FP6) of EU and partly funded by the National Natural Science Foundation of China under Grant 40425012 and 40871169.

Contents

Estimation de l’évapotranspiration de surface terrestre à partir des données satellitaires

(Résumé)

Au début du 21ème siècle, le réel problème écologique est le changement climatique global.. Le réchauffement global de la terre, les catastrophes naturelles comme les extinctions d'espèces en sont les conséquences surtout si le changement climatique se produit trop rapidement. Le pannel intergouvernemental sur le changement climatique (PICC) a été établi par l'organisation météorologique mondial (WMO) ainsi que par le programme d'environnement des Nations Unies (UNEP) en 1988 pour évaluer le risque du changement climatique provoqué par les activités humaines. L’évapotranspiration (ET) joue un rôle important en hydrologie, météorologie et agriculture, comme dans la prévision et l'estimation de ruissellement de l'eau à l’échelle régionale, dans la simulation de la circulation atmosphérique à grande échelle et du changement climatique global ainsi que dans l'établissement des programmes d’irrigations.

Globalement, l’ET moyenne de la surface terrestre explique 60% de la précipitation moyenne. Il est donc nécessaire d’avoir une information fiable de l’ET de la surface terrestre pour prévoir les catastrophes naturelles telles que les inondations et les sécheresses. Cependant, l’ET de surface terrestre, qui est aussi importante que la précipitation et l'écoulement dans la modélisation du cycle d’eau, est l'une des composantes la moins renseignée du cycle hydrologique. L’estimation précise de l’ET régionale dans la modélisation du bilan hydrologique et du bilan énergétique à différentes échelles temporelles et spatiales est essentielle dans l'hydrologie, la climatologie et l'agriculture.

La technologie de la télédétection est identifiée comme le seul moyen viable de cartographier l’ET de la surface terrestre à l’échelle régionale de façon globale, cohérente et économiquement raisonnable. La combinaison des paramètres de surface dérivés des données satellitaires avec des variables météorologiques de surface et des caractéristiques de végétation permet d’estimer l’ET à l’échelle régionale et globale. La télédétection peut fournir la distribution spatiale et l'évolution temporelle des paramètres de surface tels que NDVI, LAI (Leaf Area Index), Albédo dérivés des données visibles et proche infrarouges et la température et l’émissivité de surface restituées à partir des données infrarouge thermiques. La plupart de ces paramètres est indispensable aux méthodes et aux modèles utilisés pour estimer l’ET de surface.

La potentialité d'utilisation des données infrarouges thermiques à partir de l'espace pour estimer l’ET à l’échelle locale et régionale a été intensivement étudiée pendant les 30 dernières années et des progrès substantiels ont été accomplis. Les méthodes varient dans leurs complexités, de la régression empirique simplifiée aux modèles physiquement basés sur du bilan énergétique, sur le triangle construit par la température de surface (Ts) et l’indice de végétation (VI), et aux techniques d'assimilation de données à un modèle numérique. Cependant, la télédétection satellite ne peut pas fournir des variables proches de la surface telles que la vitesse du vent, la température de l'air, l'humidité, etc., ce qui limite les applications de l'équation du bilan énergétique aux surfaces homogènes. De plus, les approches pour déterminer l’ET de surface terrestre diffèrent considérablement dans la complexité de la structure des modèles, dans les entrées et sorties des

modèles et dans les avantages et les inconvénients de chaque modèle. Par conséquent, en considérant les caractéristiques des diverses méthodes de détermination de l'ET développées pendant les décennies passées et l''importance de l'ET pour les hydrologistes, les études de ressource en eau et les ingénieurs en irrigation, la façon de calculer ou d'estimer avec précision l'ET à l'échelle régionale, en se basant sur la technologie de la télédétection, est devenu une question cruciale.

Ce travail porte donc sur l'élaboration et la mise au point de méthodes permettant de déterminer l'évapotranspiration régionale de surface terrestre à partir des données de l'instrument MODIS embarqué sur les satellites polaires Terra et Aqua. Il s'inscrit dans le projet EAGLE (Exploitation of AnGular effects in Land surfacE observations from satellites) retenu et financé par la Commission Européenne dans le cadre du programme FP6 pour une période de 3 ans et demi à partir du 1er février 2004. et dans le projet « Estimation des paramètres de surface à partir des données satellitaires » retenu et financé par le Ministère de la Science et de la Technologie Chinois pour une période de 3 ans à partir du 1er décembre 2006.

Cette thèse comprend 6 chapitres.

Dans le premier chapitre, nous présentons l'état de l'art sur l'estimation de l'évapotranspiration régionale à partir des données satellitaires. Une vue d'ensemble des modèles utilisant des données satellitaires est décrite pour en permettre l'analyse et la critique dans l'estimation de l'ET régionale à partir des données de l'espace. Généralement, ces modèles varient considérablement dans leurs entrées, dans leurs hypothèses principales et l'exactitude de leurs résultats. Sans compter l'utilisation des données satellitaires multispectrales du visible au infrarouge thermique, la plupart des modèles doit avoir recours dans une certaine mesure à des mesures auxiliaires au sol afin d'estimer les flux de chaleur turbulentes à l'échelle régionale. Nous discutons en détail les entrées, les hypothèses, la théorie, les avantages et les inconvénients principaux de chaque modèle dans ce chapitre. De plus, les approches de l'extrapolation de valeur instantanée ET aux valeurs quotidiennes sont également brièvement présentées. A la fin de ce chapitre, nous analysons les problèmes et perspectives associés aux modèles d'ET afin de montrer objectivement leurs limitations et les aspects prometteurs de l'estimation de l'ET régionale et nous décrivons brièvement la structure de cette thèse.

Le deuxième chapitre de cette thèse est consacré à la détermination de la température de surface terrestre (LST) à partir des données du satellite Chinois de type géostationnaire – FengYun 2C (FY-2C). La température de surface est en effet un paramètre commun à plusieurs thématiques et sa connaissance donne des informations sur les variations spatio-temporelles de l'état d'équilibre de surface. De ce fait, elle est reconnue comme un des paramètres prioritaires et fait l'objet d'attentions particulières dans l'étude de notre environnement et dans l'estimation de l'ET. Pour obtenir une analyse régionale et globale, la télédétection infrarouge thermique est donc un outil extrêmement intéressant. La télédétection IRT a essentiellement pour objectif la mesure de la température et de l'émissivité de surface. En se basant sur la théorie du transfert radiatif, ce chapitre adresse l'estimation de la température de surface terrestre à partir des données dans les deux canaux infrarouges thermiques (IR1, 10.3-11.3µm et IR2, 11.5-12.5µm) embarqués sur le satellite météorologique Chinois de type géostationnaire – FengYun 2C et en utilisant l'algorithme de type split-window généralisé (GSW). Les coefficients de l'algorithme de GSW correspondant à une série de variation de l'émissivité moyenne, du contenu de vapeur d'eau atmosphérique et de la température de surface ont été dérivés par une méthode statistique de régression en utilisant les valeurs numériques simulées avec un modèle de transfert radiatif atmosphérique précis (MODTRAN 4) sur une grande variation de conditions atmosphériques et des surfaces. Ce chapitre est décomposé en 3 parties. La première décrit la théorie liée à la détermination de la température de surface par l'algorithme de type GSW et présente le développement de l’algorithme pour les données de FY-2C. La seconde donne les résultats et les valeurs numériques des coefficients de l'algorithme de GSW. L’erreur sur la température de surface produite par l'incertitude des émissivités de surface, du contenu de vapeur d'eau dans l'atmosphère et du bruit instrumental est également présentée dans cette partie. En outre, afin de comparer les différentes formulations d’algorithmes de type split-window, les températures de surface estimées par plusieurs algorithmes récemment proposés dans la littérature sont comparées et analysées. La troisième partie présente les principaux résultats obtenus de ce travail et montre que la température de surface pourrait être estimée par l'algorithme de GSW avec écart type de l'erreur (RMSE) de moins de 1 K pour l'angle de visée zénithal (VZA) < 30 degré ou pour les conditions dans lesquelles le VZA et le contenu de vapeur d'eau atmosphérique sont respectivement inférieures de 60 degré et de 3.5 g/cm2 à condition que les émissivités de surface soient connues. Le résultat de l'intercomparaison a prouvé que la plupart des algorithmes donnent des résultats comparables.

Nous abordons dans le troisième chapitre la restitution de l’émissivité directionnelle de surface à partir d’une combinaison des données infrarouge thermique (TIR) et infrarouge moyenne (MIR) de MODIS en mettant l’accent sur la modélisation de la réflectivité bidirectionnelle de surface terrestre dans le canal MIR. Jusqu’à ici, de nombreuses fonctions de distribution de réflectivité bidirectionnelles (BRDF) ont été développées pour décrire la réflectivité bidirectionnelle dans des canaux visible et proche infrarouge en fonction des géométries d'illumination et d’observation. Les modèles semi empiriques à noyaux ont été appliqués avec succès avec les instruments AVHRR, MODIS et MISR. Très peu de travaux se sont concentrés sur le développement du modèle BRDF dans la région MIR, mais tous ont visé à estimer l'émissivité dans MIR à partir de la réflectivité bidirectionnelle dérivée des données AVHRR et MSG/SEVIRI. Notre travail est ici consacré à estimer l'émissivité directionnelle de surface terrestre dans les canaux TIR et MIR à partir de la réflectivité bidirectionnelle dérivée des données de MODIS dans les deux canaux adjacents de MIR de MODIS. La première partie de ce chapitre décrit la méthodologie pour déterminer l'émissivité directionnelle et le développement du modèle BRDF dans la région MIR. La seconde partie décrit la zone d'étude, les données MODIS et la procédure pour avoir l’estimation de l’émissivité directionnelle à partir des données MODIS. La troisième partie présente certains résultats préliminaires et la validation indirecte de ces résultats avec le produit de la température et de l’émissivité de surface de MODIS (MYD11B1). Dans ce travail, dix jours de données MODIS entre le 12 Juillet et le 30 Juillet de 2005 en condition du ciel clair au moment du passage de satellite sur la région étudiée ont été sélectionnés pour déterminer les coefficients de trois paramètres du modèle BRDF développé. Les émissivités directionnelles dans le canal MIR ont été déterminées sur une région de l'Egypte et de l'Israël avec la latitude variant de 28.0N à 32.0N et la longitude de 30.0E à 36.0E. Les résultats de la comparaison entre les émissivités dans le canal MIR obtenues de notre modèle avec celles de produit MODIS (MYD11B1) ont montré que, au moins pour notre cas d’étude, la méthode proposée pour estimer l'émissivité directionnelle donne des résultats comparables à ceux du produit MODIS (MYD11B1) avec une erreur moyenne de -0.007 et un écart type de 0.024.

Le quatrième chapitre se rapporte à l’étude de l’impact de l’'hétérogénéité spatiale de LAI sur l'estimation de la fraction directionnelle d'espace (directional gap fraction). La probabilité directionnelle d'espace ou la fraction d'espace est un paramètre de base dans la modélisation du transfert radiatif dans le couvet végétal. Bien qu'on ait proposé quelques approches pour estimer cette probabilité d'espace à partir des mesures satellitaires, peu d'efforts ont été mis sur l'étude des effets de changement d'échelle sur ce paramètre. De ce fait, nous analysons dans ce chapitre l'effet de changement d'échelle sur ce paramètre en agrégeant la probabilité directionnelle d'espace estimée à partir de LAI dérivé du satellite à haute résolution spatiale à l'aide de la loi Beer et nous avons introduit un nouveau paramètre $\hat{C}$ pour compenser l'effet de changement d'échelle de ce paramètre. La première partie de ce chapitre fournit le cadre théorique pour estimer l'effet de changement d'échelle de la probabilité directionnelle d'espace introduit par deux différents schémas d'agrégation, de l'échelle locale à la plus grande échelle. Dans la deuxième partie, nous présentons les différents types d'images de LAI obtenues à partir des données satellitaires de haute résolution spatiale de la base de données de la campagne-VALERI et dans la troisième partie, nous donnons l'effet de changement d'échelle lié à la non linéarité entre LAI et la probabilité d'espace sur plusieurs types de paysage et proposons un nouveau paramètre $\hat{C}$ pour compenser l'effet de changement d'échelle.

Les résultats obtenus de ce travail montrent que l'effet de changement d'échelle dépend non seulement de l'hétérogénéité de surface et aussi du degré de non linéarité de la fonction qui relie le paramètre recherché aux mesures (paramètres connus). Des expressions analytiques pour compenser l'effet de changement d'échelle de la probabilité d'espace sont établies en fonction de la variance de LAI et de la valeur moyenne de LAI dans un grand pixel. Avec l'ensemble des données de VALERI, l'étude dans ce chapitre prouve que l'effet de changement d'échelle de la probabilité d'espace augmente avec la résolution spatiale décroissante pour la plupart de types d'occupation du sol. Un effet relatif important est trouvé pour la plupart des sites de récoltes et pour un site mixte de forêt dû à leur grande variabilité vis-à-vis LAI, alors qu'un effet plus réduit se produit sur des sites de prairie et d'arbustes. Quant au nouveau paramètre $\hat{C}$, il varie lentement dans les sites de forêt, de prairie et d'arbustes, et de manière significative dans les sites de récoltes et de forêt mixte.

Le cinquième chapitre est consacré à l'estimation de l'ET régionale à partir des données MODIS sur des régions arides et semi-arides. Les objectifs de ce travail sont doubles: (1) développement d'un algorithme opérationnel pour déterminer quantitativement les limites sèche et humide dans l'espace triangulaire construit par la température de surface (Ts) et l'indice de végétation (VI) sur des régions arides et semi-arides où des pixel humides généralement ne sont pas facilement identifiés, (2) validation de l'ET dérivé des produits de MODIS/TERRA avec l'ET mesurée par l'instrument LAS (Large Aperture Scintillometer). La première partie de ce chapitre rappelle le principe de la méthode de triangle Ts-VI et met en avant les hypothèses impliquées dans l'élaboration méthodologique ainsi que les avantages et les inconvénients de la méthode de triangle Ts-VI. La seconde partie est consacrée au développement d'un algorithme pratique pour la détermination quantitative des limites sèche et humide dans le triangle Ts-VI. Cet algorithme peut fournir une estimation du rayonnement net, du flux dans le sol, de la fraction évaporative et de l'ET à l'échelle régionale à partir uniquement des données et des produits de MODIS. La troisième partie décrit la région d'étude et les données utilisées dans cette étude et donne une validation préliminaire de flux de chaleur sensible dérivé des données MODIS avec les mesures sur le terrain faites par l'instrument LAS pendant l'expérience sur le terrain de Heihe du 20 mai au 21 août 2008. Les résultats montrent que les flux de chaleur sensible dérivés des données MODIS par notre méthode sont en bon accord avec ceux mesurés à partir du LAS. L'écart type de cette comparaison est de 25.07 W/m^2.

Le sixième chapitre est la conclusion de cette thèse. Ce travail a permis de montrer l'avantage de la méthode de triangle Ts-VI par rapport aux autres méthodes traditionnellement utilisées pour la détermination de l'évapotranspiration régionale et de proposer des méthodes permettant de calculer la température de surface et l'émissivité de surface à partir des luminances mesurées par les satellites. Ce travail a aussi montré qu'il était possible d'estimer l'ET sur des régions arides et semi-arides à partir uniquement des données satellitaires avec une précision acceptable.

Ce travail ouvre des perspectives intéressantes. Dans la restitution de l'ET régionale, l'exactitude de cette restitution dépend principalement de l'exactitude de la détermination quantitative des limites sèche et humide dans le triangle Ts-VI et de la performance du modèle d'interpolation impliqué dans l'évaluation de la fraction évaporative dans le modèle de l'estimation de l'ET. Les performances du modèle et du nouveau algorithme développé dans cette étude devront donc être évaluées de façon précise et attentive.

La détermination des limites sèche et humide dans l'espace de triangle Ts-VI implique généralement un grand degré de subjectivité et d'incertitude. Les règles et l'algorithme proposés dans cette thèse proposent un outil réaliste pour estimer la température de surface la plus élevée à chaque intervalle de la fraction du couvert végétal et de déterminer ensuite les limites sèche et humide dans l'espace de triangle Ts-VI sur des régions arides et semi-arides. Bien que l'hypothèse d'interpolation linéaire en deux étapes impliquée dans l'estimation de la fraction évaporative soit encore incertaine et non encore vérifiée directement, un très bon accord est trouvé quand le flux de chaleur sensible déterminé à partir des données MODIS est comparé à celui mesuré par l'instrument LAS. Pour réduire l'incertitude dans l'estimation des flux de chaleur turbulents par la méthode Ts-VI, d'autres travaux doivent être menés à bien pour vérifier les paramètres/variables appropriés étape par étape à condition que les données nécessaires soient alors disponibles. De plus un travail de validation doit être effectué dans d'autres régions climatiques pour l'algorithme proposé.

地表蒸散发遥感估算

（摘 要）

全球气候变化是当今人们最为关注的环境问题之一。随着全球气候变暖，冰川消融、海平面上升、飓风、海啸、洪涝、干旱、物种灭绝等自然灾害在世界各地时有发生。早在 1988 年，联合国环境规划小组（United Nations Environment Programme，UNEP）与世界气候组织（World Meteorological Organization，WMO）就成立了联合国政府间气候变化专家委员会（Intergovernmental Panel on Climate Change，IPCC）(http://www.ipcc.ch/about/index.htm)，主要评价人类活动所导致的气候变化的风险性。蒸散发（EvapoTranspiration，ET）作为生物圈、大气圈、土壤圈和水圈之间水分循环和能量传输的控制因素，在水文学、气象学、农学、地学等学科研究中，如区域尺度的地表水和地下水预测和估算、大尺度的大气环流和全球气候变化模拟、田间尺度的农田灌溉和耕作管理等等方面，都发挥着重要的作用。

从全球来看，地表 ET 约占平均降水量的 60％。因此，在开展水灾、旱灾等自然灾害预测、气象预报和气候变化建模等各项工作过程中，十分有必要掌握可靠的地表 ET 信息。然而，地表 ET 作为水循环模型的必要组分，与降水、径流居于同等重要的地位，但却在水循环研究中较少被人认识。综合考虑过去数十年 ET 估算方法研究的局限性及其在水文学、水资源研究、灌溉工程学和气象学等方面所具有的重要作用，如何开展区域尺度 ET 估算和如何开展基于遥感技术的 ET 精确估算，已经成为 ET 应用和研究领域的热点问题。

本论文共有六章，主要倾注于区域 ET 遥感估算方法的研究。 论文首先对区域 ET 遥感进行了综合评述，继而在此基础上，根据区域 ET 研究的现实需要及其存在的主要问题，着重开展了四个方面的研究，包括地表温度（Land Surface Temperature, LST）反演研究、地表方向比辐射率遥感反演研究、叶面积指数（Leaf Area Index , LAI）空间异质性对方向性空隙度遥感估算影响研究、区域 ET 全遥感估算模型研究。最后是本论文的基本结论和区域 ET 遥感研究的发展展望。

论文第一章为区域 ET 遥感研究综述。本章对区域 ET 遥感研究进展尤其是模型发展进行了全面回顾，并对现有区域 ET 遥感估算模型的主要特征及其优缺点进行了系统的比较分析和综合评述。文章指出：要制作全球系统的、区域尺度和中尺度的 ET 分布图，遥感技术被认为唯一可行的手段。相比常规的“点”测量，遥感技术有几个显著的优势：1)可在几分钟内提供范围的空间覆盖信息；2) 获得同等空间信息的成本较低；3) 可实现难以开展人工作业的区域测量。利用遥感手段，在可见光和近红外波段可获取不同空间和不同时间的植被指数(Normalized Difference Vegetation Index，NDVI)、LAI、地表反照率(Surface Albedo)等，在中红外（Middle InfreRed，MIR）和热红外（Thermal InfraRed，TIR）波段可获取相应的地表比辐射率(Land Surface Emissivity，LSE)和地表辐射温度(Radiometric Surface Temperature，RST)等。一方面，地面温度等参数遥感反演，有助于直接建立地表辐射与地表能量平衡各组分之间的关系；另一方面，把遥感反演的地面参数与地面气象数据、植被特征等有关数据结合起来，可有效地开展区域性到全球性 ET 的评估。也就是说，为了利用模型把有效能量区分为显热通量和潜热通量，上述参数在模型中往往是必不可少的。

在过去 30 年中，已经开展大量的利用空间 TIR 数据进行区域和局域 ET 估算的研究，并取得重大研究进展。总体而言，普遍应用的遥感 ET 方法主要有两种，即（半）经验方法和分析方法。利用各种方法对土壤－植被－大气系统的热传导和水传输进行模拟，从简单的经验回归方程到基于地表能量平衡的物理模型、 地表温度－植被指数(surface Temperature - Vegetation Index，Ts-VI)三角形/梯形特征空间法，再到数据同化技术，最后到 ET 的时空尺度转换，其复杂程度、假设条件、数据输入以及估算结果的精确性等方面都大不相同，而且通常与某些数字模型结合在一起应用。地表能量平衡控制着土壤-植物-大气系统中水分交换和地表湍流通量在感热和潜热两个方面的分配。地表能量平衡残差法是在不同时空条件下绘制 ET 图时最广泛应用的方法，主要由两大类模型即单源模型和双源模型构成。就单源模型而言，地表能量平衡残差法各类模型的主要区别在于怎样估算感热通量 H，相应的模型主要有“地表能量平衡指数”（Surface Energy Balance Index，SEBI)模型、“地表能量平衡系统”（Surface Energy Balance System，SEBS）模型、“简化 SEBI”（Simplified Surface Energy Balance Index，S-SEBI）模型、“陆面能量平衡算法”（Surface Energy Balance Algorithm for Land，SEBAL）模型、“内化校准高分辨率 ET 制图” (Mapping EvapoTranspiration at high Resolution with Internalized Calibration，METRIC)模型和 VI-Ts 三角形/梯形特征空

间法等。ALEXI (Atmosphere-Land Exchange Inverse) 模型是双源能量平衡模型的代表，在空间分辨率 5-10km 的陆地尺度下该模型被认为是一种切实可行的地表通量估算方法。数据同化技术已经成为提高遥感数据利用价值的有效手段。遥感 ET 模型所得到的结果大多数为瞬时 ET 值，在水文学和水资源管理应用中，需要将其转化为每天或更长时间的 ET 值。ET 时间尺度转换的方法主要有正弦函数法、恒定蒸发比(Evaporaion Fraction，EF)法、恒定参考 ET 比值(reference ET Fraction，ETrF)法。

在综合评述的基础上，本章对现有区域 ET 遥感估算模型所存在的共性问题进行了总结分析：一是模型的适用性问题。在过去 30 年中，已经开发了各种各样的 ET 遥感模型来估算从田间尺度（简化经验方程）到区域尺度（单源模型和双源模型），再到陆地尺度（如 ALEXI 模型）的 ET 空间分布。然而，每一种模型都有其各自的局限性，没有一个模型无需经过改进，而适用于全球任何地方的 ET 遥感估算。在 ET 遥感模型应用研究上，最大的挑战就是如何直接或间接利用遥感的地表变量和参数，进行各种地表类型的 ET 参数化估算。二是尺度转换问题。遥感模型给出的是瞬时 ET，需要进行时间尺度转换，即将瞬时空间 ET 转换为一天或更长时间的空间 ET。由于地表异质性和模型的非线性，一般而言适用于局部尺度的 ET 模型有可能不适用于更大的尺度；反之亦然。遥感 ET 尺度问题的解决主要与尺度理论的发展和多尺度遥感数据 的整合有关。三是缺少近地气象观测数据和卫星像元尺度的地表 ET 真实性检验数据。由于研究区域存在很大的区域差异，加之气象站点分布不均衡和代表性不足，以及气象服务的不到位，在 ET 建模过程中时常缺少 PBL 高度、近地表高度和卫星像元尺度的气象数据。另外，将遥感模型估算的 ET 与定点测量的相关数据进行对比，以便确认 ET 遥感模型的可靠性和精确性是必不可少的。尽管利用传统测量的、均质区域的“点”尺度数据验证遥感像元的平均通量是可行且合理的，但是这一做法在地表复杂的区域就会时常产生问题。而且，几种常规的地表 ET 测量技术都存在一定的局限性。四是地表变量/参数反演精度有待进一步提高。目前，基于遥感数据定量反演陆面变量/参数的研究已经取得了很大进展，但在 ET 遥感模型中需要的一些变量/参数如地表温度、LAI、植被覆盖度、植物高度等，其反演精度仍需不断提高。五是全遥感模型的构建问题。在现有 ET 遥感模型中，大多数需要一定的辅助测量数据，从而限制了模型的灵活应用。构建完全依赖遥感数据/产品（部分参数可进行无差别或有限差别的设定）的模型是区域 ET 遥感估算的重要研究方向。

本章最后给出了该论文的总体框架。

论文第二章为LST遥感反演研究。LST可为地表能量平衡时空变化提供重要信息，它不仅是地表能量平衡和温室效应的重要指标，而且是剖析土壤圈、大气圈、水圈相互之间能量转换的关键变量，是许多相关重大课题研究如蒸散发建模、土壤湿度估算等需要考虑的因素。能够在大的空间尺度下对地表温度进行可靠的遥感估算具有重要的意义。本章从辐射传输理论出发，以中国首次业务化运行的静止气象卫星风云-2 号C星（Feng Yun-2C，FY-2C）两个相邻TIR通道即IR1 (10.3-11.3μm)和IR2 (11.5-12.5μm)的遥感信息为数据源，运用Wan和Dozier（1996）提出的广义分裂窗（Generalized Split-Window, GSW）算法，对地表温度进行了估算。本章主要由四部分组成。第一部分为基本理论。主要阐述了利用GSW算法反演LST的相关理论即大气辐射传输理论，并对适用于FY-2C数据的GSW算法发展现状作了介绍。第二部分为估算结果分析。给出了GSW算法系数以及LST估算结果，指出了地表比辐射率（Land Surface Emissivity，LSE)和大气水蒸汽含量（Water Vapor Content，WVC）的给定方法，并对LSE、大气WVC以及仪器噪音的敏感性和不确定性误差进行了分析。考虑到FY-2C搭载的S-VISSR（Stretched-Visible and Infrared Spin-Scan Radiometer) 传感器没有大气探测通道，缺少可资利用的同步地表大气温度，GSW算法所需要的系数是通过如下方式得到的：首先把平均LSE、大气WVC和LST细划为不同的等级（亚级，而且各亚级之间有部分数值重叠），然后利用模拟数据，并采用统计回归方法，对这些参数值进行再计算而得。统计回归过程中所用模拟数据，是由精确的大气辐射传输模型MODTRAN (MODerate spectral resolution atmospheric TRANsmittance algorithm and computer model) 4 在广适的大气和地表环境条件下模拟生成的。模拟分析表明：在LSE已知的条件下，LST可以通过GSW算法来估算，当观测天顶角（Viewing Zenith Angle，VZA）小于 30°时，或VZA小于 60°、大气WVC小于 3.5g/cm^{2}时，LST估算值的均方根误差（Root Mean Square Error，RMSE）不高于 1K。由于GSW算法需要WVC和LSE作为模型输入数据，当传感器MODIS（MODerate resolution Imaging Spectroradiometer）与S-VISSR的扫描时间彼此接近时，MODIS水汽总量产品MOD05 所提供的大气水汽柱高被应用作（代替）WVC数据。对于S-VISSR其它扫描时间的大气WVC可利用Li等（2003）提出的方法来计算。对于LSE，MODIS/Terra的LST产品MOD11B1 提供了热红外第 31 和 32 通道分辨率为 5km的LSE数据，可分别用于替代S-VISSR IR1 和IR2 的LSE。敏感性分析结果表明：当NEΔT（噪音等效温差Noise Equivalent Temperature Difference）=0.1K

时，LST反演结果受影响的程度为 3%；当NEΔT=0.2 K时，受影响的程度为 16%；当NEΔT=0.5K时，受影响的程度为 81%，所对应的分级数据条件为ε∈[0.94,1.0], WVC∈[1.0,2.5], and Ts∈[290K,310K]。假定(1-ε)/ε和$\Delta\varepsilon/\varepsilon^2$的不确定性为 1%左右，在干燥大气状况下，LST误差为[1.3K, 1.5K]，均值为 1.4K；在湿润大气状况下，LST误差为[0.2K, 0.8K]，均值为 0.5K。WVC的不确定性对LST反演结果的影响为 0.3K左右。为了进行交叉验证，该部分还选择了几种新近提出的GSW算法，用相同的FY-2C模拟数据分别进行了LST估算，结果表明，大多数GSW算法的估算结果具有一致性。由此说明，GSW算法能够成功地应用于FY-2C数据的LST反演。第三部分为实际应用。利用FY-2C数据和GSW算法分别估算出了耕地、裸地和海洋的LST，但由于缺少实测数据，没有进行真实性检验。第四部分为该章的主要结论。该章主要研究内容已于 2008 年在期刊Sensors上发表。

论文第三章为地表方向比辐射率遥感反演研究。本章所依据的遥感资料包括MODIS TIR数据和MIR数据，并借用了地表双向反射率遥感模型。迄今为止，在灯光照明和观测几何两个领域，已有开发出许多双向反射率分布函数（Bidirectional Reflectance Distribution Function，BRDF），并应用于可见光和近红外（Near Infrared，NIR）波段的双向反射率研究。半经验核驱动模型已经成功运用到AVHRR（Advanced Very High Resolution Radiometer）、地面反射的极化作用和方向性 (Polarization and Directionality of Earth Reflectance，POLDER波谱仪) 确定、MODIS、多角度图像光谱辐射计(Multi-angle Imaging Spectra-Radiometer，MISR)、实验室分析和多角度反射数据野外测量，并与BRDF观测数据有良好的一致性。目前，只有少量研究关注于MIR波段的BRDF建模，而且主要集中于利用AVHRR和MSG/SEVIRI（Meteosat Second Generation/Spinning Enhanced Visible and Infrared Imager）双向反射率数据来估算MIR波段的比辐射率。本章第一部分论述了基于MODIS中红外波段（约 4.0μm）数据的地表方向比辐射率估算方法。该方法分两步实现：第一步，利用MODIS两个相邻的中红外通道即 22 通道（3.97μm）和 23 通道（4.06μm）的数据，结合Tang和Li[2008a]建立的模型计算双向反射率；第二步利用MIR波段的双向反射率数据和Jiang和Li[2008]建立的模型估算方向比辐射率。第二部分系统介绍了本研究开展方向比辐射率遥感估算所选定的研究区域、MODIS数据源和数据加工过程。在确定BRDF模型的三个参数（k_{iso}、k_{vol}、k_{geo}）时，所采用的共计 10 天的遥感数据为卫星过境时完全无云的MODIS数据，选自 2005 年 7 月 12 日至 30 日。研究区域地处埃及与以色列交界处，纬度为

28.0°N到 32.0° N，经度为 30.0°E到 36.0°E; 为了进行分地类研究，特制作了该区域的方向比辐射率分布图。第三部分给出了一些初步估算成果，并利用MODIS地表温度/比辐射率产品MYD11B1 对其进行了交叉验证。交叉验证结果表明：至少在本个案中，根据本研究给出的方法直接反演的MODIS MIR波段的方向比辐射率，与MODIS产品MYD11B1 中的比辐射率相比，两者有很好的一致性，平均误差=-0.007，RMSE=0.024。第四部分为该章的主要结论。该部分研究内容已于 2009 年在期刊Optics Express上公开发表。

论文第四章致力于叶面积指数（LAI）空间异质性对方向性空隙度遥感估算影响的研究。方向性空隙率或空隙度是光学遥感建模的基本参数之一。在孔隙度遥感估算方面，尽管有些方法已经被人们提出，但很少有人致力于考察尺度效应对该参数的影响。方向性空隙度与LAI往往存在高度的非线性，这就不可避免地在应用一个大的像元时产生尺度偏差。分析方向性空隙度的尺度效应，提高方向性空隙度反演的精确性，并进而提高依靠多光谱、多角度卫星数据反演地表组分温带的精确性等等，皆是十分必须的。基于此，本章通过整合高分辨率(像元尺寸为 20m)方向孔隙率，对该参数的尺度效应进行了分析，所采用的高分辨率方向孔隙率数据根据VALERI (Validation of Land European Remote sensing Instruments) 数据库中的LAI图像资料以及Beer法则估算，并引进了拓展丛生指数Ĉ对尺度偏差进行修正。本章第一部分阐述了方向孔隙率尺度效应估算的理论框架，提出了由局域尺度到大尺度两种不同的参数/变量整合方案。第二部分介绍了本研究所采用的源自VALERI数据库的各类数据的详细信息。第三部分为计算结果分析，通过对空隙率相对尺度偏差的模拟和来自VALERI数据库的空隙率空间尺度偏差、VALERI样点拓展丛生指数Ĉ的计算，在几种景观类型情况下，对与LAI和孔隙率之间非线性关系相关联的尺度效应进行了量化，并用Ĉ对其进行了修正。第四部分为该章的主要结论。公式推导表明：1）相对尺度偏差仅决定于A_p（垂直于阳光的叶片投影面积）函数和LAI的空间异质性，与LAI值本身无关；2）在给定A_p函数和方向的情况下，拓展丛生指数Ĉ与LAI平均值成正比，与LAI的空间异质性成反比。以VALERI为数据源的研究结果表明：对于大多数的土地覆盖类型，随着空间分辨率的下降，孔隙率相对尺度偏差不断增加。由于农作物和森林的LAI方差相对较大，因此大多数农作物样点和混交林样点存在相对较大的偏差，而草地样点和灌丛样点一般有很小的偏差。就拓展丛生指数Ĉ而言，对于纯林、草地和灌丛样点其变化很小，而对于农作物和混交林其变化显著。本文引入的拓展丛生指数Ĉ与传统丛生指数相比赋予了新的含

义，并为以LAI为变量的空隙率估算方法改进和丛生指数应用提供了证据。计算结果展示了（拓展）丛生指数在Beer尺度效应定律和代表空间异质性方面的性能，也说明了利用遥感数据进行空隙率反演的可行性。同时，本研究提出的拓展丛生指数计算方法不仅简单易行，而且可把遥感数据作为数据源，这为全球植被（拓展）丛生指数的制图提供了有力的支持。该部分研究内容已于 2008 年在期刊Sensors上公开发表。

论文第五章给出了一种区域ET全遥感估算方法，即Ts-VI三角形特征空间法。尽管区域ET遥感估算研究已经取得重大进展，但由于在获得大尺度地表实测数据上的困难或缺少行之有效的方法，例如大气温度、风速、水汽压差、植被高度等有关数据仅能从有限的地面观测站（点）获得，因此，大多数现行的ET模型无法开展大尺度ET制图的业务化运行。为了解决上述问题，建立完全依靠遥感数据的模型或有限依赖地面实测数据的参数体系模型（以遥感数据为主要输入）久已成为区域ET研究的重中之重。本研究即借助Ts-VI三角形特征空间探索了一种完全依赖遥感数据的区域ET估算方法。本章第一部分阐述了Ts-VI三角形特征空间法的基本原理，并对该方法的主要假设条件、发展历程和优缺点等进行了简要介绍。该部分经过公式推导，把ET或EF的估算问题，转换为Φ（空气动力学阻抗综合效用系数）的估算问题。第二部分介绍了利用Ts-VI三角形特征空间法进行区域ET全遥感估算的具体步骤：遥感数据下载→剔除有云像元→估算每个像元的植被覆盖率（Fr）→构建Ts-VI三角形特征空间→确定Ts-VI三角形特征空间的干、湿边→计算每个像元的Φ值→利用Φ值计算每个像元的EF→直接利用MODIS数据和产品估算地表净辐射（Rn）和土壤热通量（G）→利用EF、Rn、G估算LE和ET。该方法可同时实现对地表净辐射、土壤热通量、EF和ET在区域尺度上的全遥感估算。Ts-VI三角形特征空间法对ET的成功估算，主要依赖于对三角形空间干、湿边的正确确定。本研究假定湿边为一水平直线。干边采用离差（δ）判定法自动确定：针对任一的Fr值确定相应的$T_{s,max}$→利用线性回归分析得出$T_{s,max}$的回归线→计算任一$T_{s,max}$点与回归线之间的距离，并剔除距离大于 2δ的点→把剩余的$T_{s,max}$的回归线作为干边。准确估算Φ是本方法提高区域ET估算精度的关键。当干、湿边确定后，即可利用两步插值法计算每个像元的Φ。第三部分为估算结果和真实性检验。该部分论述了研究区域、遥感数据源，并利用 2008 年 5 月 20 日到 8 月 21 日LAS在黑河试验场定点实测的田间显热通量数据，对本研究利用Ts-VI三角形特征空间法全遥感反演的同类数据进行了真实性检验。黑河盆地地处中国西北黑河流域中游，植被类型为草地，利用该地区MODIS数据反演得到显热通量，与LAS测量的结果有很好的一致性，两者之间的

均方根误差为 25.07W/m^2。此说明，利用本研究提出的方法确定Ts-VI三角形特征空间的干湿边，并用其进行区域ET估算，至少在本个案中具有足够的精准度。研究表明，Ts-VI三角形特征空间法与传统的区域ET估算法和源自辐射量卫星遥感数据的地表温度/比辐射率计算法相比有其独特的优势，在干旱半干旱气候条件下，该方法不仅可实现区域ET的全遥感估算，而且可取得令人满意的精确度。第四部分为该章的主要结论。Ts-VI三角形特征空间法开辟了一个令人充满希望的研究领域。在区域ET反演研究中，区域ET的反演精度主要取决于Ts-VI三角形特征空间干湿边确定的准确与否以及EF插值估算的准确与否。该方法的精确性及其实用价值还需要进一步经受实践的检验。Ts-VI三角形特征空间干湿边的确定通常有很大的主观性和盲目性，本论文提出的有关法则，通过对植被覆盖度各区间最高地表温度的估算，为干旱半干旱地区Ts-VI三角形特征空间干湿边的确定给出了一种合理且可行的方法。尽管综合效用系数Φ和EF估算的两步插值法仍有不少问题有待进一步研究，但通过LAS数据的真实性检验表明，Ts-VI三角形特征空间法是进行显热通量全遥感估算比较可行的方法。为了降低Ts-VI三角形特征空间法在湍流热通量估算上的不确定性，需要获取更多资料对相关参数/变量进行验证，并在不同类型区的实际应用中对该方法进行逐步的修正和改进。

论文第六章为上述各章的研究结论和对未来区域 ET 遥感估算研究发展前景的展望。未来区域 ET 遥感估算研究的主要发展方向为：1）区域尺度下土壤圈-生物圈-大气圈交界面陆面过程模型研究；2）高精度地表变量（参数）遥感反演研究；3）大气对流对区域 ET 估算影响的深入研究；4）陆面过程遥感模型校准及 ET 制图研究；5）像元尺度 ET 和地表变量（参数）的真实性检验。

本论文得到欧盟第六框架（FP6）研究项目 EAGLE(卫星对地观测角度效应研究，合同文号：SST3 CT2003 502057)和国家自然科学基金项目（批准文号：40425012 和 40871169）的支持。

Chapter 1

Introduction

Generally speaking, EvapoTranspiration (ET) is a term used to describe the loss of water from the earth's surface to the atmosphere by the combined process of both evaporation from the open water bodies, bare soil and plant surfaces, etc. and transpiration from vegetation or any other moisture living surface. Water in an entity or over an interface and energy needed to convert liquid water to the vapor form, along with a mechanism to transport water from the land surface to the atmosphere, are prerequisites to ensure the occurrence of ET. Other factors affecting ET rates mainly include solar radiation, wind speed, vapor pressure deficit and air temperature, etc..

At the beginning of 21st century, there may be no other environmental problems than global climate change that can be the issue of the most concern for humans. Global warming, natural hazards and species extinctions, etc., are several dangerous situations that might happen if the climate change occurs too rapidly. The Intergovernmental Panel on Climate Chang (IPCC) was established by the World Meteorological Organization (WMO) and the United Nations Environment Program (UNEP) in 1988 (http://www.ipcc.ch/about/index.htm) to evaluate the risk of climate change caused by human activity. ET, which governs the water cycle and energy transport among the biosphere, atmosphere and hydrosphere as a controlling factor, plays an important role in hydrology, meteorology, and agriculture, such as in prediction and estimation of regional-scale surface runoff and underground water, in simulation of large-scale atmospheric circulation and global climate change, in the scheduling of field-scale field irrigations and tillage [Idso et al., 1975a; Su, 2002]. On the global basis, the mean ET from the land surface accounts for approximately 60% of the mean precipitation. It is therefore indispensable to have reliable information on the land surface ET when natural hazards such as floods and droughts are predicted and weather forecasting and climate change modeling are performed [Brutsaert, 1986]. However, land surface ET, which is as important as precipitation and runoff in the water cycle modeling, is one of the least understood components of the hydrological cycle. In recent years, except for a few industrialized countries, most countries have undergone an increase of water use due to the population and economic growth and expended water supply systems while irrigation water use accounts for about 70% of water withdrawals worldwide and for more than 90% of the consumptive water use and irrigation water use has been believed to be the most important cause to the increase of water use in most countries [Bates et al., 2008]. Estimation of consumptive use of water based on ET models using remotely sensed data has become one of the hot topics in water resources planning and management over watersheds due to the competition for water between trans-boundary water users [Bastiaanssen et al., 2005]. In climate dynamics, continuous progress has been made to describe the general circulation of the atmosphere and Brutsaert [1986] has shown that the general circulation models appeared to be quite sensitive to the land surface ET information. For vegetated land surfaces, ET rates are closely related to the assimilation rates of plants and can be used as an indicator of plant water stress [Jackon et al., 1981]. Therefore, accurate estimates of regional ET in the land surface water and energy budget modeling at different temporal and spatial scales are essential in hydrology, climatology and agriculture.

In various practical applications, there are still no specific ways to directly measure the actual ET over a watershed [Brutsaert, 1986]. Conventional techniques of ET estimation (i.e., Pan-measurement, Bowen ratio, Eddy correlation system, and Weighing lysimeter, Scintillometer, Sap flow) are mainly based on site (field)-measurement and many of those techniques are dependent on the variety of model complexities. Though they can provide relatively accurate estimates of ET over an homogeneous area, conventional techniques are of rather limited use because they need a variety of surface accessory measurements and land parameters such as air temperature, wind speed, vapor pressure at a reference height, surface roughness, etc., which are difficult to obtain over large-scale terrain areas and have to be extrapolated/interpolated to various temporal and spatial scales with limited accuracy in order to initialize/force those models [Idso et al., 1975a]. Remote sensing technology is recognized as the only viable means to map regional- and meso-scale patterns of ET at the earth's surface in a globally consistent and economically feasible manner and surface temperature helps to establish the direct link between surface radiances and the components of surface energy balance [Weigand and Bartholic, 1970; Idso et al.,1975b; Idso et al., 1975c; Jackson, 1985; Moran et al., 1989; Caselles et al., 1992; McCabe and Wood, 2006]. Remote sensing technology has several marked advantages over conventional "point" measurements: 1) it can provide large and continuous spatial coverage within a few minutes, 2) it costs less when same spatial information is required, 3) it is particularly conducive to ungauged areas where man-made measurements are difficult to be conducted or unavailable [Engman and Gurney, 1991; Rango, 1994]. Remotely sensed surface temperature can provide a measure of surface from a resolution of a few cm^2 from a hand-held thermometer to about several km^2 from certain satellites [Hatfield, 1983]. Combining surface parameters derived from remote sensing data with surface meteorological variables and vegetation characteristics allows the evaluation of ET at local, regional and global-scales. Remote sensing information can provide spatial distribution and temporal evolution of NDVI (Normalized Difference Vegetation Index), LAI (Leaf Area Index), surface Albedo from visible and near-infrared bands and surface emissivity and radiometric surface temperature from MIR (Mid-InfraRed) and TIR (Thermal InfraRed) bands, many of which are indispensable to most of the methods and models that partition the available energy into sensible and latent fluxes components [Mauser and Stephan, 1998]. The possibility and ability of using remote sensing technology to evaluate ET have been recognized and verified since the year 1970 with the help of hand-held and airborne thermometer. But it was not until 1978 with the launch of HCMM (Heat Capacity Mapping Mission) and polar orbiting weather satellites-TIROS-N that were data available for such surface fluxes studies from the spacecrafts [Price, 1980].

The potentiality of using MIR data from space to infer regional and local scale ET has been extensively studied during the past 30 years and substantial progress has been made [Seguin and Itier, 1983]. The methods vary in complexity from simplified empirical regression to physically based surface energy balance models, the vegetation index-surface temperature triangle/trapezoid methods, and finally to data assimilation techniques usually coupled with a numerical model that incorporates all sources of available information to simulate the flow of heat and water transfer through the soil-vegetation-atmosphere continuum [Kustas and Norman, 1996]. In 1970s when split-window technique for surface temperature retrieval was not developed, ET evaluation was often accomplished by regressing thermal radiances from remote sensors and certain surface meteorological measurement variables (solar radiation, air temperature) to in-situ ET observations or by simulating a numerical model of a planetary boundary layer to continuously match the thermal radiances from satellites [Idso et al., 1975a; Idso et al., 1977; Jackson et al., 1977; Price, 1980]. These methods and the refinements have been successfully used in mapping ET over local areas.

However, satellite remote sensing cannot provide near-surface variables such as wind speed, air temperature, humidity, etc., which has to a great extent limited the applications of the energy balance equation to the homogeneous areas with uniform vegetation, soil moisture and topography [Kustas et al., 1994]. Moreover, approaches to deriving land surface ET differ greatly in model-structure complexity, in model input and output and in the advantages and drawbacks when compared to each other. Therefore, with the consideration of the characteristics of the various ET methods developed over the past decades and of the significance of land surface ET to hydrologists, water resources and irrigation engineers, and climatologists, etc., how to calculate the ET over a regional scale or how to estimate ET precisely based on the remote sensing technology has become a critical question in various ET-related applications and studies. Summaries and comparisons of different remote sensing-based ET approaches are urgently required and indispensable for us to better understand the mechanisms of interactions among the hydrosphere, atmosphere and biosphere of the earth.

This introduction provides an overview of a variety of methods and models that have been developed to estimate land surface ET on field, regional and large scales based mainly on remotely sensed data. For each method or model, we shall detail the main theory and assumptions involved in the model development, and highlight its advantages, drawbacks and potentiality. In latter part, methods of how to convert instantaneous ET to daily values, the problems and issues are addressed, and main research contents and organization of this thesis are given.

1.1 Overviews of remote sensing-based ET models in the past decades

Generally, the commonly applied ET models using remote sensing data can be categorized into two types: (semi-) empirical method and analytical method. (Semi-) empirical method is often accomplished by employing empirical relationships and making use of data mainly derived from remote sensing observations with minimum ground-based measurements while analytical method involves the establishment of the physical processes at the scale of interest with varying complexity and requires a variety of direct and indirect measurements from the remote sensing technology and ground-based instruments.

1.1.1 Simplified empirical regression method

The main theory of the simplified empirical regression method firstly proposed by Jackson et al. [1977] over irrigated wheat at Phoenix, Arizona (U.S.A.) directly relates the daily ET to the difference between instantaneous surface temperature (T_s) and air temperature (T_a) measured near midday at about 13h30 to 14h00 local time over diverse surfaces with variable vegetation cover [Courault et al., 2003]. The most general form of the simplified regression method can be expressed mathematically as:

$$LE_d = R_{nd} - B(T_s - T_a)^n \tag{1.1}$$

where LE_d is daily ET and R_{nd} is daily surface net radiation. B and n are site-specific regression coefficients dependent on surface roughness, wind speed and atmospheric stability, etc. [Seguin and Itier, 1983] , which are determined either by linear least squares fit to data or by simulations based on a SVAT (Soil-Vegetation-Atmosphere Transfer) model [Carlson et al., 1995a] or on a boundary layer model [Carlson and Buffum, 1989].

The simplified regression method proposed by Jackson et al. [1977] and its refinements have attracted great attentions in the subsequent operational applications of ET mapping. For example, Jackson et al. [1977] firstly have demonstrated parameter B was 0.064 and n was unity by regressing daily ET from a lysimeter to the daily net radiation and one-time measurement of (T_s-T_a) while Seguin et al. [1982] regressed data over large homogeneous areas in France with regression coefficients of

B=0.025 and n=1. Seguin and Itier [1983] discussed the theoretical basis and applications of the simplified regression method proposed by Jackson et al. [1977], and showed that surface roughness, wind speed and atmospheric stability were the main contributing factors to the regression coefficients and finally recommended different sets of parameters of B and n applicable to 'medium rough' surfaces for stable and unstable cases respectively. Thus, the imposition of a single value of B and n may be unacceptable and specific values should be adjusted according to the broad range of surface roughness, wind speed and atmospheric stability [Caselles et al., 1992]. Carlson et al. [1995a] theoretically analyzed the implications of the regression coefficients in the simplified equation. They defined B as an average bulk conductance for the daily integrated sensible heat flux and n as a correction for non-neutral static stability. A SVAT model was utilized to simulate the relationships between the coefficients B, n and the fractional vegetation cover (Fr) under variable circumstances with surface roughness and geostrophic wind speed respectively ranging from 2 to 30 cm and 1 to 8.5 m/s [Carlson et al., 1995a]. The resultant formulae are expressed as:

$$B = 0.0175 + 0.05Fr \quad (\pm 0.002) \tag{1.2}$$

$$n = 1.004 - 0.335Fr \quad (\pm 0.053) \tag{1.3}$$

This relationship is generally valid at a time period between 12h00 and 14h00 when temperature varies slowly with time [Carlson et al., 1995a].

The height of measurement of T_a in the simplified equation is also not specially specified. Consequently, Jackson et al. [1977] have used the height of 1.5 m as the measurement level of T_a while Seguin and Itier [1983] utilized 2 m instead. Carlson and Buffum [1989] found that the simplified equation might be more applicable to regional-scale ET estimations if the air temperature and wind speed were measured or evaluated at a level of 50 m because at this level the meteorological variables are insensitive to the surface characteristics. They also suggested that a surface temperature rise (e.g., between 08h00 and 10h00 local time) in the morning obtained from Meteosat or GOES (Geostationary Operational Environmental Satellites) could replace the difference between surface and air temperature, in which the regression coefficients were highly sensitive to wind speed and surface roughness.

Two implicit assumptions in the simplified equation are that daily soil heat flux can be assumed to be negligible and instantaneous midday value of sensible heat flux can adequately express the influence of partitioning daily available energy into turbulent fluxes [Courault et al., 2003; Kairu, 1991]. Several papers have tested and verified this simple procedure to estimate daily ET under diverse atmospheric conditions and variable vegetation covers [Jackson et al., 1977; Seguin and Itier, 1983; Nieuwenhuis et al., 1985; Carlson and Buffum, 1989; Thunnissen and Nieuwenhuis, 1990; Caselles et al., 1992; Carlson et al., 1995a]. All the contributions to this work have shown that the error of the calculated daily ET is about 1 mm/day, which is sufficient to give reliable information to the water availability over a regional level [Seguin et al., 1994].

The main advantage of this procedure is its simplicity, whose inputs include only one-time measurements of T_s and T_a near midday and the daily net radiation. Thus, it is very convenient for the simplified empirical equation to be applied so long as these ground-based near midday meteorological measurements and one-time remotely sensed radiometric surface temperature are available. However, the site-specific parameters B and n have more or less limited the applications of the simplified equation method over regional scales with variable surface conditions.

1.1.2 Residual method of surface energy balance

Surface energy balance governs the water exchange and partition of the surface turbulent fluxes into sensible and latent heat fluxes in the soil-vegetation-atmosphere continuum. Residual method of surface energy balance is one of the most widely applied approaches to mapping ET at different temporal and spatial scales. When heat storage of photosynthetic vegetation and surface residuals and horizontal advective heat flow are not taken into account, the one-dimensional form of surface energy balance equation at instantaneous time scale can be expressed numerically as:

$$LE = R_n - G - H \tag{1.4}$$

Each of the three components of the energy balance equation, including surface net radiation (R_n), soil heat flux (G) and sensible heat flux (H), can be estimated by combining remote sensing based parameters of surface radiometric temperature and shortwave albedo from visible, near infrared and thermal infrared wavebands with a set of ground-based meteorological variables of air temperature, wind speed and humidity and other ancillary surface measurements (see Fig.1-1).

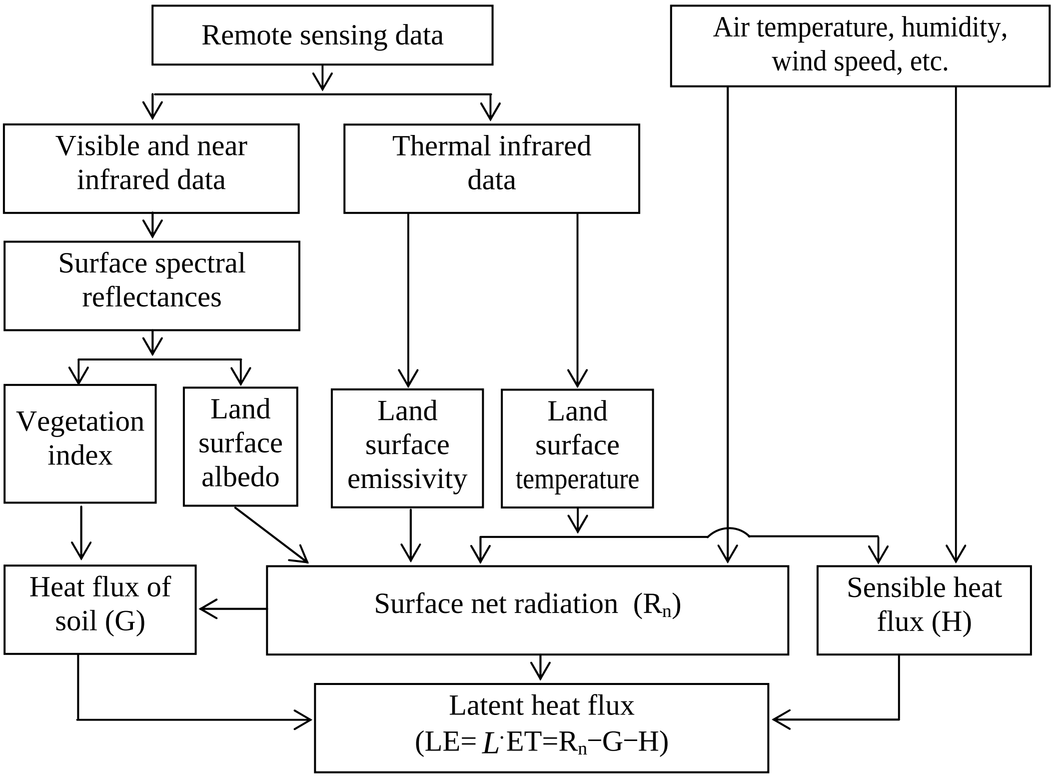

Fig.1-1 Flowchart for estimating ET based on energy balance theory

The residual method of surface energy balance between land and atmosphere can be divided into two categories: 1) single-source model [Brown and Rosenberg, 1973; Bastiaanssen et al., 1998; Roerink et al., 2000a; Boni et al., 2001; Su, 2002; Allen et al., 2007], 2) dual-source model [Norman et al., 1995; Anderson et al., 1997; Kustas and Norman, 1997; Kustas and Norman, 1999; Kustas and Norman, 2000; Chen et al., 2005] and will be addressed in the following parts.

1.1.2.1 Single-source model

Single-source model, also called as big-leaf model, widely used in the simulation of climatology and plays an important role on the continent pattern, is the earliest one to quantitatively depict the conversion process of surface radiation, heat, material etc.. As its name implies, single-source model just regards the earth surface covered with vegetation as a big leaf, ignoring all the secondary structure and characteristics. The physical quantities of leaf such as temperature, water content, radiation etc. represent the corresponding physical quantities of the whole land surface which will constantly exchange energy, heat and moisture with outside atmosphere.

Single-source model is one of the most simplified one in simulating the land surface process and the most widely used one in practice. Three components of the energy balance equation used in equation (1.4) to estimate ET are addressed below.

1.1.2.1.1 Surface net radiation flux (Rn)

Surface net radiation (R_n) represents the total heat energy that is partitioned into *G*, *H* and *LE*. It can be estimated from the sum of the difference between the incoming (R_s) and the reflected outgoing shortwave solar radiation (0.15 to 5μm), and the difference between the downwelling atmospheric and the surface emitted and reflected longwave radiation (3 to 100μm), which can be expressed as [Jackson, 1985; Kustas and Norman, 1996]:

$$R_n = (1-\alpha_s)R_s + \varepsilon_s\varepsilon_a\sigma T_a^{\ 4} - \varepsilon_s\sigma T_s^{\ 4} \tag{1.5}$$

where α_s is surface shortwave albedo, usually calculated as a combination of narrow band spectral reflectance values in the bands used in the remote sensing [Liang, 2004], R_s is determined by a combined factors of solar constant, solar inclination angle, geographical location and time of year, atmospheric transmissivity, ground elevation, etc. [Allen et al., 2007], ε_s is surface emissivity evaluated either as a weighted average between bare soil and vegetation [Li and Lyons, 1999] or as a function of NDVI [Bastiaanssen et al., 1998], ε_a is atmospheric emissivity estimated as a function of vapor pressure and air temperature [Brutsaert, 1975].

Kustas and Norman [1996] reviewed the uncertainties of various methods in estimating the net shortwave and longwave radiation fluxes and found that a variety of remote sensing methods of surface net radiation estimation had an uncertainty of 5-10% from comparisons with ground-based observations at meteorologically temporal scales. Bisht et al. [2005] proposed a simple scheme to calculate the instantaneous net radiation over large heterogeneous surfaces for clear sky days using only land and atmospheric products obtained using remote sensing data from MODIS-Terra satellite over Southern Great Plain (SGP). Allen et al. [2007] detailed an internalized calibration model for calculating ET as a residual of the surface energy balance from remotely sensed data when surface slope and aspect information derived from a Digital Elevation Model (DEM) were taken into account.

1.1.2.1.2 Soil heat flux (G)

Soil heat flux (G) is the heat energy used for warming or cooling substrate soil volume. It is traditionally measured with sensors buried beneath the surface soil and is directly proportional to the thermal conductivity and the temperature gradient with depth of the topsoil. The one used in SEBAL (Surface Energy Balance Algorithm for Land) [Bastiaanssen et al., 1998] to estimate the regional-scale G is expressed as follows

$$G = 0.30(1 - 0.98 NDVI^4) R_n \tag{1.6}$$

As G varies considerably from dry bare soil to highly well watered vegetated areas, it is inappropriate to extrapolate ground-based measurements to values of areal areas. Under current circumstance, it is still impossible to directly measure G from remote sensing satellite platforms. Fortunately, the magnitude of G is relatively small compared to R_n at the daytime overpass time of satellites. Estimation error of G will thus have a small effect on the calculated latent heat flux. Many papers have found the ratio of G to R_n ranges from 0.05 for full vegetation cover or wet bare soil to 0.5 for dry bare soil [Price, 1982; Jackson, 1985; Reginato et al., 1985; Daughtry et al., 1990; Choudhury, 1990; Kustas and Norman, 1996; Li and Lyons, 1999] and this ratio is simply related in an exponential form to LAI [Choudhury, 1989], NDVI [Moran et al., 1989; Bastiaanssen et al., 1998; Allen et al., 2007], T_s [Bastiaanssen, 2000; Allen et al., 2007] and solar zenith angle [Gao et al., 1998] based on field observations. The value of G has been shown to be variable in both diurnal and yearly cycle over diverse surface conditions [Kustas and Daughtry, 1990]. However, the assumption that daily value of G is equal to 0 and can be negligible in the daily energy balance is generally regarded as a good approximation [Price, 1982]. Comparisons of G between results from these simplified techniques and observations at micrometeorological scales showed an uncertainty of 20-30% [Kustas and Norman, 1996].

1.1.2.1.3 Sensible heat flux (H)

The sensible heat flux (H) is the heat transfer between ground and atmosphere and is the driving force to warm/cool the air above the surface. In the single-source energy balance model, it can be calculated by combining the difference of aerodynamic and air temperatures (T_{aero}-T_a) with the aerodynamic resistance (r_a) from:

$$H = \rho c_p (T_{aero} - T_a) / r_a \tag{1.7}$$

where ρ is the air density and c_p is the specific heat of air at constant pressure.

Aerodynamic resistance r_a is affected by a combined factors of surface roughness (vegetation height, vegetation structure), wind speed and atmospheric stability, etc. Therefore aerodynamic resistance to heat transfer must be adjusted according to different surface characteristics except when the water is freely available [Seguin, 1984]. Hatfield et al. [1983] have shown that r_a decreased as the wind speed increased regardless of whether the surface was warmer or cooler than air, and r_a decreased if the surface become rougher. Various methods for calculating r_a have been developed ranging from extremely elementary (a function of wind speed only) to quite rigorous ones (accounting for atmospheric stability, wind speed, surface “aerodynamic” roughness, etc.) [Monteith, 1973; Seguin et al., 1982; Hatfield,1983; Choudhury et al., 1986; Moran et al., 1994], with the commonly applied one being [Brutsaert, 1982]:

$$r_a = \frac{\ln[(z_a - d)/z_{om} - \psi_1]\ln[(z_a - d)/z_{oh} - \psi_2]}{k^2 u} \tag{1.8}$$

where z_a is the measurement height of air temperature and wind speed, z_{om} and z_{oh} are surface roughness length for momentum transfer and heat transfer respectively, d is zero plan displacement height, k is Von Karman constant, u is the wind speed. ψ_1 and ψ_2 are stability correction function for momentum transfer and heat transfer respectively, with neutral stability, $\psi_1 = \psi_2 = 0$.

Jackson et al. [1983] found that T_s-T_a varied from -10 to +5 ^{o}C under medium to low atmospheric humidity, which shows that neutral stability cannot prevail under a wide range of vegetation cover and soil moisture conditions. Under stable and unstable atmospheric stability conditions, the Monin-Obukhov length (Λ) [Monin and Obukhov, 1954] was introduced to measure the stability and it needs to be solved with H iteratively [Choudhury, 1990]:

$$\Lambda = \frac{u*^3 \rho c_p T_a}{kgH} \tag{1.9}$$

where $u*$ is friction velocity and g is the acceleration due to gravity of the earth. if $\Lambda < 0$, unstable stability; $\Lambda > 0$, stable stability.

For unstable conditions (usually prevailing at daytime) with no predominant free convection, ψ_1 and ψ_2 can be expressed as [Paulson, 1970]:

$$\psi_1 = 2\ln(\frac{1+x}{2}) + \ln(\frac{1+x^2}{2}) - 2\arctan(x) + \frac{\pi}{2} \tag{1.10}$$

$$\psi_2 = 2\ln(\frac{1+x^2}{2}) \tag{1.11}$$

with

$$x = (1 - 16\frac{z_a - d}{\Lambda})^{0.25} \tag{1.12}$$

For stable conditions (usually prevailing at night-time), the formula proposed by Webb [1970] and Businger et al. [1971] was adopted to account for the effects of atmospheric stability on r_a :

$$\psi_1 = \psi_2 = -5\frac{z_a - d}{\Lambda} \tag{1.13}$$

Hatfield et al. [1983] have shown that ET rates could be over-estimated when the canopy-air temperature difference is greater than about ±2^{o}C if the aerodynamic resistance is not corrected for atmospheric stability.

The surface roughness plays a significant role in the determination of sensible heat flux and it changes apparently with leaf size and the flexibility of petioles and plant stems [Jackson, 1985]. The effective roughness for momentum z_{om} is considered to be some unspecified distance above a zero plane displacement height where the wind speed is assumed to be zero when log-profile wind speed is extrapolated downward, rather than at true ground surface [Carlson et al., 1981]. Some papers have specified z_{om} is equal to z_{oh} and can be either a function of vegetation height [Soer, 1980; Gurney and Camillo, 1984], in which z_{om} is typically 5 to 15 percent of vegetation height depending on vegetation characteristics [Monteith and Unsworth, 1990], or estimated from wind profiles, using an extrapolation of the standard log-linear wind relationship to zero wind speed [Gurney and Camillo, 1984]. Brutsaert [1982] showed that the heat transfer was mainly driven by molecular diffusion while the momentum transfer near the surface was controlled by both viscous shear and pressure forces. Because of the differences between heat and momentum transfer mechanisms, there is a distinction between z_{om} and z_{oh}, which has caused an additional resistance (often expressed as aerodynamic definition of kB^{-1}（$kB^{-1}=\ln(z_{om}/z_{oh})$） [Li and Lyons, 1999]) to heat transfer [Garratt and Hicks, 1973] or an excess (extra) resistance [Norman and Becker, 1995]. Kustas et al. [1989] related the kB^{-1} (radiometric definition [Li and Lyons, 1999]) to the combined factors of wind speed and the difference between T_s and T_a in the following form:

$$kB^{-1} = S_{kB} u (T_s - T_a) \tag{1.14}$$

where S_{kB} is an empirical coefficient, ranging from 0.05 to 0.25 [Li and Lyons, 1999].

Verhoef et al. [1997] showed that kB^{-1} was sensitive to the measuring errors both in the micrometeorological variables and in the roughness length for momentum and its value over bare soil could be less than zero. Massman [1999] used a physically based “localized near-field” Lagrangian theory to evaluate the effects of kB^{-1} on the vegetative components in the two-source energy balance models and on the combined effects of soil and vegetation in a single-source model. Su et al. [2001] proposed a quadratic weighting based on the fractional coverage of soil and vegetation to calculate the kB^{-1} in order to take into account of any situation from full vegetation to bare soil conditions. What should be noted is that the determination of the surface roughness still remains a challenging issue for large scale retrieval of the turbulent fluxes in spite of the efforts made in the past.

Klaassen and van den Berg [1985] showed that the measurement (or reference) height should be set at 50 m instead of 2 m at the bottom of the mixed layer and calculation of ET of crops over rough surfaces could be improved with increasing reference height.

T_{aero}, the temperature at level of $d+z_{oh}$, which is the average temperature of all the canopy elements weighted by the relative contribution of each element to the overall aerodynamic conductance [Moran et al., 1989], may be estimated from extrapolation of temperature profile down to $z=d+z_{oh}$ and is recognized as the temperature of the apparent sources or sinks of sensible heat [Kalma and Jupp, 1990]. A number of papers have utilized remotely sensed surface temperature T_s instead of T_{aero} in Eq. (1.7) to calculate H over a wide range of vegetated surfaces because T_{aero} is very difficult to measure [Blad and Rosenberg, 1976; Seguin et al., 1982; Moran et al., 1989; Kalma and Jupp, 1990;]. However, there are problems associated with the assumption that measured T_s is identical to T_{aero} [Kalma and Jupp, 1990]. T_{aero} is found to be lower (higher) than T_s under stable (unstable) atmospheric conditions and they are nearly the same only under neutral conditions [Choudhury et al., 1986; Kalma and Jupp, 1990]. Kustas and Norman [1996] concluded that the differences between T_{aero} and T_s could range from 2 ^oC over uniform vegetation cover to 10 ^oC for partially vegetated areas. Subsequently dual-source (two-source) models have been developed to account for the differences between T_{aero} and T_s, and thus avoid the needs for adding excess resistance in Eq. (1.7) [Norman et al., 1995].

The bulk transfer equation (resistance-based model) expressed in Eq.(1.7) has been predominately applied since 1970s over a local/regional scale with various vegetation covers [Blad and Rosenberg,1976; Hatfield, 1983; Moran and Jackson,1991]. The average difference of H estimated by different authors based on the bulk transfer equation is about 15-20%, which is around the magnitude of uncertainty in eddy correlation and Bowen ratio techniques for determining the surface fluxes in heterogeneous terrain [Seguin, 1984; Kustas and Norman, 1996].

Generally speaking, energy balance models are theoretically verified and physically based. Single source models are usually computationally timesaving and require less ground-based measurements compared to dual-source models. Over homogeneous areas, single-source models can evaluate ET with a relatively high accuracy. But over partially vegetated areas, there is a strong need to develop a dual-source model to model separately the heat and water exchange and interaction between soil and atmosphere and between vegetation and atmosphere, which often deals with a decomposition of radiometric surface temperature to soil and vegetation component temperatures either from multi-angular remotely sensed thermal data or from an iteration of respective solution of soil and vegetation energy balance combined with a Priestly-Taylor equation. A major dilemma with both the physics-based single and dual-source models lies in the requirements for sufficiently detailed parameterization of surface soil and vegetation properties and ground-based measurements, such as air temperature, wind speed, surface roughness, vegetation height, etc., as model inputs.

1.1.2.1.4 Discription of typical Single-source Models for Estimating Sensible Heat Flux (H)

In the single-source surface energy balance models, the main distinction of various methods is how to estimate the sensible heat flux. Some of them are based on the spatial context information (emergence of representative dry and wet pixels) of land surface characteristics in the area of interest. Some of them are not. Below we will review several representative single-source energy balance models.

(1) SEBI (Surface Energy Balance Index) and SEBS (Surface Energy Balance System)

SEBI, firstly proposed by Menenti and Choudhury [1993], along with its derivatives like SEBAL, S-SEBI (Simplified-SEBI), SEBS, METRIC (Mapping ET at high Resolution with Internalized Calibration) etc., is typically a single-source energy balance model based on the contrast between dry and wet limits to derive pixel by pixel ET and EF from the relative evaporative fraction when combined with surface parameters derived from remote sensing data and a certain amount of ground-based variables over local/regional scale surfaces [Gowda et al., 2007]. The dry (wet) limit, no matter how it was specifically defined, often has the following characteristics: 1) generally maximum (minimum) surface temperature, 2) usually low or no (high or maximum) ET.

In SEBI method, the dry limit is assumed to have a zero surface ET (latent heat flux) for a given set of boundary layer characteristics (potential temperature T_{pbl}, wind speed and humidity, etc.). So the sensible heat flux is then equal to the surface available energy, with the $T_{s,\max}$ inverted from the bulk transfer equation being expressed as [Van den Hurk, 2001]:

$$T_{s,\max} = T_{pbl} + r_{a,\max} \frac{H}{\rho c_p} \tag{1.15}$$

Correspondingly, the minimum surface temperature can be evaluated from the wet limit, where the surface is regarded as to evaporate potentially and the potential ET (LE_p) is calculated from Penman-Monteith equation with a zero internal-resistance. The $T_{s,\min}$ is expressed as [Van den Hurk, 2001]:

$$T_{s,\min} = T_{pbl} + \frac{r_{a,\min} \frac{R_n - G}{\rho c_p} - VPD/\gamma}{1 + \Delta/\gamma} \tag{1.16}$$

where VPD represents Vapor Pressure Deficit, γ is Psychrometric constant.

The relative evaporation fraction can then be calculated by interpolating the observed surface temperature within the maximum and minimum surface temperature in the following form [Van den Hurk, 2001]:

$$\frac{LE}{LE_p} = 1 - \frac{r_a^{-1}(T_s - T_{pbl}) - r_{a,\min}^{-1}(T_{s,\min} - T_{pbl})}{r_{a,\max}^{-1}(T_{s,\max} - T_{pbl}) - r_{a,\min}^{-1}(T_{s,\min} - T_{pbl})} \tag{1.17}$$

where the second part of the right hand side of Eq.(1.17) is the so-called SEBI which varies between 0 (actual=potential ET) and 1 (no ET).

Parameterization of SEBI approach was first proposed by defining theoretical pixel-wise ranges for *LE* and T_s to account for spatial variability of actual evaporation due to albedo and aerodynamic roughness [Menenti and Choudhury, 1993]. This parameterization was essentially a modification from CWSI (Crop Water Stress Index) proposed by Idso et al. [1981] and Jackson et al. [1981; 1988]. The theoretical CWSI accounted for the effects of the net radiation and wind speed in addition to the temperature and vapor pressure required by the empirical CWSI. Taking into account the dependence of external resistance on the atmospheric stratification, Menenti and Choudhury [1993] proposed an approach to calculate the pixel-wise maximum and minimum surface temperature and redefined CWSI as a pixel-wise SEBI at given surface reflectance and roughness to derive the regional ET from the relative evaporative fraction. The CWSI was based on surface meteorological scaling while the SEBI used Planetary Boundary Layer (PBL) scaling. Subsequently the SEBAL, SEBS and S-SEBI models have been developed from this conception of SEBI. The main distinction between each of these models and other commonly applied single-source models is the difference of how to calculate the sensible heat flux or precisely how to define the dry (maximum sensible heat and minimum latent heat) and wet (maximum latent heat and minimum sensible heat) limits and how to interpolate between the defined upper and lower limits to calculate the sensible heat for a given set of boundary layer parameters of both remotely sensed T_s, Albedo, NDVI, LAI, F_r and ground-based air temperature, wind speed, humidity, vegetation height, etc.. Assumptions in SEBI, SEBAL, S-SEBI, SEBS models are that there are few or no changes in atmospheric conditions (mainly the surface available energy) in space and sufficient surface horizontal variations are required to ensure dry and wet limits exist in the study region.

The Surface Energy Balance System (SEBS), detailed by Su [2001; 2002; 2005], Su et al. [2003] with a dynamic model for the thermal roughness and the Bulk Atmospheric Similarity (BAS) theory for PBL scaling and the Monin-Obukhov Atmospheric Surface Layer (ASL) similarity for surface layer scaling, is an extension from the concept of SEBI for the estimation of land surface energy balance using remotely sensed data in a more complex framework. SEBS consists of 1) a set of tools for the calculations of land surface physical parameters, 2) calculation of roughness length for heat transfer, 3) estimation of the evaporative fraction based on energy balance at limiting cases [Su, 2002]. In SEBS, at the dry limit, latent heat flux is assumed to be zero due to the limitation of soil moisture which means sensible heat flux reaches its maximum value (i.e., $H_{dry}=R_n-G$). At the wet limit, ET takes place at potential rate (LE_{wet}), (i.e. ET is limited only by the energy available under the given surface and atmospheric conditions, which can be calculated by a combination equation similar to the Penman-Monteith combination equation [Monteith, 1965] assuming that the bulk internal resistance is zero), the sensible heat flux reaches its minimum value, H_{wet}. The sensible heat flux at dry and wet limits can be expressed as:

$$H_{dry} = R_n - G \tag{1.18}$$

$$H_{wet} = ((R_n - G) - \frac{\rho C_p}{r_a}\frac{VPD}{\gamma}) / (1 + \frac{\Delta}{\gamma}) \tag{1.19}$$

where r_a is dependent on the Obukhov length, which in turn is a function of the friction velocity and sensible heat flux.

The EF_r and EF then can be expressed as:

$$EF_r = 1 - \frac{H - H_{wet}}{H_{dry} - H_{wet}} \tag{1.20}$$

$$EF = \frac{EF_r \cdot LE_{wet}}{R_n - G} \tag{1.21}$$

H can be solved using a combination of a dynamic model for thermal roughness [Su, 2001] and the BAS theory of Brutsaert [1999] for PBL scaling and the Monin-Obukhov ASL similarity for surface layer scaling [Monin and Obukhov, 1954].

In SEBS, distinction is made between the ABL (Atmospheric Boundary Layer) or PBL (Planetary Boundary Layer) and the ASL similarity. Inputs to the SEBS include remote sensing data-derived land parameters and ground-based meteorological measurements, such as land surface temperature, LAI, fractional vegetation cover, albedo, wind speed, humidity, air temperature. Jia et al. [2003] described a modified version of SEBS using remote sensing data from ATSR (Along Track Scanning Radiometer) and ground data from a Numerical Weather Prediction model and validated the estimated sensible heat flux with large aperture scintillometers located at three sites in Spain. With the surface meteorology derived from the Eta Data Assimilation System (EDAS), Wood et al. [2003] applied SEBS to the SGP region of the United States where the ARM (Atmospheric Radiation Measurement) program had been carried out by the U.S. Department of Energy. Derived latent heat fluxes were compared with the measurements from the EBBR (Energy Balance Bowen Ration) sites and results indicated that the SEBS approach had promise in estimating surface heat flux from space for data assimilation purposes. SEBS has been used to estimate daily, monthly and annual evaporation in a semi-arid environment [Su et al., 2003]. Su [2002] showed that SEBS could be used for both local scaling and regional scaling under all atmospheric stability regimes.

Advantages of the SEBS are that 1) uncertainty from the surface temperature or meteorological variables in SEBS can be limited with consideration of the energy balance at the limiting cases, 2) new formulation of the roughness height for heat transfer is developed in SEBS instead of using fixed values, 3) a priori knowledge of the actual turbulent heat fluxes is not required. However, too many required parameters and relatively complex solution of the turbulent heat fluxes in SEBS have brought more or less inconveniences when data are not readily available.

(2) S-SEBI

A new method, called the S-SEBI developed by Roerink et al. [2000a] to derive the surface energy balance, has been tested and validated with data from a small field campaign conducted during August 1997. The main theory of S-SEBI is based on the contrast between a reflectance (albedo) dependent maximum surface temperature for dry limit and a reflectance (albedo) dependent minimum surface temperature for wet limit to partition available energy into sensible and latent heat fluxes.

A theoretical explanation to S-SEBI, when a wide range of surface characteristics changing from dry/dark soil to wet/bright pixels exist, can be given: 1) at low reflectance (albedo), surface temperature keeps almost unchangeable because of the sufficient water available under these conditions, such as over open water or irrigated lands, 2) at higher reflectance (albedo), surface temperature increases to a certain point with the increases of reflectance due to the decrease of ET resulting from the less water availability, which is termed as "evaporation controlled", 3) after the inflexion, the surface temperature will decrease with the increases of surface reflectance (albedo), which is called the "radiation controlled" (see Fig.1-2).

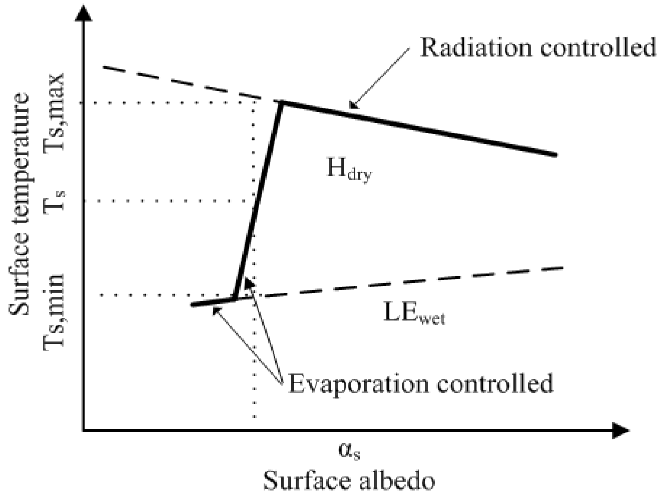

Fig.1-2 Theoretically schematic relationship between surface temperature and alebdo in the S-SEBI (after [Roerink et al., 2000a])

In S-SEBI, the evaporative fraction is bounded by the dry and wet limits and formulated by interpolating the reflectance (albedo) dependent surface temperature between the reflectance (albedo) dependent maximum surface temperature and the reflectance (albedo) dependent minimum surface temperature, which can be expressed as:

$$EF = \frac{T_{s,\max} - T_s}{T_{s,\max} - T_{s,\min}} \tag{1.22}$$

where $T_{s,max}$ corresponds to the minimum latent heat flux (LE_{dry}=0) and maximum sensible heat flux (H_{dry}=Rn-G) (the upper decreasing envelope when T_s is plotted against surface reflectance (albedo)), $T_{s,min}$ is indicative of the maximum latent heat flux (LE_{wet}=Rn-G) and minimum sensible heat flux (H_{wet}=0) (the lower increasing envelope when T_s is plotted against surface reflectance). $T_{s,max}$ and $T_{s,min}$ are regressed to the surface reflectance (albedo):

$$T_{s,\max} = a_{\max} + b_{\max}\alpha_s \tag{1.23}$$

$$T_{s,\min} = a_{\min} + b_{\min}\alpha_s \tag{1.24}$$

where a_{max}, b_{max}, a_{min} and b_{min} are empirical coefficients estimated from the scatter plot of T_s and α_s over study area.

Inserting Eqs.(1.23-1.24) into Eq.(1.22), EF can be derived by

$$EF = \frac{a_{\max} + b_{\max}\alpha_s - T_s}{a_{\max} - a_{\min} + (b_{\max} - b_{\min})\alpha_s} \tag{1.25}$$

If the atmospheric conditions over the study area can be regarded as constant and sufficient variations in surface hydrological conditions are present, the turbulent fluxes then can be calculated with S-SEBI without any further information than the remote sensing image itself. Results from Roerink et al. [2000a] have shown that measured and estimated evaporative fraction values had a maximum relative difference of 8% when measurements obtained from a small field campaign during

1997 in Italy were compared with the S-SEBI derived outputs.

The major advantage of this S-SEBI is that 1) besides the parameters of the surface temperature and reflectance (albedo) derived from remote sensing data no additional ground-based measurement is needed to derive the EF if the surface extremes are present in the remotely sensed imagery, 2) the extreme temperatures in the S-SEBI for the wet and dry conditions vary with changing reflectance (albedo) values, whereas other methods like SEBAL try to determine a fixed temperature for wet and dry conditions. However, it should be noted that atmospheric corrections to retrieve T_s and α_s from satellite data and determination of the extreme temperatures for the wet and dry conditions are location-specific when atmospheric conditions over larger areas are not constant any more.

(3) SEBAL and METRIC

SEBAL, developed by Bastiaanssen [1995] and Bastiaanssen et al. [1998] with minimum ground-based measurements to evaluate ET, has been tested at both field and catchments scales under several climatic conditions in more than 30 countries worldwide, with the typical accuracy at field scale being 85% and 95% at daily and seasonal scales respectively [Bastiaanssen et al., 1998; Bastiaanssen, 2000; Allen et al., 2001; Bastiaanssen et al., 2005].

One of the main considerations in SEBAL, when evaluating pixel by pixel sensible and latent heat fluxes, is to establish the linear relationships between T_s and the surface-air temperature difference dT (dT=T_s-T_a) on each pixel with the coefficients of the linear expressions determined from the extremely dry (hot) and wet (cold) points. The dT can be approximated as a relatively simple linear relation of T_s expressed as:

$$dT = a + bT_s \tag{1.26}$$

where a and b are empirical coefficients derived from two anchor points (dry and wet points).

At the dry (hot) pixel, latent heat flux is assumed to be zero and the surface-air temperature difference at this pixel is obtained by inverting the single-source bulk aerodynamic transfer equation:

$$dT_{dry} = \frac{H_{dry} \times r_a}{\rho C_p} \tag{1.27}$$

where H_{dry} is equal to R_n-G.

At the wet (cold) pixel, latent heat flux is assigned a value of R_n-G (or a reference ET), which means sensible heat flux under this condition is equal to zero (when reference ET is applied, both H and dT at this pixel will not equal zero any more). Obviously, the surface-air temperature difference at this point is also zero (dT_{wet}=0).

After calculating surface-air temperature differences at both dry (hot) and wet (cold) points, coefficients a and b in Eq. (1.26) can be obtained. Providing that a and b are known, the surface-air temperature difference dT at each pixel over the study area is estimated with T_s using Eq. (1.26). Finally, H can be obtained iteratively with r_a corrected for stability using Eq. (1.7). This procedure requires wind speed measured at ground to be extrapolated to a blending height of about 100 to 200 m where wind speed at this level is assumed to be not affected by surface variations.

SEBAL has been applied for ET estimation, calculation of crop coefficients and evaluation of basin wide irrigation performance under various agro-climatic conditions in several countries including Spain, Sri Lanka, China, and the United States, etc. [Bastiaanssen et al., 2005; Singh et al., 2008]. Timmermans et al. [2007] compared the spatially distributed surface energy fluxes derived from SEBAL with a dual-source energy balance model using data from two large scale field experiments covering sub-humid grassland (Southern Great Plains '97) and semi-arid rangeland (Monsoon '90). Norman et al. [2005] showed that the assumption of linearity between surface temperature and the air temperature gradient used in defining the sensible heat fluxes did not generally hold true for strongly heterogeneous landscape. The selection of dry pixel and wet pixel can have a significant impact on the heat flux distribution from SEBAL.

One of the assumptions made in SEBAL model is that full hydrological contrast (i.e., wet and dry pixels) is present in the area of interest. The most key aspect in the SEBAL is to identify the dry pixel while wet pixel is often determined over a relatively large calm water surface or at a location of well-watered areas. The advantages of the SEBAL over previous approaches to estimate land surface fluxes from thermal remote sensing data are: 1) it requires minimum ancillary ground-based data, 2) it does not require a strict correction of atmospheric effects on surface temperature thanks to its automatic internal calibration, and 3) internal calibration can be done within each analyzed image. However, SEBAL has several drawbacks: 1) it requires subjective specifications of representative hot/dry and wet/cool pixels within the scene to determine model parameters *a* and *b*, 2) it is often applied over flat surfaces. When SEBAL is applied over mountainous areas, adjustments based on a DEM need to be made to *Ts* and *u* to account for the lapse rate, 3) errors in surface temperatures or surface-air temperature differences have great impacts on H estimate, 4) radiometer viewing angle effects, which can cause variation in Ts of several degrees for some scenes, have not been taken into account.

To avoid the limitations of the SEBAL in mapping regional ET over more complicated surfaces, Allen et al. [2005a; 2005b; 2007] highlighted a similar SEBAL-based approach, named as METRIC, to derive ET from remotely sensed data in the visible, near-infrared and thermal infrared spectral regions along with ground-based wind speed and near surface dew point temperature. In METRIC, an automatic internal calibration method similar to SEBAL (linearly relating Ts to the surface-air temperature difference) is used to calculate the sensible and latent heat fluxes.

Main distinctions between METRIC and SEBAL are: 1) METRIC does not assume $H_{wet}=0$ or $LE_{wet}=R_n-G$ at the wet pixel, instead a daily surface soil water balance is run to confirm that for the hot pixel, ET is equal to zero, and for the wet pixel, ET is set to $1.05ET_r$, where ET_r is the hourly (or shorter time interval) tall reference (like alfalfa) ET calculated using the standardized ASCE (American Society of Civil Engineers) Penman-Monteith equation, 2) wet pixel in METRIC is selected in an agricultural setting where the cold pixel should have biophysical characteristics similar to the reference crop (alfalfa), 3) the interpolation (extrapolation) of instantaneous ET to daily value is based on the alfalfa ET_rF (defined as the ratio of instantaneous ET to the reference ET_r that is computed from meteorological station data at satellite overpass time) instead of the actual evaporative fraction, which can better account for the impacts of advection and changing wind and humidity conditions during the day.

(4) VI-Ts Triangle/Trapezoidal feature space

VI-T_s triangle feature space, derived from the contextual information of remotely sensed surface temperature T_s and Vegetation Index (VI), was firstly proposed by Goward et al. [1985], and subsequently was utilized to study the soil water content, surface resistance, land use and land cover change, drought monitoring and regional ET [Nemani and Running, 1989; Nemani et al., 1993; Lambin and Ehrlich, 1996; Jiang and Islam, 1999; Jiang and Islam, 2001; Jiang and Islam, 2003] while the trapezoidal space was derived from a simple CWSI [Jackson et al., 1981; Idso et al., 1981].

The T_s-VI triangle/trapezoidal feature space established under the conditions of full ranges of soil moisture content and vegetation is characteristic of being bounded with an upper decreasing envelope (dry edge, defined as the locus of the highest surface temperatures under differing amounts of vegetation cover at a given atmospheric forcing, which is assumed to represent pixels of unavailability of soil moisture content) and a lower nearly horizontal envelope (wet edge, defined as the locus of the lowest surface temperatures under differing amounts of vegetation cover, which is regarded to describe pixels in the potential ET at the given atmospheric forcing) with increasing vegetation cover and the two envelopes ultimately intersect at a (truncated) point at full vegetation cover (see Fig.1-3).

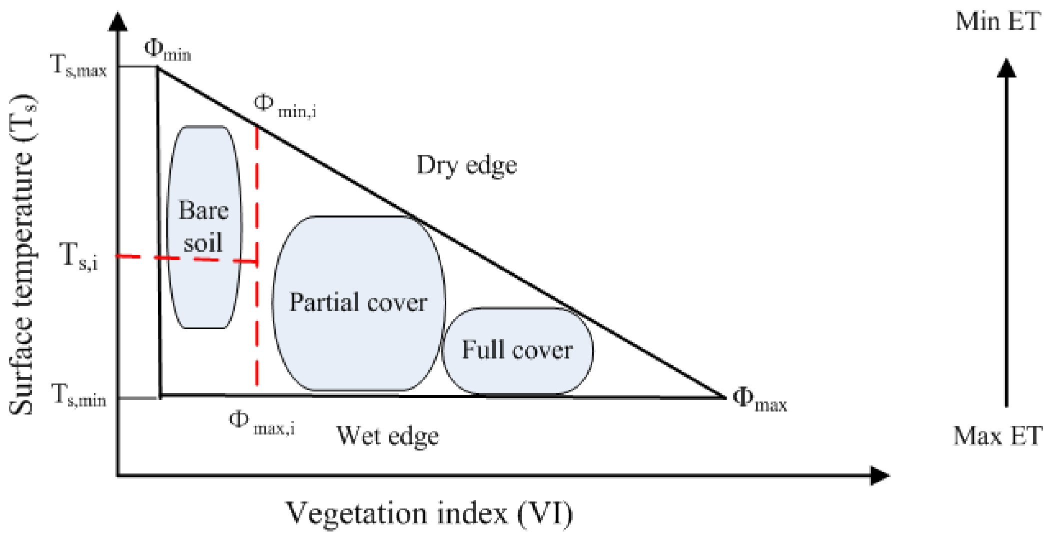

Fig.1-3 The simplified VI-T_s triangular space (after [Lambin and Ehrlich, 1996])

The principal rationale of the T_s-VI triangle and trapezoid to be applied to evaluate ET at regional scale will be addressed respectively as follows.

i) Triangle method

A simplicity of Priestley-Taylor formulation with fully remotely sensed data proposed by Jiang and Islam [1999; 2001; 2003] representatively based on the interpretations of the remotely sensed T_s-NDVI triangle feature space, has been employed to estimate regional EF and ET, which can be expressed as:

$$LE = \Phi[(R_n - G)\frac{\Delta}{\Delta + \gamma} \tag{1.28}$$

where Φ ranges from 0 to 1.26, Δ is slope of saturated vapor pressure as function of T_a. In Eq.(1.28), all terms in the right-hand side can be calculated using remotely sensed data [Jiang and Islam1999].

Solution of parameter Φ in Eq.(1.28) generally involves a certain degree of simplicity and some assumptions, including 1) a complete range of soil moisture and vegetation coverage at satellite pixel scale should be ensured, 2) contaminations of clouds and atmospheric effects have to be removed, 3) two-step linear interpolation scheme [Jiang and Islam, 1999; Carlson, 2007; Stisen et al., 2008] is used to get the value of Φ in Eq. (1.28) based on the Ts-NDVI triangle feature space as displayed in Fig.1-3. This two-step linear interpolation is realized in the following manner: 1) a global minimum and maximum Φ are respectively set to $\Phi_{\min}$ =0 on the driest bare soil pixel and $\Phi_{\max}$ =1.26 on the pixel with largest NDVI and lowest T_s, and $\Phi_{\min,i}$ for each NDVI interval (i) is linearly interpolated with NDVI between $\Phi_{\min}$ and $\Phi_{\max}$, and $\Phi_{\max,i}$ for each NDVI (i) is calculated using the lowest surface temperature within that NDVI interval (generally, one assumes that $\Phi_{\max,i} = \Phi_{\max} = 1.26$), 2) Φ_i within each NDVI interval is linearly increased with the decrease of T_s between $\Phi_{\min,i}$ and $\Phi_{\max,i}$.

The triangular (trapezoidal) feature space (T_s-VI) constructed by plotting the remotely sensed surface temperature (or temperature difference, or a scaled surface temperature) against the vegetation indices (e.g., NDVI, SAVI - Soil-Adjusted Vegetation Index, a scaled NDVI, or F_r - fractional vegetation cover) for a full range of variability in surface soil moisture and fractional vegetation cover has been found in a series of papers to derive surface soil moisture, and surface fluxes [Goward et al., 1985; Hope, 1988; Nemani and Running, 1989; Price, 1990; Nemani et al., 1993; Choudhury, 1994; Moran et al., 1994; Carlson et al., 1995a; Gillies and Carlson, 1995; Moran et al., 1996; Jiang and Islam, 1999; Jiang and Islam, 2001; Jiang and Islam, 2003; Venturini et al., 2004; Batra et al., 2006; Wang et al., 2006; Carlson, 2007; Stisen et al., 2008] and has been verified using measurements collected during the MONSOON 90 [Kustas et al., 1991] and FIFE 1987 and 1989 field programs [Sellers et al., 1992]. Jiang and Islam [1999] proposed the NDVI-T_s triangle scheme to estimate surface ET over large heterogeneous areas from AVHRR data over the Southern Great Plain. The proposed approach appeared to be more reliable and easily applicable for operational estimate of ET over large areas. Gillies and Carlson [1995] and Carlson [2007] have examined the triangular patterns of T_s plotted against VI using the simulated surface temperature and NDVI with a SVAT model on a theoretical basis and analyzed the spatial distributions of surface soil moisture availability and EF in the triangle feature space. Batra et al. [2006] have analyzed the effects of spatial resolution of different remote sensing data on the VI-T_s triangle with MODIS，NOAA16 and NOAA14 data in the Southern Great Plain in USA. Wang et al. [2006] combined the advantages of both the thermal inertia method and the T_s-NDVI spatial variation method to develop a day-night T_s difference-NDVI approach and satisfactory results have been obtained at the Southern Great Plain of the United States from April 2001 to May 2005 when compared with the ground-based observations collected by Energy Balance Bowen Ratio Systems. The triangle method, proposed by Jiang and Islam [1999], was modified by Stisen et al. [2008] to take into account of the non-linear interpolation between Φ and the surface temperature to estimate surface fluxes based entirely on remotely sensed data from MSG/SEVIRI (Meteosat Second Generation / Spinning Enhanced Visible and Infrared Imager) sensor. Carlson et al. [1995a] have showed that the emergence of the triangle shape when the scatter plots of T_s versus VI were plotted under the same coordinate system seemed to depend more on the number of pixels rather than just the spatial resolutions. Thus the triangle/trapezoid can be found from T_s and VI data derived from satellites/sensors of different scales, such as the higher-resolution TM and the lower-resolution GOES data [Diak et al., 1995].

Implications in the so-called triangle/trapezoidal method are that 1）the sensitivity of surface temperature to canopy and soil differs and canopy temperature is insensitive to surface/deep-layer soil moisture content, which contributes to the (truncated) vertex at full vegetation cover, 2）variations in the VI-T_s triangle space are not primarily caused by differences in atmospheric conditions but by the variations in available soil water content.

The major assets of the remotely sensed VI-T_s triangle method are that 1) it allows for accurate estimate of regional ET with no ancillary atmospheric or ground data besides the remotely sensed surface temperature and vegetation indices, 2) it is relatively insensitive to the correction of atmospheric effects. The limitations are that 1) determination of the dry and wet edges requires a certain degree of subjectivity, 2) a large number of pixels over a flat area with a wide range of soil wetness and fractional vegetation cover are required to make sure that the dry and wet limits exist in the VI-T_s triangle space.

ii) Trapezoid method

On the basis of CWSI [Jackson et al., 1981], Moran et al. [1994] introduced a Water Deficit Index (WDI, defined as 1 minus the ratio of actual to potential ET) for ET estimate based on the Vegetation Index/Temperature (VIT) trapezoid to extend the application of CWSI over fully to partially vegetated surface areas. The ground-based inputs to the trapezoid method include vapor pressure, air temperature, wind speed, maximum and minimum stomatal resistances, etc.. One of the assumptions in the trapezoid approach is that values of T_s-T_a vary linearly with vegetation cover along crop extreme conditions edges while all the intermediary conditions relating T_s-T_a to a vegetation index are included within the constructed trapezoid. In order to calculate the WDI value of pixels of intermediate vegetation cover and soil moisture content for a specific time, four vertices of the trapezoid, corresponding to (1) well watered full-cover vegetation, (2) water-stress full-cover vegetation, (3) saturated bare soil, and (4) dry bare soil, should be computed firstly combined with the CWSI theory and Penman-Monteith equation (see Fig.1-4).

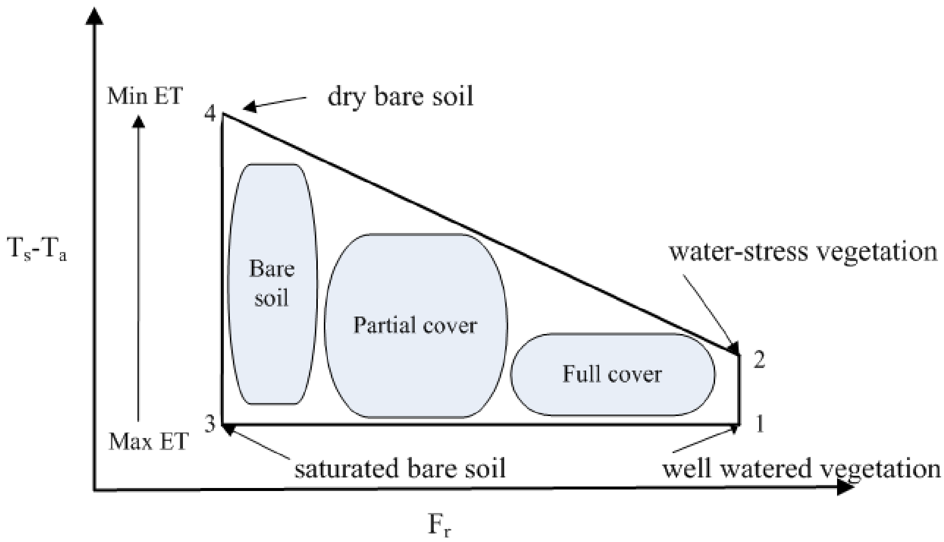

Fig.1-4 The hypothetical trapezoidal space between T_s-T_a and F_r (after [Moran et al., 1994])

Moran et al. [1994] defined/assumed the dry edge and wet edge respectively as the linear line connecting vertex (2) with vertex (4) and the linear line linking vertices between vertex (1) and vertex (3), as displayed in Fig.1-4. WDI within each VI from bare soil to full vegetation cover in the trapezoid is linearly related to the maximum and minimum temperature differences (T_s-T_a) and values of WDI equal to 0 and 1 respectively correspond to minimum and maximum temperature differences. Therefore, for a partially vegetated surface, WDI can be defined as:

$$WDI = 1 - LE / LE_P = [(T_s - T_a)_{\min} - (T_s - T_a)_i]/[(T_s - T_a)_{\min} - (T_s - T_a)_{\max}] \tag{1.29}$$

The trapezoid method is in essence an extension of CWSI developed by Idso et al. [1981] and Jackson et al. [1981]. CWSI is a commonly used index for detection of plant water stress based on the difference between canopy and air temperature and is only appropriate to apply for full-cover vegetated areas and bare soils at local and regional scales [Moran et al., 1994]. Idso et al. [1981] proposed an empirical CWSI to quantify canopy stress by determining 'non-water-stressed baselines' for crops, in which the baselines represented the lower limit of the difference of canopy to air temperature when the plants are transpiring at the potential rate. Shortly, Jackson et al. [1981; 1988] defined the theoretical CWSI by ratioing the difference between the measured canopy temperature and the lower limit (corresponding to canopy transpiring potentially) to the difference between the upper (corresponding to non-transpiring canopy) and lower limits. The trapezoid method ((T_s-T_a)-SAVI) is a method to measure the surface water stress based on the formed trapezoid given a full range of surface vegetation cover and soil moisture content when the difference between surface and air temperature is plotted against a vegetation index [Moran et al., 1994; 1996]. Kustas and Norman [1996] have found that this trapezoid method permitted the concept of CWSI applicable to both heterogeneous and uniform areas and did not require the range of VI and surface temperature in the scene of interest as that proposed by Carlson et al. [1990] and Price [1990]. Luquet et al. [2004] evaluated the impact of complex thermal infrared directional effects on the application of WDI using multidirectional crop surface temperatures and reflectance data acquired on a row-cotton crop with different water and cover conditions in Montpellier (France). Results from the work of Moran et al. [1994] showed that the WDI provided accurate estimates of field ET rates and relative field water deficit for both full cover and partially vegetated sites.

One of the advantages in the VI-T_s trapezoidal space over the triangular space is that the VI-T_s trapezoidal space does not require as large number of pixels to be existent as that in the triangular space. Instead, the intermediate values in the trapezoidal space are determined by the four limiting vertices. However, the relatively more ground-based parameters in the VI-T_s trapezoidal space than that in the triangular space have constrained the broad applications of the trapezoidal space. Some limitations have also emerged in WDI although this new index offers large opportunity than CWSI [Luquet et al., 2004], including that 1) there are no consideration of heat exchanges between soil and vegetation, which may be not valid when soil and vegetation are at different temperatures, 2) water stress does not have instantaneous effect on vegetation cover, 3) WDI method does not separate plant transpiration from soil evaporation.

1.1.2.2 Dual-source model

Dual-source model is also called Two-source model.

Although single-source energy balance models may provide reliable estimates of turbulent heat fluxes, they often need field calibration and hence may be unable to be applied over diverse range of surface conditions. Kustas and Daughtry [1990] have shown that single-source models had serious limitations over partially vegetative surfaces though some adjustments to r_a can be made but such adjustments are not generally applicable to all circumstances. Errors in sensor calibration, atmospheric corrections, and the specification of the surface emissivity have been detrimental to methods that rely on absolute surface temperature or surface-air temperature difference to derive regional surface energy balance [Mecikalski et al., 1999]. Furthermore, air temperature measured at a shelter-level as an upper boundary condition suffers significantly from the interpolations over large heterogeneous areas [Mecikalski et al., 1999]. Dual-source models require no a priori calibration and do not need additional ground-based information as that required in a single-source model and therefore have a wider range of applicability without resorting to any additional input data. Anderson et al. [1997] showed that dual-source models represented an advance over single-source surface models that treated the earth's surface as a single, uniform layer. However, assumptions on and solution of dual-source energy balance models generally involve an estimation of the divergence of surface energy balance inside the canopy and the way to account for the clumped vegetation, which affects both the wind speed profile and radiation penetration and radiative surface temperature partitioning between soil and vegetation [Kustas and Norman, 2000].

Generally speaking, the solution of a dual-source energy balance model is to implement the decomposition of the soil and canopy component temperatures either by iterating latent heat fluxes with the assumption that the vegetation is unstressed and transpiring at the potential rate or by acquiring remote sensing data of surface temperatures at multiple angles for the calculation of the component energy balance of soil and vegetation respectively.

The ensemble directional radiometric surface temperature ($T_{RAD}(\theta)$) is determined by the respective fraction of soil and vegetation viewed by a radiometer, which can be expressed as:

$$T_{RAD}(\theta) = [\, f(\theta)T_c^M + (1 - f(\theta))T_0^M\,]^{1/M} \tag{1.30}$$

where M is usually set to 4 for 8-14 μm and 10-12 μm wavelength bands. $f(\theta)$ is vegetation fraction viewed at angle θ, T_c and T_0 are component of vegetation and soil temperature respectively.

If the surface emissivity and sky conditions are known, the directional radiometric temperature can be calculated from the brightness temperature ($T_B(\theta)$) from the following formula:

$$T_B(\theta) = [\varepsilon(\theta)(T_{RAD}(\theta))^M + (1 - \varepsilon(\theta))T_{SKY}\,]^{1/M} \tag{1.31}$$

With the assumption that the flux of soil surface is in parallel with the flux of leaves of canopy, and with a first-guess estimate of canopy transpiration (LE_c) using Priestly-Taylor equation, which often leads an over-prediction in semiarid and arid ecosystems, H in a two source model can be divided into two parts of energy component of soil and vegetation:

$$H = \rho c_p \frac{T_{RAD}(\theta) - T_a}{r_c} = H_s + H_c = \rho c_p \left(\frac{T_0 - T_a}{r_a + r_s} + \frac{T_c - T_a}{r_a}\right) \tag{1.32}$$

Inputs to dual-source energy balance models generally include directional brightness temperature, viewing angle, fractional vegetation cover or leaf area index, vegetation height and approximate leaf size, net radiation, air temperature and wind speed. If measurements of T_a, u, measurement heights, $T_{RAD}(\theta)$ measured simultaneously at two viewing angles (e.g., data available from ATSR), canopy height (h), approximate leaf size, and fraction of vegetative cover (F_r) or LAI are given, T_c, T_0, H_c, H_s, LE_c and LE_s can then be solved directly with the dual-source surface energy balance models without resorting to empirically determined 'adjustment' factors for "excess" resistance [Kustas and Norman, 1997; 1999].

A series of papers have concentrated on the respective temperature and radiation components of both soil and vegetation through a set of applications, validations and modifications to the dual-source energy balance models over various landscapes over the past years [Shuttleworth and Wallace, 1985; Shuttleworth and Gurney, 1990; Norman et al., 1995; Kustas and Norman, 1997; 1999; Norman et al., 2000; Norman et al., 2003; Anderson et al., 2004; Mecikalski et al., 2005; Anderson et al., 2005; Li et al., 2005; Sánchez et al., 2008]. The increase of surface temperature in the morning was also found to be highly sensitive to the change of surface soil moisture (and thus ET) [Idso et al., 1975c; Price, 1980; Carlson and Buffum, 1989; Carlson et al., 1981, Wetzel et al., 1984; Diak, 1990; Franks and Beven, 1997] and an utilization of rate of surface temperature rise in the form of simplified equation has also been shown by Carlson and Buffum [1989] to estimate daily ET with the advantages of no need for absolute surface temperature retrievals from satellite data. Wetzel et al. [1984] and Diak [1990] have attempted to compute surface energy balance by using the rate of rise of T_s from a geostationary satellite with an atmospheric boundary layer model. Norman et al. [1995] developed a TSM (Two-Source (soil+canopy) Model) to accommodate the difference between radiometric surface and aerodynamic temperatures to partition surface energy balance into energy components of both soil and vegetation using data either from a single view angle or from multiple view angles. Subsequently, on the basis of that work, Anderson et al. [1997] examined and tested the TSTIM (Two-Source Time Integrated Model, subsequently was named as ALEXI: Atmosphere-Land Exchange Inverse [Mecikalski et al., 1999]) relating the morning rise of surface temperature acquired at 1.5 and 5.5 hours past sunrise to the growth of a planetary boundary layer through an estimate of sensible heat using data collected during ISLSCP (the International Satellite Land-Surface Climatology Project) and Monsoon '90 experiments. Lhomme and Elguero [1999] have commented on the assumption on the parallel transfer of heat from canopy and soil and assumed the scale to be a determinant of whether a dual-source model should be coupled or not. Since 1999, ALEXI has been applicable over a wide variety of landscape, agricultural and land-surface-atmosphere interactions [Mecikalski et al., 2005]. It removes the need for the measurements of near-surface air temperature and is relatively insensitive to uncertainties in surface emissivity and atmospheric corrections on the remotely sensed surface temperatures. Kustas and Norman [2000] made four modifications, which had largest impacts on dual-source flux predictions under sparse canopy-covered conditions to the TSM developed by Norman et al. [1995], involving: 1) the estimation of the divergence of net radiation with a more physically-based algorithm, 2) use of a simple model to account for the effects of clumped vegetation, 3) application of an adjusted Priestley-Taylor [Priestley and Taylor, 1972] coefficient, 4) computation of soil resistance to sensible heat flux transfer with a new formulation. Norman et al. [2000] developed a variation of TSM called DTD (Dual-temperature-difference) method using time rate of change in T_s and T_a to derive surface turbulent fluxes and this DTD method is simpler than other modifications of TSM in that it requires minimal ground-based data and does not require modeling boundary layer development. On the basis of TSTIM, a two-step approach called DISALEXI (Disaggregated ALEXI) model has been proposed to estimate surface ET with the combination of low- and high-resolution remotely sensed data without a need for local observations [Norman et al., 2000; Kustas et al., 2003]. Anderson et al. [2005] have found that consideration of vegetation clumping within the thermal model could significantly improve the estimates of turbulent heat fluxes at both local and watershed scales when observations from eddy covariance data collected by aircraft and a ground-based tower network are compared. Li et al. [2005] compared two resistance network formulations that are used in a dual-source model for parameterizing soil and canopy energy exchanges over a wide range of soybean and corn crop cover and soil moisture conditions during the Soil Moisture–Atmosphere Coupling Experiment. In the two resistance formulations, the parallel resistance formulation does not consider interaction between the soil and canopy fluxes while the series resistance algorithms provide interaction via the computation of a within-air canopy temperature. Results from Li et al. [2005] showed that both the parallel and series resistance formulations produced basically similar estimates compared with the tower-based flux observations while the parallel resistance formulation was more able to achieve the balance of the component temperature and heat fluxes of soil and canopy.

Compared to other types of remote sensing ET formulations, dual-source energy balance models have been shown to be robust for a wide range of landscape and hydro-meteorological conditions [Kustas and Norman, 1997]. The ALEXI approach is believed to be a practical means to operational estimates of surface fluxes over continental scales with the spatial resolution of 5- to 10-km.

The main advantages of the dual-source models over single-source models are that 1) they avoids the need for precise atmospheric corrections, emissivity estimations and high accuracy in sensor calibration, 2) ground-based measurement of T_a is not indispensable when dual-source models are coupled with a PBL [Kustas and Norman, 1996] and thus is much better suitable to applications over large-scale regions than single-source models and other algorithms [Anderson et al. 1997], 3) they generally incorporate effects of view geometry, 4) they avoid empirical corrections for the ‘excess resistance’. However, applications of the aforementioned models of both directly relating surface turbulent fluxes to temperature difference measured at two times and imbedding the morning temperature rise into a dual-source energy balance coupled with a PBL (Planetary Boundary Layer) generally require a geo-stationary satellite, which is less suitable for high latitudes due to the suboptimal viewing orientation and coarse spatial resolution to provide a series of cloud-free images [Van den Hurk, 2001]. The new MSG/SEVIRI sensor has provided a good promise with its relatively small pixel size and high observation frequency for applications in Europe and Africa.

1.1.3 Data assimilation

Results from remote sensing ET models are generally either instantaneous (daily) values using data from polar-orbiting satellites or coarse spatial resolution values from geostationary satellites, which can not provide temporally continuous values and thus can not meet the requirements in most hydrological and numerical prediction models. One possible means to overcome this dilemma is to use data assimilation technique to map ET, which can take advantage of the synergy of multisensor/ multiplatform observations [Boni et al., 2001; Reichle, 2008].

Data assimilation has been firstly used by meteorologist to construct daily weather maps, displaying variations of environmental variables such as pressure and wind velocity over space and time [McLaughlin, 1995]. Simply speaking, data assimilation technique is the process in which all available information is used in order to estimate objective variables as accurately as possible [Talagrand, 1997; Bouttier and Courtier, 1999]. A data assimilation system is generally consisted of three components: a set of observations, a dynamic model and a data assimilation technique [Robinson and Lermusiaux, 2000]. All existing assimilation algorithms can be described as more or less an approximate of statistical linear estimation [Rabier et al., 1993]. Data assimilation schemes are often statistically optimal by minimizing the errors in estimates derived from merging noisy observations and uncertainty of models in a statistical sense.

Data assimilation techniques for ET estimate can assimilate all available information but it generally has to rely on a numerical model which may need a lot of atmospheric forcing and is relatively computationally demanding than remote sensing ET models [Mclaughlin et al., 2006; Kumar et al., 2008]. Selection of a data assimilation technique is essentially to achieve a balance between making the best use of all available information (optimality) and computational efficiency, flexibility, and robustness. However, compromises have to be made to adapt to specific goals because these evaluation criteria often conflict [Margulis et al., 2002]. The principle of any data assimilation scheme is to minimize the mismatch between the observations and models by adjusting components under the fundamental physical constraints.

Nowadays, data assimilation techniques are generally put into two categories, including sequential assimilation (e.g., Ensemble Kalman Filter and optimal interpolation) [Anderson, 2001; Reichle et al., 2002; Reichle, 2002; Caparrini et al., 2004; Crow and Kustas, 2005; Margulis et al., 2005; Huang et al., 2008] and un-sequential/variational/retrospective assimilation (e.g., 4-dimentional variational assimilation) [Županski and Mesinger, 1995; Courtier et al., 1998; Margulis and Entekhabi, 2003; Seo et al., 2003; Caparrini and Castelli, 2004]. One of the distinctions between sequential and variational assimilations is that in sequential assimilation each individual observation influences the estimated state of the flow only at later times and not at previous times while variational assimilation aims at adjusting the model solution globally to all the observations available over the assimilation period [Talagrand, 1997]. Several papers have attempted to use data assimilation techniques combined with a numerical model to estimate regional surface turbulent heat fluxes [Boni et al., 2001; Caparrini et al., 2004; Crow and Kustas, 2005; Margulis et al., 2005; Pipunic et al., 2008]. Boni et al. [2001] developed a land data assimilation system to estimate latent heat flux and surface control on evaporation with the dynamic equations for surface temperature as the constraint. In this assimilation system, satellite remotely sensed surface temperatures are assimilated within the Southern Great Plain 1997 hydrology field experiment. Factors characterizing land surface influences on evaporation and surface heat fluxes are estimated through assimilation of radiometric surface temperature sequences with a land surface energy balance as a constraint and this approach has been tested using data from the ISLSCP FIFE (International Satellite Land Surface Climatology Project) [Caparrini et al., 2004]. Caparrini et al. [2003] proposed a land data assimilation scheme with sequences of multi-satellite remotely sensed surface temperature measurements and data from surface micrometeorological stations to estimate the surface energy balance components in a basin with varying surface conditions. Margulis et al. [2005] compared the VI-Ts triangle method to variational data assimilation method for estimating surface turbulent fluxes from radiometric surface temperature observations. Results from a set of synthetic experiments and an application of data from ISLSCP FIFE site have shown that the assimilation approach performs slightly better than the VI-Ts triangle method.

Data assimilation approach to map surface energy fluxes often has some advantages over traditional retrieval methods, including 1) assimilation procedure estimates not only latent heat flux but also the various intermediate variables related to the turbulent heat fluxes in a numerical model, 2) estimates of the turbulent heat fluxes are continuous in time and space since the dynamic models used in the assimilation procedure interpolate the measurements taken at discrete sampling times, 3) the data assimilation procedure can produce estimates at a much finer resolution, 4) data assimilation scheme can merge spatially distributed information obtained from many data sources with different resolutions, coverage, and uncertainties [Margulis et al., 2002]. The main drawback of data assimilation technique to retrieve regional ET with a numerical model is that it is relatively computationally demanding than the remote sensing ET models.

Above mentioned sub-sections detail the theory, advantages and weaknesses of the various remote sensing ET models from the simplified empirical regression method applied over a field scale to the relatively complex dual-source surface energy balance models employed at both regional and continental scales. Data assimilation approaches can assimilate all available data sources to provide the spatially and temporally continuous surface turbulent heat fluxes. Comparisons of the different remote sensing ET models reviewed above are recapitulated in Table 1-1.

Table 1-1. Comparisons of a variety of commonly applied remote sensing ET methods

METHODS	REFS.	EQS.	MAIN INPUTS	MAIN ASSUMPTIONS	ADVANTAGES	DISADVANTAGES
Simplified Equation	[Seguin and Itier, 1983] [Jackson et al., 1977]	Eq.(1.1)	R_{nd}, T_s, T_a	1) Daily soil heat flux is negligible; 2) Instantaneous *H* at midday can express the influence of partitioning daily available energy into turbulent fluxes.	Simplicity	Site-specific
VI-Ts Triangle	[Jiang and Islam, 1999]	Eq.(1.28)	R_n, G, T_s, VI	1) Complete range of both soil moisture and vegetation coverage exists within the study area at satellite pixel scale; 2) cloud contaminations are discarded and atmospheric effects are removed; 3) EF varies linearly with Ts for a given VI	No ground-based measurements are needed	1) Difficult to determine the dry and wet edges; 2) VI-Ts triangle form is not easy recognized with coarse spatial resolution data
VI-Ts Trapezoid	[Moran et al., 1994]	Eq.(1.29)	T_a,VPD, u, T_s,VI, R_n, G	1) Dry and wet edges are linear lines and vary linearly with VI 2) EF varies linearly with Ts for a given VI.	Whole range of VI and soil moisture in the scene of interest is not required;	1) Uncertainty in the determination of dry and wet edges; 2) lot of ground - based measurements are needed.
SEBI	[Menenti and Choudhury, 1993]	Eq.(1.17)	T_{pbl}, h_{pbl}, u, T_s, R_n, G	1) Dry limit has a zero surface ET; 2) Wet limit evaporates potentially.	Directly relating the effects of Ts and r_a on LE.	Ground-based measurements are needed.
SEBAL	[Bastiaanssen et al., 1998]	Eq.(1.26)	u, z_a, T_s, VI, R_n, G	1) Linear relationship between Ts and dT; 2) ET of the driest pixel is 0; 3) ETwet is set to the surface available energy.	1) Minimum ground measurements 2) Automatic internal calibration; 3) Accurate atmospheric corrections are not needed	1) Applied over flat surfaces; 2) Uncertainty in the determination of anchor pixels.
S-SEBI	[Roerink et al., 2000a]	Eq.(1.25)	T_s, α_s, R_n, G	1) EF varies linearly with Ts for a given surface albedo.	No ground-based measurements are needed	Extreme temperatures have to be location specific.

METHODS	REFS.	EQS.	MAIN INPUTS	MAIN ASSUMPTIONS	ADVANTAGES	DISADVANTAGES
				2) $T_{s,max}$ corresponds to the minimum LE. 3) $T_{s,min}$ corresponds to the maximum LE.		
SEBS	[Su, 2002]	Eq.(1.20)	T_a, z_a u, T_s, R_n, G	1) At the dry limit, ET is set to 0; 2) At the wet limit, ET takes place at potential rate.	1) Uncertainty in SEBS from Ts and meteorological variables can be limited and reduced; 2) Computing explicitly the roughness height for heat transfer instead of using fixed values.	1) Too many parameters are required 2) Solution of the turbulent heat fluxes is relatively complex.
METRIC	[Allen et al., 2007] [Allen et al., 2005]	Eq.(1.26)	u, z_a, T_s, VI, R_n, G,	1) For the hot pixel, ET is equal to zero 2) For the wet pixel, LE is set to $1.05ET_r$.	Same as SEBAL but surface slope and aspect can be considered.	Uncertainty in the determination of anchor pixels.
TSM	[Norman et al., 1995]	Soil and canopy energy budgets	u, z_a T_a, T_s, T_c, F_r or LAI, R_n, G	1) Fluxes of soil surfaces are in parallel or in series with fluxes of canopy leaves; 2) Priestly-Taylor Eq. is employed to give the first-guess of canopy transpiration	1) Effects of view geometry are taken into account; 2) Empirical corrections for the ‘excess resistance’ are not needed;	1) Many ground measurements are needed. 2) Component temperatures of soil and vegetation are required.
TSTIM/ ALEXI	[Mecikalski et al., 1999]	Soil and canopy energy budgets	u, z_a dTs, F_r or LAI, R_n, G.	Surface temperature changes linearly with the time during the morning hours of the sensible heating	Errors due to atmospheric corrections and surface emissivity specification are significantly reduced;	Determination of an optimal pair of thermal observation times for the linear rise in sensible heating is needed.

1.2 Scaling from instantaneous ET to daytime integrated value

Most of the aforementioned ET models using remotely sensed data produce only instantaneous ET values. Obviously, it is necessary to convert essentially instantaneous ET value at the overpass times of satellites to daily or longer time value to make full use of the remote sensing data in hydrological and water resources management applications. A number of techniques are proposed to extrapolate the instantaneous ET to the longer time values, mainly including sine function, constant evaporative fraction (EF), constant reference ET fraction (ETrF).

1.2.1 Sine function

Jackson et al. [1983] related the ratio of instantaneous ET to daily value to the diurnal trend of solar irradiance with the following equation:

$$ET_d / ET_i = R_{sd} / R_{si} = 2N/(\pi \sin(\pi t / N)) \tag{1.33}$$

where subscripts *d* and *i* respectively indicate the daily total and instantaneous values. The sine function gives a good approximate of the change of diurnal solar irradiance except near sunrise and sunset. *t* is the duration time starting at sunrise. *N* is the duration of daytime and can be expressed as:

$$N = 0.945(a + b\sin^2(\pi(D_y + 10)/365)) \tag{1.34}$$

$$a = 12.0 - 5.69\times10^{-2}\lambda - 2.02\times10^{-4}\lambda^2 + 8.25\times10^{-6}\lambda^3 - 3.15\times10^{-7}\lambda^4 \tag{1.35}$$

$$b = 0.123\lambda - 3.10\times10^{-4}\lambda^2 + 8.00\times10^{-7}\lambda^3 + 4.99\times10^{-7}\lambda^4 \tag{1.36}$$

in which D_y is the day of year, λ is geographical latitude in degree.

With Eqs.(1.33-1.36) and time of day (t), day of year (D_y) and geographical latitude between 60^o S and 60^o N, one can scale the one-time measured instantaneous ET to the daily totals. Jackson et al. [1977] have shown that when the daytime was always cloud free or the cloud cover was relatively constant throughout the daytime, the sine function of Eq.(1.33) could obtain reliable estimates of daytime integrated ET. When cloudy days exist, improvements of Eq.(1.33) should be made to take account the mount and temporal coverage of the cloud cover. This approach is widely used for daily ET estimation and satisfactory results have been produced [Zhang and Lemeur, 1995; Kustas and Norman, 1996; Chen et al., 2005; Colaizzi et al., 2006]. Zhang et al. [1995] refined the sine function by introducing a parameter to reflect impacts of geographic latitude, solar declination and degree of cloudiness on the convexity of the diurnal patterns of solar radiation.

1.2.2 Constant Evaporative Fraction (EF)

Sugita and Brutsaert [1991] assumed the evaporative fraction to be constant during the daylight hours to determine regional daily ET using data obtained during FIFE in northeastern Kansas. Knowing the daytime available energy $(R_n\text{-}G)_d$, and assuming that EF is constant during the daytime, daily estimate of ET_d can therefore be written as:

$$LE_d = (R_n - G)_d \cdot EF_i = (R_n - G)_d \frac{LE_i}{(R_n - G)_i} \tag{1.37}$$

where subscripts *i* and *d* are respectively indicative of instantaneous and daytime integrated values. The value of EF varies from 0 to 1 under daytime convective conditions with minimal advection and represents the fraction of available energy partitioned into latent heat flux [Kustas et al., 1993].

A great number of papers have used this assumption to calculate the daily ET and examined whether the assumption that daytime EF is nearly constant throughout the day is reasonable [Shuttleworth et al., 1989; Sugita and Brutsaert, 1991; Hall et al., 1992; Kustas et al., 1993; Nichols and Cuenca, 1993; Crago, 1996; Lhomme and Elguero, 1999; Farah et al., 2004; Colaizzi et al., 2006; Hoedjesa et al., 2008]. With data from the FIFE and other observations, Crago [1996] has concluded that the variability or conservation of EF on individual day was affected by complicated combination factors, including weather conditions, soil moisture, topography, biophysical conditions, cloudiness and the advections of moisture and temperature directly contributed to the amount of variability of EF on a given day. A strong correlation with the coefficient of determination value of 0.89 has been demonstrated between the midday and daily average evaporative fractions for data from the Hapex-Mobilhy program on clear days [Nichols and Cuenca, 1993]. Zhang and Lemeur [1995] using data from the Hapex-Mobilhy Experiment in southwestern France compared the sine function with the constant EF method and concluded that both methods were accurate to estimate daily total ET for cloud-free days and recommended that the sine function was preferable for the purpose of estimating ET using remotely sensed data.

Jackson et al. [1983], Owe and van de Griend [1990] and Kustas et al. [1994] have found that nighttime ET could reach as many as about 10 percent of the daily totals. Allen et al. [2007] illustrated that the assumption of constant EF during the 24h period could underestimate the overall daily ET when afternoon advection and increased wind speed appeared in arid climates. Anderson et al. [1997] therefore added this 10 percent of latent heat fluxes into daily integrated ET in Eq. (1.37) using the evaporative fraction expressed as follows:

$$EF = 1.1 \frac{LE_i}{(R_n - G)_i} \tag{1.38}$$

1.2.3 Constant reference ET fraction (ETrF)

In the METRIC process, Allen et al. [2007] proposed a constant ET_rF, which is believed to be better able to capture any impacts of advection and changing wind and humidity conditions during the day, to estimate the 24-h total ET. ET_rF is defined as the ratio of the computed ET_i from each pixel to ET_r. ET_r. is the reference ET over the standardized 0.5 m tall alfalfa and computed from meteorological data measured at ground meteorological stations [Allen et al., 2007]:

$$ET_rF = \frac{ET_i}{ET_r} \tag{1.39}$$

$$ET_i = 3600 \frac{LE}{L \times \rho_w} \tag{1.40}$$

$$L = [2.501 - 0.00236(T_s - 273.15)] \times 10^6 \tag{1.41}$$

With the assumption of instant ET_rF being same as the average ET_rF over the 24 h average and the consideration of the sloping effects over terrain areas, ET_d can be estimated by [Allen et al., 2007]:

$$ET_d = C_{rad}(ET_r F)(ET_{r,d}) \tag{1.42}$$

$$C_{rad} = \frac{R_{s,i,Horizontal}}{R_{s,i,pixel}} \cdot \frac{R_{s,d,pixel}}{R_{s,d,Horizontal}} \tag{1.43}$$

where subscripts *i* and *d* indicate instantaneous and daily values respectively; subscripts “pixel” and “horizontal” represent respectively the value for a specific pixel at certain slope and aspect conditions and value calculated for a horizontal surface. For applications to horizontal areas, C_{rad}=1.0. $ET_{r,d}$ is cumulative daily reference ET [Allen et al., 2007].

1.3 Problems/issues

Although great progress has been made since 1970s on a number of methods from an empirical simplified equation to a more complex physically based dual-source energy balance model using the remote sensing technology to estimate regional surface turbulent fluxes, there are still some problems that have not been solved reasonably, which are mainly associated with the parameterization of land surface fluxes at regional/global scales, retrieval accuracy and physical interpretation of different surface variables retrieved from satellite data, temporal and spatial data/model scaling from one scale to other scale, validation of the latent heat flux obtained from models at regional/global scale, etc.. These problems will be discussed briefly below.

1.3.1 Problems related to remotely sensed data itself

Remotely sensed data are acquired instantaneously and can only provide instantaneous two-dimensional spatial distribution of land surface variables such as surface albedo, surface vegetation fraction, surface temperature, surface net radiation and soil moisture, etc, which are indispensable variables to know for remote sensing estimate of land surface ET. This is one of the specialities of remote sensing technique, as well as the distinct predominance of remote sensing technique in estimating spatial distribution of land surface ET at regional/global scale. These speciality and predominance have great impact on the spatial scaling from the "point" to the regional scale. However, temporally integrated daily, weekly and monthly ETs at regional and global scales are required for many ET-related disciplines. Therefore, temporal scaling, which is one of the weaknesses of remotely sensed data, is needed to convert the instantaneously spatial ET to a longer-time value. Moreover, due to the effect of cloud coverage, it is impossible to provide the two-dimensional spatial patterns of land surface variables under the clouds by the optical remote sensing and consequently impossible to estimate the surface instantaneous ET over the areas covered by clouds with optical remote sensing data. Nowadays, great progress has been made to convert the instantaneous ET to the daily value on clear-sky days while little work or progress has been done on the temporal scaling from instantaneous remote sensing ET to weekly/monthly remotely based-ET due to the coarse spatial resolution of microwave remote sensing data and the inaccuracy of the surface variables used in remote sensing models retrieved from the microwave data, as well as the effects of cloud cover.

1.3.2 Uncertainty of the remote sensing ET models

Over the past 30 years, a variety of remote sensing ET models have been developed to estimate the spatial distribution of ET at various scales ranging from the field (simplified empirical equation) to regional (single-source or dual-source models) and continental scales (eg. ALEXI). Single-source models can be applied with a relatively high accuracy over homogeneous areas (eg. dense vegetation), while over the arid and semi-arid areas (eg. partially vegetated cover) two-source models are especially required to separately model the heat interactions between soil and atmosphere and between vegetation and atmosphere. However, as reviewed in the previous sections, each model developed has its advantages and disadvantages (weaknesses) and was applied successfully to some extent to some conditions. Since, in the different areas of the world, there exist great differences in the land surface characteristics, in the climate and terrain etc., no model developed nowadays can be used everywhere in the world without any modification or improvement to estimate the ET from satellite data. A big challenge in the development of remote sensing ET model is to develop a new parameterization of land surface ET with only land surface variables and parameters directly or indirectly derived from satellite data.

1.3.3 Uncertainties in the accuracy of the retrieved land surface variables (parameters)

The presence of the atmosphere between land surface and sensors at satellite level disturbs the radiances measured by a radiometer at the top of the atmosphere. These radiances result primarily from emission/reflection of surface modulated by the effects of absorption, diffusion and emission of the atmosphere. The passage of the radiances measured at the top of the atmosphere to the macroscopic land surface parameters (variables) and physics of surfaces requires the corrections for the atmospheric effects and the connection of the surface parameters (variables) derived directly from satellite data to other surface parameters (variables) through physical models.

Although great progress has been made nowadays to retrieve quantitatively land surface variables (parameters) from remotely sensed data, accuracy of some variables (parameters), such as surface temperature, LAI, vegetative coverage, plant height, etc., required in remote sensing ET models still needs to be improved. In addition, due to the influences of vegetation architecture, sunlit fractional of vegetation and solar zenith angle, etc., observational angular effect is a significant factor affecting the retrieval of radiometric surface temperature especially over heterogeneous surfaces [Norman et al., 1995]. Differences in received radiances will occur due to the differing amounts of soil and vegetation in the filed of view when sensor viewing changes from one angle to another, while over homogeneous dense, well-watered vegetative surfaces, the effect is less important [Carlson et al., 1995a; Anderson et al., 1997]. Data obtained during the ISLSCP FIFE program have shown that difference of surface temperature obtained at nadir and 60 degrees in zenith angle can reach as large as 5 ^{o}C [Anderson et al., 1997], implying that a large and unaccepted error on ET estimate would be generated if the angular effect is neglected. In order to take into account this angular effect in the development of dual-source remote sensing ET models, methodologies must be developed to estimate accurately the component temperatures of surface (vegetation and ground) from multispectral and multi-angular satellite measurements.

1.3.4 Lack of the measurements of near-surface meteorological variables

In most remote sensing data based ET models, whatever the single-source or dual-source models are, meteorological data (air temperature, atmospheric pressure, wind speed, relative humidity) at PBL-height or at near-surface height at satellite pixel scale are indispensable and spatial interpolation method is often used to get these meteorological data at satellite pixel scale from discrete meteorological stations. Because the big difference of the climate and terrain conditions may exist in the study region and the implementation of meteorological stations is often sparse and irregular in the world, accuracy of the non-physics and merely spatial-statistics based interpolation needs to be improved either by developing physically static- or dynamic-feedback interpolation methods based on remote sensing data or by making use of atmospheric reanalysis data at high spatial-resolution. Another approach to improve the accuracy of spatial data interpolation is to integrate the remote sensing ET models with atmospheric general circulation models or numerical weather forecast models, which maybe one of the promising subjects in the future for the regional ET estimates with remotely sensed data.

1.3.5 Spatial and temporal scaling effects

Scaling problem is of nature much more fundamental since it implies a conceptual analysis of the physical significance of the measured quantities (variables). Indeed, the diversity of continental surfaces involves spatial (vertical and horizontal) and radiometric heterogeneities of surface, considering the spatial resolution of the current onboard sensors varying from 10^{-2} to 10^{1} km^2, it is therefore necessary to be able to define and interpret correctly surface parameters (variables) independent of the scale used, as well as the processes necessary to validate this definition.

Simply speaking, scaling effect in the derivation of surface turbulent fluxes is shown in the form of whether functions of parameters and variables obtained over one scale can be used at other scales (local/regional/large) [Carlson et al., 1995a]. It seems general that models applicable for deriving surface fluxes/parameters at local scale may not be appropriate for applications at a larger scale because of the heterogeneities of the surface and non-linearity of the models [Carlson et al., 1995a].

Since 1980s, several international field programs have been designed to obtain useful surface parameters and study the issue of scaling from point to regional- or global-scale estimates of the surface energy fluxes [Carlson et al., 1995a]. The spatial resolution of thermal infrared bands is usually coarser than that in visible and near infrared bands, which will lead to a scale difference in the land surface parameters indispensable to ET estimates between surface temperature obtained from thermal bands and vegetation indices derived from visible and near infrared bands [Courault et al., 2003; Gowda et al., 2007].

The possibility of resolving all problems raised by scaling effects may be to a great extent associated with the development of the scaling theory and further with the fusion of multi-scale remote sensing observations [McCabe and Wood, 2006; Gowda et al., 2007].

1.3.6 Lack of the land surface ET at satellite pixel scale for the truth validation

Comparisons between turbulent heat fluxes derived from remote sensing ET models and in-situ measured data are required to evaluate the reliability and accuracy of the applied ET models. Although it may be feasible and reasonable to validate pixel-averaged fluxes derived from remote sensing ET models with traditional measurements mainly conducted at the "point" scale over uniform areas, problems will be encountered when validation is performed over complicated land surface areas.

Nowadays, several conventional techniques such as Bowen ratio, eddy correlation system and weighing lysimeters have been commonly applied to measure the ET at ground level. Lysimeters provide the only direct measure of water flux from a vegetated surface. Its measurements can therefore be used as a standard for evaluating the performance of other physically based ET models. However, data measured by Lysimeters are essentially point data and thus cannot be used for validating the regional ET estimates [Kairu, 1991]. Study has shown that measurements from Bowen ratio and large weighing lysimeters for irrigated alfalfa during advective conditions can differ by up to 29% [Blad and Rosenberg, 1974; Todd et al., 2000]. Eddy correlation technique, based on the principle that atmospheric eddies transport the entities of water vapor, CO_2, and heat with equal facility, is particularly useful for rough surfaces with high coefficients of turbulent exchange [Kairu, 1991]. It has overtaken Bowen ratio as being the most preferred micrometeorological technique for ET measurements in the past few decades [Farahani et al., 2007]. The source area of an eddy correlation system generally represents an upwind distance of about 100 times the sensor height above the surface [Campbell and Norman, 1998], which is appropriate to validate the ET at pixel sizes of an order of hundred meters. In the past decades, most studies used measurements conducted by the Bowen Ratio Energy Balance (BREB) and the eddy correlation system to validate ET at local and regional scales. Angus and Watts [1984] showed that LE measured by Bowen ratio was dependent on the range of Bowen ratio values. For ET at the potential rate, relative errors of up to 30% in Bowen ratio can produce relative errors of 5% in LE. However, as soil water becomes less available, the precision in LE will decrease [Kalma and Jupp, 1990]. Energy balance non-closure in eddy correlation, typically higher over strongly evaporating surfaces such as irrigated crops [Farahani et al., 2007], can reach up to 20% even for non-advective conditions [Gowda et al., 2007]. Measurements from eddy correlation system at night under low wind-speed stable conditions can yield large errors and the instrument errors and atmospheric stability contribute to the sources of errors [Gurney and Camillo,1984; Shuttleworth, 2007].

Validation of remote sensing ET derived from satellite data at high spatial resolution, such as TM and ASTER (Advanced Space-borne Thermal Emission and Reflection Radiometer) data, was generally performed using the measurements made by the BREB and eddy correlation system. However, difficulties still remains in validation of ET estimated from low spatial resolution satellite data such as MODIS, GOES whose pixel size in thermal bands is a magnitude of an order of kilometers [Carlson, et al., 1995a].

The newly developed (Extra-) Large Aperture Scintillometers (XLAS, LAS) provide a promising approach to validate the remote sensing ET at much larger scales [Meijninger et al., 2002; Hoedjes et al., 2002; Hemakumara et al., 2003; Hoedjes et al., 2007]. Scintillometers are regarded as the unique possibility of measuring the sensible heat flux averaged over horizontal distances comparable to the grid size of numerical models and satellite images [Kohsiek et al., 2002] and thus can be employed to validate to a certain degree the regional turbulent heat fluxes derived from remote sensing models. One limitation of using Scintillometers is the saturation of scintillation, which can be overcome by using either large, incoherent transmitter and/or receiver apertures or a longer wavelength [Kohsiek et al., 2002; Kohsiek et al., 2006].

1.4 Main research contents and basic conclusions

Focused on the issues/problems identified above throughout a complete overview of the regional ET estimation from remotely sensed data, this work thus concerns the methodological development permitting to determine the regional land surface ET from the MODIS data onboard the polar satellites Terra and Aqua.

This thesis is composed of 6 chapters.

In the first chapter, the state of the art on the estimate of the regional ET from satellite data is presented. An overview of the commonly applied ET models using remotely sensed data is made to provide an insight into the estimate of ET over a regional scale from satellite data. The main inputs, assumptions, theory, advantages and drawbacks in each model are discussed. Moreover, approaches to the extrapolation of instantaneous ET to the daily values are also briefly presented. In the final part, associated problems regarding these remotely sensed ET models are analyzed to show objectively the limitations and promising aspects of the estimation of regional ET based on remotely sensed data and ground-based measurements and the structure of this thesis is also briefly given in this chapter.

The second chapter of this thesis is devoted to the determination of land surface temperature (LST) from the Chinese geostationary meteorological satellite data - FengYun 2C (FY-2C). Land surface temperature is recognized to be one of the priority parameters and made special attentions in the study of our environment and in the estimate of ET. On the basis of the radiative transfer theory, this chapter addresses the retrieval of the LST from the FY-2C data in two thermal infrared channels IR1 (10.3-11.3μm) and IR2 (11.5-12.5μm), using the Generalized Split-Window (GSW) algorithm. This chapter is broken up into 4 parts. The first describes the theory associated with the LST retrieval using the GSW algorithm and presents the algorithm development for FY-2C data. The second gives the results and the numerical values of the coefficients in the GSW algorithm. The sensitivity and error analyses in term of the uncertainty of the Land Surface Emissivity (LSE) and Water Vapor Content (WVC) in the atmosphere as well as the instrumental noise are also presented in this part. In addition, in order to compare the different formulations of the split-window algorithms, this part gives also the intercomparsion of the LSTs estimated by several split-window algorithms. The third part presents the main results obtained in this work. The fourth part gives an example of retrieving LST from FY-2C satellite data and conclusions of this chapter.

We approach in the third chapter the restitution of the directional land surface emissivity from the combination of the MODIS TIR data and MODIS mid-infrared (MIR) data with emphasis on the modeling of the land surface bidirectional reflectivity in MIR channel. The first part of this chapter describes the methodology to retrieve directional emissivity and the development of BRDF model in MIR region. The second describes the study area, MODIS data and data processing for estimating directional emissivity from MODIS data. The third part presents some preliminary results and cross-validation with the MODIS land surface temperature/emissivity product MYD11B1 data. The last part will give the conclusion of this chapter.

The fourth chapter is devoted to study the impact of spatial heterogeneity of leaf area index (LAI) on the estimate of directional gap fraction. Directional gap probability or gap fraction is a basic parameter in the optical remote sensing modeling and is closely related to the vegetation fraction required by most of the ET models. The first part of this chapter provides the theoretical framework to estimate the scaling effect of directional gap probability raised by two different aggregation schemes from local scale to larger scale. In the second part, we present the different types of remotely sensed LAI images obtained from VALERI database. In the third part, the scaling effect associated with the non-linear relationship between LAI and gap probability is quantified over several types of landscape and a new parameter is introduced to compensate the scaling effect. In the last part, a conclusion of this chapter is given.

The fifth chapter is devoted to the estimation of regional ET from MODIS data over arid and semi-arid regions. The first part of this chapter recalls the principle of the T_s-VI triangle method and highlights the assumptions involved in the methodological development and the advantages and disadvantages of the T_s-VI method. The second part is devoted to the development of a practical algorithm for quantitative determination of dry and wet edges in the T_s-VI triangle from MODIS/Terra data and products. The third part describes the study region and data used in the present study and gives a preliminary validation of satellite derived sensible heat flux with the field measurements made by the LAS during the Heihe Field Experiment from May 20th to August 21st, 2008. The last part gives the conclusion of this chapter.

The sixth chapter is mainly devoted to the conclusions of this thesis and gives some future trends and prospects.

Chapter 2

Generalized Split-Window Algorithm for Estimate of Land Surface Temperature from Chinese Geostationary FengYun Meteorological Satellite (FY-2C) Data

Land Surface Temperature (LST) is not only a good indicator of both the energy equilibrium of the Earth's surface and greenhouse effects, but is also one of the key variables controlling fundamental biosphere and geosphere interactions between the Earth's surface and its atmosphere. It can play either a direct role such as when estimating longwave fluxes, or indirectly as when estimating latent and sensible heat fluxes [Mannstein, 1987; Sellers et al., 1988]. Moreover, many other applications, such as evaportranspiration modeling [Serafini, 1987; Bussieres et al., 1990], estimating soil moisture [Price, 1980], and climatic, hydrological, ecological and biogeochemical studying [Schmugge and André, 1991; Running et al., 1994] and so on, rely on the knowledge of LST. Consequently, it is crucial to have access to reliable estimates of surface temperature over large spatial and temporal scales. It is practically impossible to obtain such information from ground based measurements, whereas the satellite observations in the Thermal Infra-Red (TIR) appears to be very attractive since it can give access to global and temporal estimates of LST.

However, the retrieval of the LST from satellite data is a very difficult task because, besides the radiometric calibration and the cloud screening procedures, three types of corrections have to be made. They are emissivity corrections, atmospheric corrections and topography corrections [Price, 1984]. Up to now, many algorithms for estimating the LST from satellite observations have been proposed. They may be roughly grouped into three categories: the single channel algorithm [Ottlé and Vidal-Madjar, 1992; Jiménez-Muñoz and Sobrino, 2003], the split window algorithm [McMillin, 1975; Becker and Li, 1990] and the triple window algorithm [Sun and Pinker, 2003].

The single channel method is a simple inversion of the radiative transfer equation providing that the Land Surface Emissivities (LSEs) and the atmospheric profiles are known in advance. The triple window method combines two thermal window channels and one middle infrared channel to estimate the LST for nighttime satellite observations. The split window method is used to retrieve the LST based on the differential water vapor absorption in two adjacent infrared channels. This method was firstly proposed by McMillin [1975] to estimate sea surface temperature from satellite measurements. Since then, a variety of split window algorithm have been developed and modified to retrieve LST, and, currently, most of them have been successfully applied to the LST retrieval from the data observed by the AVHRR, MODIS, and Spinning Enhanced Visible and Infrared Imager (SEVIRI) instruments [Price, 1984; Becker and Li, 1990; Prata and Platt, 1991; Vidal, 1991; Ulivieri et al., 1992; Sobrino et al., 1993; Sobrino et al., 1994; Coll and Caselles, 1997; Becker and Li, 1995; Wan and Dozier, 1996; Sobrino and Romaguera, 2004].

The FengYun-2C (FY-2C), a geostationary meteorological satellite developed by Shanghai Academy of Space Flight Technology (SAST, also known as 8th Space Academy) and China Academy of Space Technology (CAST, also know as 5th Space Academy) and operated by China Meteorological Administration (CMA), was launched on 19 October 2004 and is becoming fully operational in 2006. The FY-2C is the Chinese first operational meteorological satellite, which was also the fourth satellite of the FY series and is located above the Equator at longitude 105° E, and some 35,800 km away. The objective of the mission is to monitor the temperature and the clouds above China and neighboring areas and also to provide meteorological information for the Asia-Pacific region. The upgraded Stretched-Visible and Infrared Spin-Scan Radiometer (S-VISSR) is one of the major payloads onboard the FY-2C. This optical imaging radiometer consists of one visible channel and four infrared channels. The characteristics of the instrument are shown in Table 2-1. It can acquire one full disc image covering the Earth surface from 60° N to 60° S in latitude and from 45° E to 165° E in longitude per hour and 30 min per acquisition for flood season.

Table 2-1. Specifications of S-VISSR channels: spectral range and spatial resolutions.

Channel no.	Channel name	Spectral range (μm)	Spatial resolution (km)
1	IR1	10.3-11.3	5
2	IR2	11.5-12.5	5
3	IR3	6.3-7.6	5
4	IR4	3.5-4.0	5
5	VIS	0.55-0.90	1.25

The work presented in this chapter aims to retrieve LST from the FY-2C satellite data in two thermal infrared channels (IR1, 10.3-11.3 μm and IR2, 11.5-12.5 μm), using the Generalized Split-Window (GSW) algorithm proposed by Wan and Dozier [1996]. Section 2.1 describes the theory associated with the LST retrieval using the GSW algorithm and presents the algorithm development for FY-2C data. Section 2.2 gives the results and the numerical values of the coefficients in the GSW algorithm. The sensitivity and error analyses in term of the uncertainty of the LSE and Water Vapor Content (WVC) in the atmosphere as well as the instrumental noise are also presented in this section. In addition, in order to compare the different formulations of the split-window algorithms, this section gives the intercomparsion of the LSTs estimated by several split-window algorithms. Section 2.3 gives an example of retrieving LST from FY-2C satellite data. The Conclusion is drawn in Section 2.4.

2.1 Theory

2.1.1 Radiative transfer for split-window algorithm

On the basis of the radiative transfer theory, for a cloud-free atmosphere under thermodynamic equilibrium, the channel radiance $B_i(T_i)$ measured at the Top Of the Atmosphere (TOA) in a Thermal Infra-Red (TIR) channel of the sensor onboard the satellite, is given with a good approximation as [Li et al., 2000]

$$B_i(T_i) = \varepsilon_i B_i(T_s)\tau_i + R^{\uparrow}_{atm\_i} + (1-\varepsilon_i)R^{\downarrow}_{atm\_i}\tau_i \tag{2.1}$$

where T_i is the channel brightness temperature observed in channel i at the TOA, B_i is the Planck function, $B_i(T_s)$ is the radiance measured if the surface was a blackbody with surface temperature T_s, ε_i is the channel emissivity in channel i, τ_i is the total atmospheric transmittance along the target to sensor path in channel i, $R^{\uparrow}_{atm\_i}$ is the thermal path atmospheric upwelling radiance in channel i, and $R^{\downarrow}_{atm\_i}$ is the channel downwelling atmospheric radiance from the whole hemisphere in channel i divided by π. The first term on the right hand side of Eq. (2.1) represents the surface emission that is attenuated by the atmosphere. The second term represents the upwelling atmosphere emission toward the sensor and the third term represents the downwelling atmosphere emission that is reflected by the surface and reaches the sensor.

Inverting Eq.(2.1), one can get

$$T_s = B^{-1}[\frac{B_i(T_i) - R^{\uparrow}_{atm\_i} - (1-\varepsilon_i)R^{\downarrow}_{atm\_i}\tau_i}{\varepsilon_i \tau_i}] \tag{2.2}$$

in which B^{-1} is the inverse of the Planck function. Once the channel emissivity ε_i is known, there are two ways to estimate the LST from satellite data. One way is to use Eq. (2.2) with atmospheric radiative transfer model such as MODTRAN 4 [Berk et al., 1998] or 4A/OP [Scott and Chédin, 1981], if the atmospheric profile is available from either conventional radiosoundings or satellite soundings. Another is to employ the split-window algorithm developed on the basis of the differential water vapor absorption in two adjacent infrared channels [McMillin, 1975] if the atmospheric profile is not available.

As S-VISSR sensor onboard FY-2C has two adjacent thermal infrared channels (IR1 and IR2), the GSW algorithm proposed by Becker and Li [1990] and Wan and Dozier [1996] is adopted to estimate the LST from FY-2C satellite data. According to GSW algorithm, the LST can be expressed as

$$T_s = a_0 + (a_1 + a_2\frac{1-\varepsilon}{\varepsilon} + a_3\frac{\Delta\varepsilon}{\varepsilon^2})\frac{T_i + T_j}{2} + (a_4 + a_5\frac{1-\varepsilon}{\varepsilon} + a_6\frac{\Delta\varepsilon}{\varepsilon^2})\frac{T_i - T_j}{2} \tag{2.3}$$

with $\varepsilon = (\varepsilon_i + \varepsilon_j)/2$ and $\Delta\varepsilon = \varepsilon_i - \varepsilon_j$. Where T_i and T_j are the TOA brightness temperatures measured in channels i (11.0 μm) and j (12.0 μm), respectively; ε_i and ε_j are, respectively, the land surface emissivities in channels i and j; ε is the averaged emissivity; $\Delta\varepsilon$ is the emissivity difference between the two adjacent channels; and $a_0 - a_6$ are unknown coefficients which will be derived below from simulated FY-2C data..

2.1.2 Algorithm development for FY-2C

So far, as there is no available database of in situ LST measurements in coincidence with the FY-2C overpasses, the only possible way to obtain the coefficient in Eq. (2.3) is to use numerical simulation for establishing the database used in the statistical regression. To this end, the atmospheric radiative transfer model MODTRAN 4 was used to simulate the TOA radiance with the appropriate thermal infrared channel response function of the S-VISSR onboard FY-2C.

Keeping in mind that a practical LST algorithm should accommodate atmospheric variations wide enough to cover all possible real situations, two atmospheric profiles databases were taken into account in our simulation. One is the latest version of the Thermodynamic Initial Guess Retrieval (TIGR) database TIGR2002, which was constructed by the Laboratoire de Meteorologie Dynamique (LMD) and represents a worldwide set of atmospheric situations (2311 radiosoundings) from polar to tropical atmospheres with varying water vapor amounts ranging from 0.1 to 8 g/cm^2

(http://ara.lmd.polytechnique.fr/htdocs-public/products/TIGR/TIGR.html). The other is the six standard atmospheric profiles (tropical, mid-latitude summer, mid-latitude winter, sub-arctic summer, sub-arctic winter, and US76) stored in the MODTRAN 4. For LST retrieval, we only consider atmospheric variation in clear-sky conditions. Consequently, the profiles with relative humidity at one of levels greater than 90% in TIGR2002 were discarded as this seldom happens under clear-sky conditions. Therefore, 1413 representative atmospheric situations were extracted from TIGR2002. Fig.2-1 shows a plot of the atmospheric Water Vapor Content (WVC) as function of the atmospheric temperature T_{a_1st} in the first boundary layer of these selected atmospheres. As shown in this Fig. 2-1, the T_{a_1st} varies from 231 K to 315 K and the atmospheric WVC changes from 0.06 g/cm^2 to 6.44 g/cm^2.

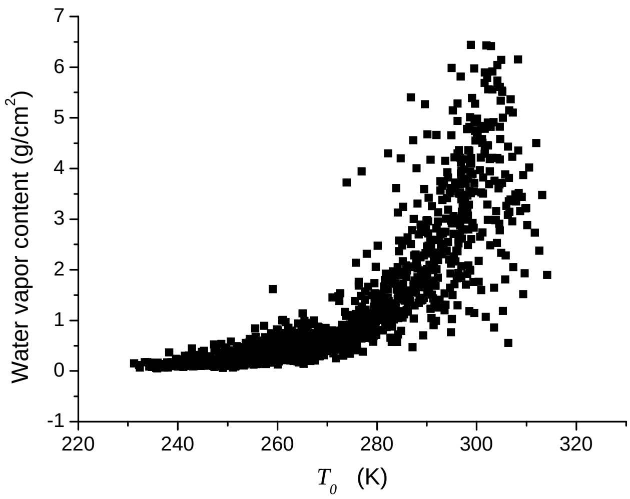

Fig.2-1 Plot of the atmospheric water vapor content as function of atmospheric temperature T_{a_1st} in the first boundary layer of the selected 1413 atmospheric profiles in TIGR2002.

Taking into account the angular dependence of the TOA radiance, six different Viewing Zenith Angles (VZAs) (0°, 33.56°, 44.42°, 51.32°, 56.25°, 60°) varying from 0° to 60° were used in MODTRAN simulations. With the VZAs and the radiosoundings mentioned above as MODTRAN input, we can obtain the channel atmospheric parameters (τ_i, $R^{\uparrow}_{atm\_i}$, $R^{\downarrow}_{atm\_i}$) with spectral integration of the channel response function for each VZA and each atmospheric profile.

In addition, in order to make the simulation more representatives, the reasonable variations of LST are varied in a wide range according to the atmospheric temperature T_{a_1st} in the first boundary layer of the atmospheric profiles used. That is, LST varies from T_{a_1st}-5K to T_{a_1st}+15K in steps of 5 K for $T_{a_1st} \geqslant$290K, and from T_{a_1st} -5K to T_{a_1st} +5K in steps of 5 K for $T_{a_1st} <$290K. Moreover, considering the most land covers, the averaged emissivity ε varies from 0.90 to 1.0 with a step of 0.02, and the emissivity difference $\Delta\varepsilon$ varies from -0.025 to 0.015 with a step of 0.005 were used in our simulation [Wan and Dozier, 1996].

Then for a given LST, in combination with the atmospheric parameters (τ_i, $R^{\uparrow}_{atm\_i}$, $R^{\downarrow}_{atm\_i}$), LST (T_s) and LSE (ε_i), the channel brightness temperature T_i at the TOA can be simulated according to

Eq. (2.1) with the inverse of Planck's law. At this stage, the T_s is directly related to the TOA measured brightness temperatures T_i and T_j. The coefficients $a_0 - a_6$ in Eq. (2.3) can be obtained through statistical regression method. In total, for the TIGR2002 database and the six standard MODTRAN 4 atmospheres, 261738 different situations were obtained for each VZA.

2.2 Results and analysis

2.2.1 GSW algorithm coefficients

In order to determine the coefficients a_1-a_6 in Eq. (2.3), Wan and Dozier [1996] divided the averaged emissivity, atmospheric WVC and atmospheric surface temperature into several tractable sub-ranges for improving the fitting accuracy. Taking into account the fact that the S-VISSR sensor onboard FY-2C has no atmospheric sounding channels, the atmospheric surface temperature is not simultaneously available, and thus it will be substituted in this work for the determination of the coefficients in Eq. (2.3) by the approximate Land Surface Temperature (LST) as proposed by Jiang and Li [2008].

For different values of the numerical experiments, in order to improve the accuracy of the retrieval LST, for each VZA as done in Wan and Dozier [1996] and in Jiang and Li [2008], the averaged emissivity was divided into two groups: one varies from 0.90 to 0.96 and the other ranges from 0.94 to 1.0. The WVC was divided into six sub-ranges with an overlap of 0.5 g/cm^2: [0, 1.5], [1.0, 2.5], [2.0, 3.5], [3.0, 4.5], [4.0, 5.5], and [5.0, 6.5] g/cm^2. The LST, Ts, was divided into five sub-ranges with an overlap of 5 K: $T_s \le 280$ K, $275 \le T_s \le 295$ K, $290 \le T_s \le 310$ K, $305 \le T_s \le 325$ K, $T_s \ge 320$ K. Then, the coefficients $a_0 - a_6$ in Eq.(2.3) can be obtained through statistical regressions method for each VZA and each sub-range.

As an example, Fig.2-2 displays the coefficients of the GSW algorithm as functions of the secant VZA for the sub-range with WVC from 1.0 g/cm^2 to 2.5 g/cm^2, and LST varying from 290 K to 310 K for the two emissivity groups. As shown in this Figure, the coefficients $a_0 - a_6$ for other VZAs can be linearly interpolated in function of the secant VZA. Similar results are obtained for the other sub-ranges.

2.2.2 Estimation of LST

Fig.2-3 shows, respectively, the histogram of the difference between the actual T_s and the T_s estimated using GSW algorithm with the coefficients corresponding to the sub-range $WVC \in [1.0, 2.5]$, and $T_s \in [290K, 310K]$ for two different emissivity groups and VZA=0°. The Root Mean Square Errors (RMSEs) between the actual and estimated T_s is 0.37 K for the emissivity group $\varepsilon \in [0.94, 1.0]$, and 0.48 K for the other emissivity group $\varepsilon \in [0.90, 0.96]$. Similar results were obtained for the other VZAs.

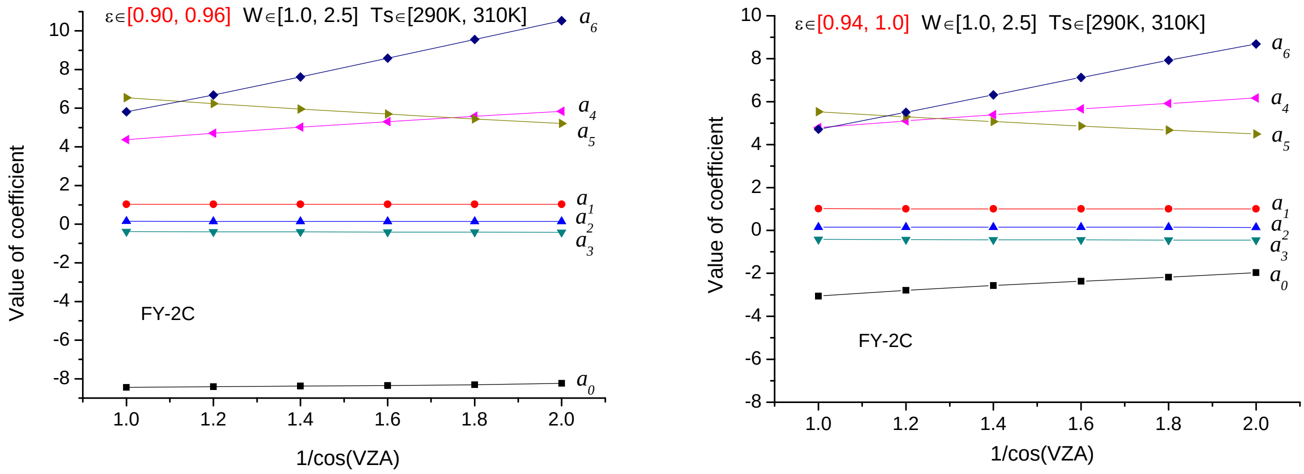

(a) (b)

Fig.2-2 Coefficients of the generalized split-window algorithm for the sub-range with LST varying from 290 K to 310 K, and WVC from 1.0 g/cm^2 to 2.5 g/cm^2.(a) for $\varepsilon \in [0.90, 0.96]$ and (b) for $\varepsilon \in [0.94, 1.0]$

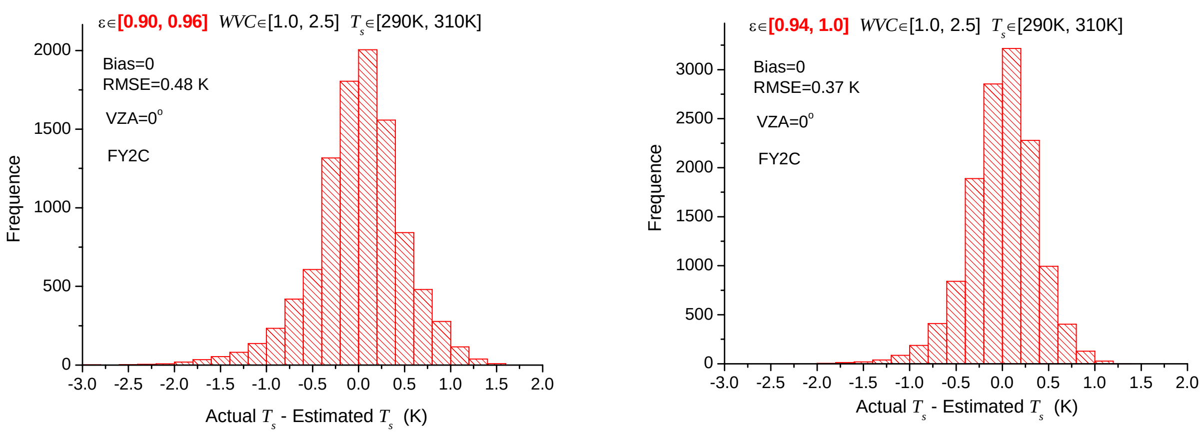

(a) (b)

Fig.2-3 Histogram of the difference between the actual and estimated T_s for the sub-range with LST varying from 290 K to 310 K, and WVC from 1.0 g/cm^2 to 2.5 g/cm^2. (a) for $\varepsilon \in [0.90, 0.96]$ and (b) for $\varepsilon \in [0.94, 1.0]$

In addition, Fig.2-4 gives the RMSEs between the actual and estimated T_s as functions of the secant VZA for the two emissivity groups with different sub-ranges. Taking into account that, in reality, the lower LST usually accompanied with much less WVC, as shown in Fig.2-1, Therefore, for the LST less than 280 K, the maximum WVC is 2.5 g/cm^2, while for the LST between 275 K and 295 K, the maximum WVC is 5.5 g/cm^2.

From Fig.2-4, one can see that the RMSEs increase with the increase of the VZA. The RMSEs are less than 1 K for all sub-ranges with the VZA less than 30°, or for all sub-ranges with the VZA less than 60° and the WVC less than 3.5 g/cm^2. The RMSEs increase dramatically with the increase of the VZA when the WVC larger than 3.0 g/cm^2, with the maximum RMSE of 2.7 K for the sub-range $\varepsilon \in [0.94, 1.0]$, $WVC \in [5.0, 6.5]$, and $T_s \in [305K, 325K]$, for VZA=60°.

It should be pointed out here that, in practice, the LST is estimated in two steps for actual satellite data. Firstly, approximate LSTs are estimated using Eq. (2.3) with the coefficients derived for the whole range of LST providing that the sub-ranges of emissivity and WVC are known, and then more accurate LSTs are estimated once again using Eq. (2.3), but with the coefficients $a_0 - a_6$ corresponding to the sub-range of LST which is determined according to the approximate LST obtained in the first step. Fig.2-4 also shows the RMSEs between the actual T_s and the T_s estimated with the coefficients obtained for the whole range of LST.

Keeping in mind that the GSW algorithm also requires LSE and WVC as model input, the following section will present the determination of these two parameters.

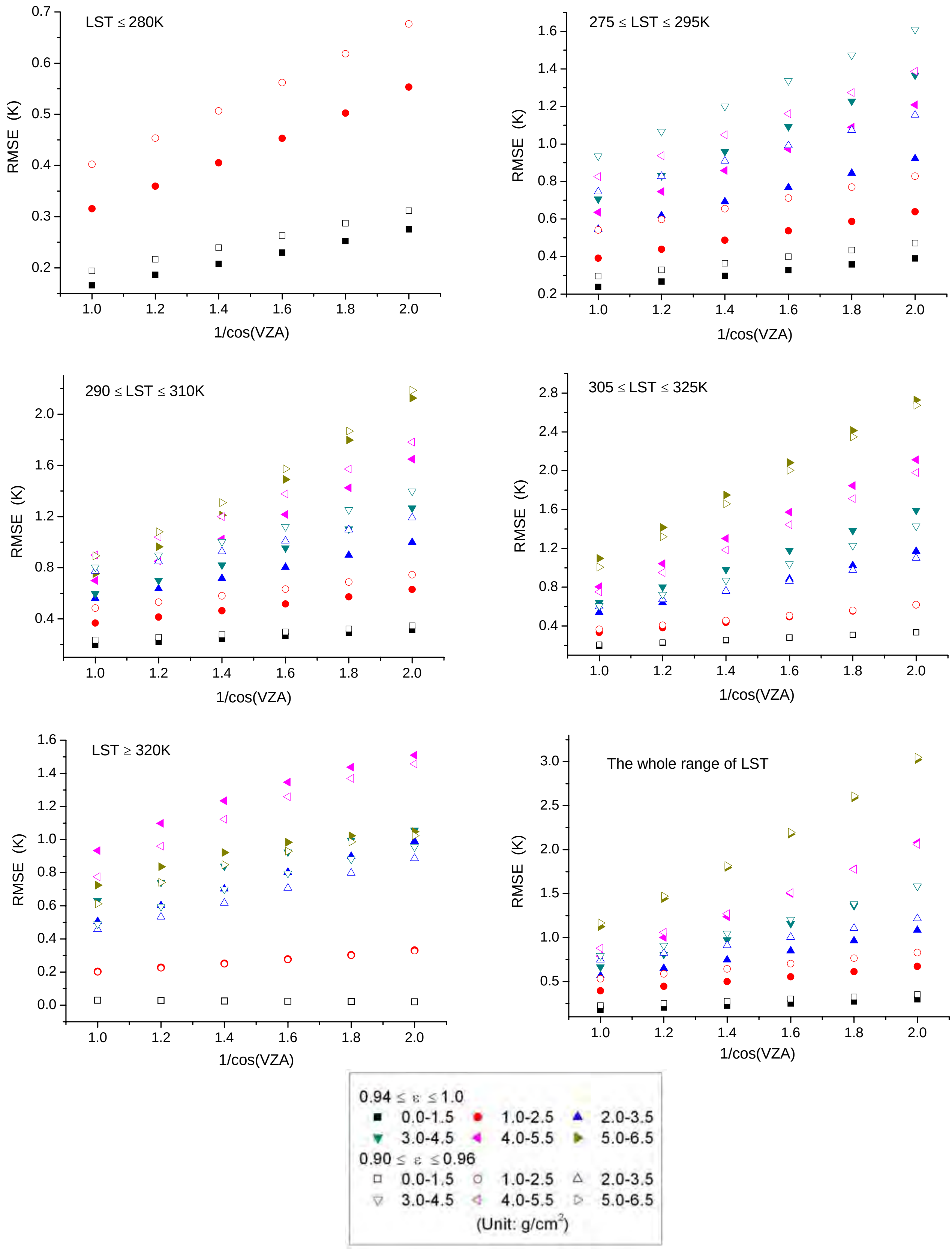

Fig.2-4 RMSEs between the actual and estimated T_s as functions of the secant VZA for different subranges in two different emissivity groups.

2.2.3 Determination of the LSEs

The LSEs in channels IR1 and IR2 of S-VISSR can be estimated from the LSEs in channels 31 (11 μm) and 32 (12 μm) of MODIS provided by the MODIS LST product MOD11B1 at 5 km resolution. To determine the emissivity relationship between S-VISSR channels and MODIS 31 and 32 channels, two spectral databases, one from the University of California Santa Barbara (UCSB) (http://www.icess.ucsb.edu/modis/EMIS/html/em.html) and the other from the Johns Hopkins University (JHU) (http://speclib.jpl.nasa.gov/), are used. The emissivities in the two split-window channels of MODIS (ε_{31} and ε_{32}) and S-VISSR (ε_{IR1} and ε_{IR2}) were calculated by the integrals of the spectral emissivity with the channel response functions over the spectral range of the channels. The channel response functions of the two split-window channels for MODIS and FY-2C are displayed respectively in Fig.2-5.

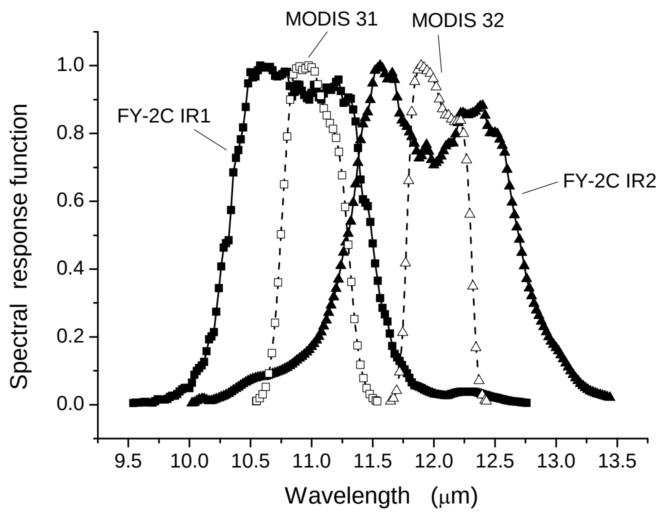

Fig.2-5 S-VISSR and MODIS split-window spectral response functions.

A statistical relationship between MODIS channels and S-VISSR channels was established by a linear regression analysis. As a result, the emissivities in S-VISSR channels IR1 and IR2 are, respectively, related to the emissivities in MODIS channels 31 and 32 by Eqs. (2.4) and (2.5).

$$\varepsilon_{IR1} = -0.0611 + 1.0614\varepsilon_{31} \tag{2.4}$$

$$\varepsilon_{IR2} = -0.0210 + 1.0199\varepsilon_{32} \tag{2.5}$$

Fig.2-6 shows the emissivities and linear regression results. Only the emissivities of soil, vegetation, water, and snow/ice in JHU and UCSB databases were included in this work. Some few deviated points in this Figure are due to the fact that the spectral ranges of S-VISSR channels IR1 and IR2 are broader than those of MODIS channels 31 and 32 as shown in Fig.2-5. However, as shown in Fig.2-6, the results of the linear regression are good with the RMSEs within 0.002, which indicates that the emissivities in S-VISSR channels IR1 and IR2 can be directly derived from those in MODIS channels 31 and 32, respectively.

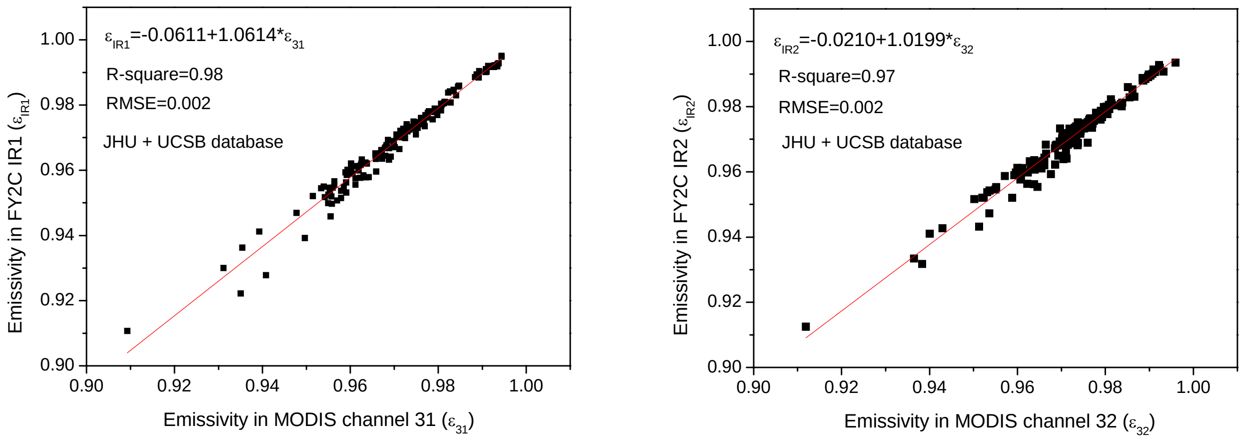

Fig.2-6 Linear fitting relationship of the emissivities between the S-VISSR channels IR1 and IR2 and the MODIS channels 31 and 32, respectively.

Alternatively, the emissivities of the S-VISSR IR1 and IR2 channels can be estimated either with the land surface classification as did by Sun and Pinker [2003] or using the method developed by Jiang et al. [2006] which combined mid-infrared and thermal infrared data of SEVIRI to retrieve LSE.

2.2.4 Determination of the atmospheric WVC

The MODIS total precipitable water product MOD05 provides the atmospheric column water vapor amounts, which can be used as the model input when the scanning time of the sensors MODIS and S-VISSR is closed each other. However, MODIS provides the instantaneous WVC only four times per day, which can not meet the temporal resolutions (an hour) of S-VISSR onboard FY-2C. Since the atmospheric WVC changes with time, the method developed by Li et al. [2003] can be used to determine the WVC from S-VISSR IR1 and IR2 data.

According to Li et al. [2003], the atmospheric WVC can be derived by the use of the transmittance ratio of split-window channels,

$$WVC = c_1 + c_2 \times \frac{\tau_j}{\tau_i} \tag{2.6}$$

with

$$\frac{\tau_j}{\tau_i} = \frac{\varepsilon_i}{\varepsilon_j} R_{ji} \tag{2.7}$$

and

$$R_{ji} = \frac{\sum_{k=1}^{N} (T_{i,k} - \overline{T}_i)(T_{j,k} - \overline{T}_j)}{\sum_{k=1}^{N} (T_{i,k} - \overline{T}_i)^2} \tag{2.8}$$

where c_1 and c_2 are unknown coefficients, τ_i and τ_j are the atmospheric transmittances in the split-window channels i and j, the subscript k denotes pixel k, and the $\overline{T_i}$ and $\overline{T_j}$ are the TOA mean (or the median) channel brightness temperatures of the N neighboring pixels considered for channels i and j, respectively.

On the basis of the numerical results obtained in Section 2.1.2, coefficients c_1 and c_2 can be respectively derived as functions of secant VZA as

$$c_1 = 28.104 - 14.996/\cos(\theta) + 3.211/\cos^2(\theta) \tag{2.9}$$

$$c_2 = -28.056 + 14.954/\cos(\theta) - 3.026/\cos^2(\theta) \tag{2.10}$$

where θ is VZA.

Fig.2-7 shows the curve fits of the coefficients c_1, c_2 as functions of secant VZA. As noted, the fitting results are quit well with both R-squares equal to 0.999. In addition, with the actual WVC and the transmittance ratio of split-window channels IR1 and IR2 obtained in Section 2.1.2, the RMSE between the actual WVC and the WVC estimated using Eqs. (2.6), (2.9) and (2.10) is 0.17 g/cm^2, which indicates that the fitting results are good.

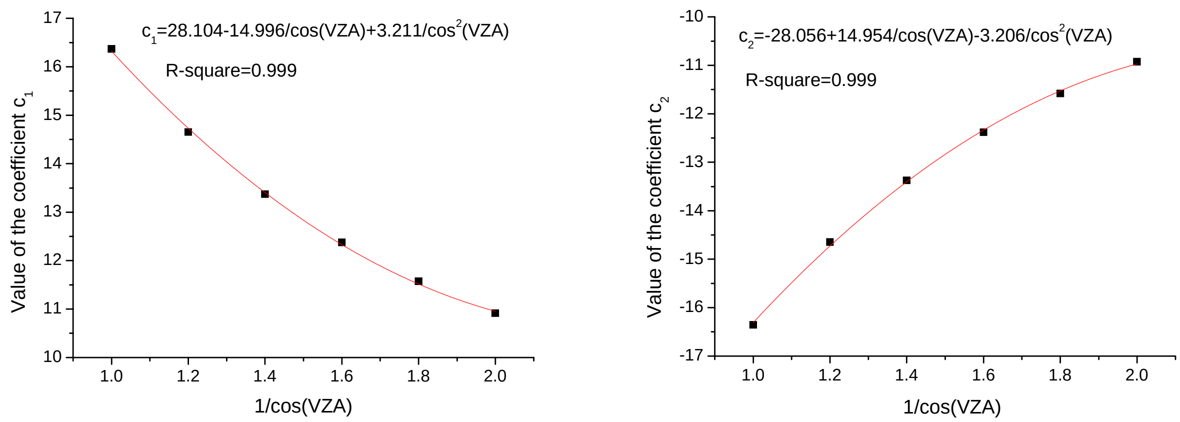

Fig.2-7 Curve fits of the coefficients $c_1 - c_2$ in Eq. (2.6) as functions of the VZA

2.2.5 Sensitivity analysis

As Wan and Dozier [Wan and Dozier, 1996] indicated that the errors of LST estimated by the GSW algorithm come mainly from the uncertainties of LSEs, atmospheric properties and the instrument noises. These three uncertainties of error are taken into account in this investigation.

2.2.5.1 Sensitivity analysis to instrumental noises (NEΔT)

In order to see how significant the effect of the instrumental NEΔT on the retrieval of LST, a Gaussian random distribution error of 0.1 K, 0.2 K and 0.5 K are, respectively added to the TOA brightness temperatures T_i and T_j in Eq. (2.3). Then we estimate the LST using GSW algorithm with the noised TOA brightness temperatures. As an example, compared the actual LST with the estimated LST for the sub-range: $\varepsilon \in [0.94,1.0]$, $WVC \in [1.0,2.5]$, and $T_s \in [290K,310K]$, the RMSE is 0.38 K for NEΔT=0.1 K, 0.43 K for NEΔT=0.2 K, and 0.67 K for NEΔT=0.5 K. Compared the RMSE of 0.37 K for no instrumental noise, the accuracy of retrieval LST can be affected by 3% for NEΔT=0.1 K, by 16% for NEΔT=0.2 K, and by 81% for NEΔT=0.5 K.

2.2.5.2 Sensitivity analysis to LSEs

According to the Eq. (2.3), the sensitivity of the uncertainties in LSEs is mainly dependent on the terms $(1-\varepsilon)/\varepsilon$ and $\Delta\varepsilon/(\varepsilon^2)$, which can be written as

$$\alpha = a_2 \frac{T_i + T_j}{2} + a_5 \frac{T_i - T_j}{2} \tag{2.11}$$

$$\beta = a_3 \frac{T_i + T_j}{2} + a_6 \frac{T_i - T_j}{2} \tag{2.12}$$

Two cases are considered in this investigation. One is the extremely dry atmospheric condition ($WVC \in [0.0,1.5]$) and the other is the extremely wet atmospheric condition ($WVC \in [5.0,6.5]$). With the regression coefficients and the T_i and T_j simulated in Section 2.1.2, using Eqs. (2.11) and (2.12) we can obtain the variations of α and β. Table 2-2 lists the variations of α and β for the sub-range: $\varepsilon \in [0.94,1.0]$, $T_s \in [290K,310K]$, $WVC \in [0.0,1.5]$ and the sub-range $\varepsilon \in [0.94,1.0]$, $T_s \in [290K,310K]$, $WVC \in [5.0,6.5]$, for VZA=0°, respectively.

Table 2-2. Statistics of the errors due to the uncertainties in LSEs for the sub-range $\varepsilon \in [0.94,1.0]$, $T_s \in [290K,310K]$, $WVC \in [0.0,1.5]$ and the sub-range $\varepsilon \in [0.94,1.0]$, $T_s \in [290K,310K]$, $WVC \in [5.0,6.5]$, for VZA=0°.

CONDITIONS	$\varepsilon \in [0.94,1.0]$, $T_s \in [290K,310K]$, VZA=0°			
Water vapor content (g/cm^2)	$WVC \in [0.0,1.5]$		$WVC \in [5.0,6.5]$	
Variable	α	β	α	β
Range of Values (K)	[44.80,61.23]	[-135.71,-121.05]	[11.57, 34.42]	[-70.13,-19.48]
Mean (K)	52.39	-127.60	23.29	-45.56
Standard deviation (K)	3.10	3.06	4.22	9.32

From table 2-2 one can see that the values of α and β in extremely dry atmospheric condition ($WVC \in [0.0,1.5]$) are nearly two times as large as those of α and β in extremely wet atmospheric condition, ($WVC \in [5.0,6.5]$), respectively. This means that the sensitivity of $(1-\varepsilon)/\varepsilon$ and $\Delta\varepsilon/(\varepsilon^2)$ to LST for wet atmospheric condition is decreased two times as that for dry atmospheric condition.

From Eq. (2.3), the LST error δLST due to the uncertainty in $(1-\varepsilon)/\varepsilon$ and $\Delta\varepsilon/(\varepsilon^2)$ can be estimated by,

$$\delta LST = \sqrt{\alpha^2 \delta(\frac{1-\varepsilon}{\varepsilon})^2 + \beta^2 \delta(\frac{\Delta\varepsilon}{\varepsilon^2})^2} \tag{2.13}$$

Assuming that the uncertainties of $(1-\varepsilon)/\varepsilon$ and $\Delta\varepsilon/(\varepsilon^2)$ are around 1%, the LST error is [1.3K, 1.5K] with the mean of 1.4 K for the dry atmosphere and [0.2K, 0.8K] with the mean of 0.5 K for the wet atmosphere.

2.2.5.3 Sensitivity analysis to the atmospheric WVC

It is well known that the WVC in the atmosphere is not easily determined from satellite data. In order to see how significant the effect of the uncertainty of the WVC on the retrieval of LST in GSW algorithm, the wrong sub-range selection of the WVC is investigated in our work. As mentioned above in Section 2.2.1, the WVC was divided into six sub-ranges with an overlap of 0.5 g/cm^2. The overlap WVC could be fallen into two adjacent sub-ranges. That is, it is included by two sub-ranges and corresponded to two pairs of coefficients $a_0 - a_6$. We aim to analyze the effect of the overlap WVC on the retrieval of LST.

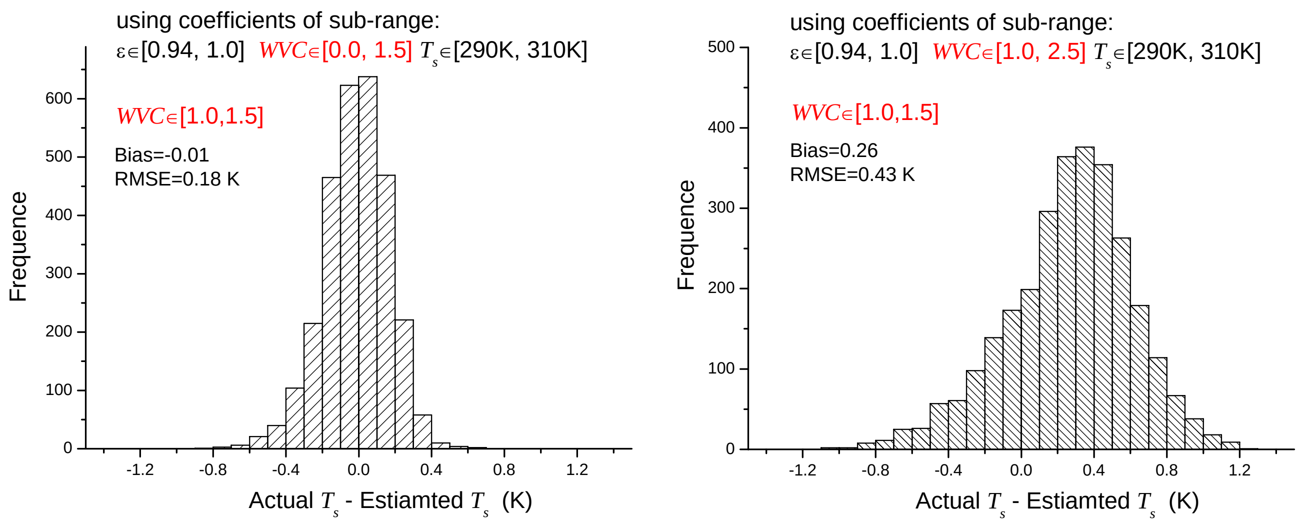

Fig.2-8 Histogram of the difference between the actual and estimated T_s for the overlap water vapor content $WVC \in [1.0, 1.5]$ using the coefficients of different sub-ranges.

Fig.2-8 gives an example of the uncertainty of the WVC. From Fig.2-8 one can see that the overlap water vapor content $WVC \in [1.0, 1.5]$ falling into two sub-ranges $WVC \in [0.0, 1.5]$ and $WVC \in [1.0, 2.5]$. When we estimate the LST with the water vapor content $WVC \in [1.0, 1.5]$ using the coefficients corresponding to the sub-range $\varepsilon \in [0.94, 1.0]$, $WVC \in [0.0, 1.5]$, and

$T_s \in [290K, 310K]$, the RMSE between the actual and the estimated T_s is 0.18 K, while using the coefficients corresponding to the sub-range $\varepsilon \in [0.94, 1.0]$, $WVC \in [1.0, 2.5]$, and $T_s \in [290K, 310K]$, the RMSE is 0.43 K.

2.2.6 Intercomparison of different formulations of the split-window algorithms

It is well known that the LST retrieval from satellite observations has been ongoing for several decades. Many different formulations of the split-window algorithms have been proposed. They are somewhat similar in formulation and several of them are directly inspired from Becker and Li's [Becker and Li, 1990] formulation. In order to perform the intercomparison with the recently proposed split-window algorithms, different formulations were used to estimate the LST with the same simulated FY-2C data in this work. Those formulations are listed in table 2-3:

Table 2-3. Different formulations of split-window algorithms in literatures.

AUTHORS	FORMULATIONS
Price, 1984	$T_s = a_0 + a_1 T_i + a_2(T_i - T_j) + a_3(T_i - T_j)(1-\varepsilon) + a_4 T_j \Delta\varepsilon^*$
Prata and Platt, 1991	$T_s = a_0 + a_1 \frac{T_i}{\varepsilon} + a_2 \frac{T_j}{\varepsilon} + a_3 \frac{1-\varepsilon^*}{\varepsilon}$
Vidal, 1991	$T_s = a_0 + a_1 T_i + a_2(T_i - T_j) + a_3 \frac{1-\varepsilon}{\varepsilon} + a_4 \frac{\Delta\varepsilon}{\varepsilon}$
Ulivieri et al., 1992	$T_s = a_0 + a_1 T_i + a_2(T_i - T_j) + a_3(1-\varepsilon) + a_4 \Delta\varepsilon$
Sobrino et al., 1993	$T_s = a_0 + a_1 T_i + a_2(T_i - T_j) + a_3(T_i - T_j)^2 + a_4(1-\varepsilon) + a_5 \Delta\varepsilon$
Sobrino et al., 1994	$T_s = a_0 + a_1 T_i + a_2(T_i - T_j) + a_3 \varepsilon + a_4 \frac{\Delta\varepsilon}{\varepsilon}$
Coll and Caselles, 1997	$T_s = T_i + a_0 + a_1(T_i - T_j) + a_2(T_i - T_j)^2 + a_3(1-\varepsilon) + a_4 \Delta\varepsilon$

* $\varepsilon = (\varepsilon_i + \varepsilon_j)/2$ and $\Delta\varepsilon = \varepsilon_i - \varepsilon_j$

In addition, Becker and Li [1995] further modified their split-window algorithm [Becker and Li, 1990] by adding atmospheric water vapor correction as

$$T_s = A_0 + P \frac{T_i + T_j}{2} + M \frac{T_i - T_j}{2} \tag{2.14}$$

with $A_0 = a_0 + a_1 w$; $P = a_2 + (a_3 + a_4 w \cos(\theta))(1-\varepsilon) - (a_5 + a_6 w)\Delta\varepsilon$;

$$M = a_7 + a_8 w + (a_9 + a_{10} w)(1-\varepsilon) - (a_{11} + a_{12} w)\Delta\varepsilon$$

where $\varepsilon = (\varepsilon_i + \varepsilon_j)/2$ and $\Delta\varepsilon = \varepsilon_i - \varepsilon_j$, w is the total precipitable water amount, and θ is the Viewing Zenith Angle (VZA).

In order to make the intercomparsion more reasonable, the coefficients from the above equations have been recalculated using the same simulated FY-2C data within the same sub-ranges in Section 2.2.1. As an example, table 2-4 depicts the RMSEs between the actual and the estimated T_s versus the secant VZA for the sub-range: $\varepsilon \in [0.94, 1.0]$, $WVC \in [1.0, 2.5]$, and $T_s \in [290K, 310K]$. From table2-4, one can see that the RMSEs increase with the increase of the VZA for all algorithms. In addition, except for the algorithms proposed by Price [1984], and Prata and Platt [1991], the T_s estimated using the other algorithms are comparable, which indicates that the split-window algorithm can be successfully applied to the LST retrievals from FY-2C data.

Table 2-4. RMSEs between the actual T_s and the T_s estimated using different formulations of the split-window algorithms for the sub-range $\varepsilon \in [0.94, 1.0]$, $WVC \in [1.0, 2.5]$, and $T_s \in [290K, 310K]$.

	VZA (^{o})	AUTHORS								
		GSW	Price84	Prata91	Vidal91	Ulivieri92	Sobrino93	Sobrino94	Coll97	BL95
RMSE (K)	0	0.37	0.73	1.15	0.38	0.38	0.37	0.38	0.38	0.22
	33.56	0.41	0.74	1.26	0.43	0.42	0.42	0.42	0.43	0.25
	44.42	0.46	0.74	1.35	0.48	0.47	0.47	0.47	0.47	0.28
	51.32	0.52	0.75	1.43	0.53	0.53	0.51	0.53	0.52	0.32
	56.25	0.57	0.77	1.49	0.58	0.58	0.57	0.58	0.57	0.36
	60	0.63	0.80	1.54	0.64	0.64	0.62	0.64	0.62	0.41

2.3 Application to actual FY-2C satellite data

The objective of the present work is to estimate the LST from Chinese first operational geostationary meteorological satellite FengYun-2C (FY-2C) data for cloud-free skies. Fig.2-9 gives an example of the retrieval LST around Beijing in China during FY-2C satellite scanning on May 15, 2006 at 11:00 local time. The model inputs are the TOA brightness temperatures, VZA, LSEs, and WVC. The TOA brightness temperatures and VZA are directly extracted from the FY-2C satellite data. The LSEs are derived from the emissivities in MODIS channels 31 and 32 provided by MODIS/Terra LST product MOD11B1, and the WVC are obtained from MODIS total precipitable water product MOD05. Symbols A, B, and C located in red, green and baby blue colored areas in Fig.2-9 represent bare soil, cultivated surface and sea surface, respectively.

In addition, table 2-5 lists the values of the VZA, WVC, LSE, TOA brightness temperature, and resultant T_s for one representative pixel in each red, green, and baby blue colored areas in Fig.2-9.

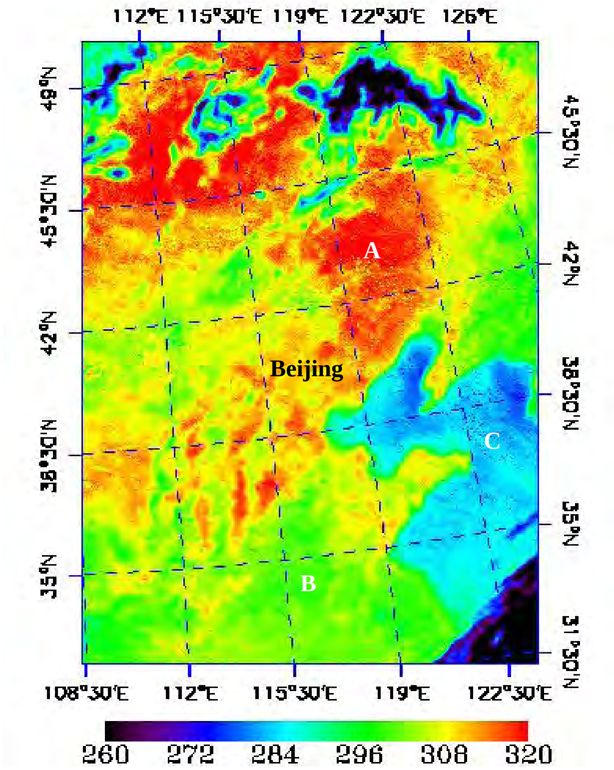

Fig.2-9 Map of the LST estimated from FY-2C satellite data at 11:00 local time on May 15, 2006.

Table 2-5. Description of symbols A, B and C in Fig.2-9

	A (RED)	B (GREEN)	C (BABY BLUE)
Longitude (°)	120.06 E	116.15 E	122.75 E
Latitude (°)	43.70 N	33.84 N	38.47 N
VZA (°)	53.44	41.96	49.14
WVC (g/cm^2)	0.868	1.465	1.217
ε_{IR1}	0.944	0.962	0.986
ε_{IR2}	0.946	0.966	0.99
T_{IR1} (K)	309.42	295.24	281.95
T_{IR2} (K)	307.32	294.58	282.20
T_s (K)	318.35	299.74	286.47

It should be pointed out here that the LST estimated from the FY-2C satellite data has not been validated with in situ measurements since there are no in situ measurements available. In addition, due to the extreme difficulty or impossibility to get the LST at ground level representative at 5km*5km, we will try to cross validate LST derived from FY-2C data in the future with the well validated LST product provided by MODIS data.

2.4 Conclusions

In this chapter, we have addressed the retrieval of the Land Surface Temperature (LST) from the Chinese first operational geostationary meteorological satellite FengYun-2C (FY-2C) data in two thermal infrared channels IR1 (10.3-11.3 μm) and IR2 (11.5-12.5 μm), using the Generalized Split-Window (GSW) algorithm proposed by Wan and Dozier [1996].

Taking into account the fact that the S-VISSR sensor onboard FY-2C has no atmospheric sounding channels, the coefficients in the GSW algorithm were derived by dividing the ranges of the mean emissivity, the atmospheric Water Vapor Content (WVC), and the LST into tractable sub-ranges, and were recalculated using a statistical regression method from the numerical values simulated with an accurate atmospheric radiative transfer model MODTRAN 4 over a wide range of the atmospheric and surface conditions. The simulation analysis showed that the LST could be estimated by the GSW algorithm with the Root Mean Square Error (RMSE) less than 1 K for the sub-ranges with the Viewing Zenith Angle (VZA) less than 30° or for the sub-ranges with VZA less than 60° and the atmospheric WVC less than 3.5 g/cm^2 provided that the Land Surface Emissivities (LSEs) are known.

As the GSW algorithm requires WVC and LSE as model input, the MODIS total precipitable water product MOD05 providing the atmospheric column water vapor amounts, was used to obtain the WVC when the scanning time of the sensors MODIS and S-VISSR is closed each other. As for the other scanning times of S-VISSR, the atmospheric WVC can be determined using the method developed by Li et al. [2003]. As for LSE, the MODIS/Terra LST product MOD11B1 providing the LSEs with 5 km resolution for the thermal infrared channels 31 and 32, was used to derive the LSEs in S-VISSR channels IR1 and IR2, respectively.

In addition, the sensitivity and error analyses in term of the uncertainty of the LSE and WVC as well as the instrumental noise were also performed in this work. The results show that the accuracy of retrieval LST can be affected by 3% for NEΔT=0.1 K, by 16% for NEΔT=0.2 K, and by 81% for NEΔT=0.5 K for the sub-range $\varepsilon \in [0.94, 1.0]$, $WVC \in [1.0, 2.5]$, and $T_s \in [290K, 310K]$; given the uncertainties of $(1-\varepsilon)/\varepsilon$ and $\Delta\varepsilon/(\varepsilon^2)$ around 1%, the LST error is [1.3K, 1.5K] with the mean of 1.4 K for the dry atmosphere and [0.2K, 0.8K] with the mean of 0.5 K for the wet atmosphere; and the effect of the uncertainty of the WVC on the retrieval LST could be around 0.3 K.

Moreover, in order to compare the different formulations of the split-window algorithm, several split-window algorithms were used to estimate the LST with the same simulated FY-2C data. The result of the intercomparsion showed that most of the algorithms give comparable results, which indicates that the split-window algorithm can be successfully applied to the LST retrievals from FY-2C data.

Chapter 3

Estimation of Land Surface Directional Emissivity in Mid-InfraRed Channel around 4.0μm from MODIS Data

Up to now many Bidirectional Reflectance Distribution Functions (BRDFs) have been developed to describe the bidirectional reflectance in visible and near infrared channels as a function of both illumination and view geometries [Nilson and Kuusk, 1989; Roujean et al., 1992; Wanner et al., 1995; Lucht and Roujean, 2000; Pokrovsky and Roujean, 2002; Lucht, 1998]. The semi-empirical kernel-driven models [Roujean et al., 1992; Wanner et al., 1995; Lucht and Roujean, 2000; Pokrovsky and Roujean, 2002] have been proven successfully in application to AVHRR, Polarization and Directionality of Earth Reflectance (POLDER), MODIS, Multi-angle Imaging Spectra-Radiometer (MISR), laboratory, and field-measured multi-angular reflectance data and have been shown to fit observed BRDF data well [Roujean et al., 1992; Wanner et al., 1995; Lucht, 1998; Lucht and Roujean, 2000; Pokrovsky and Roujean, 2002]. Only a few works focused on the BRDF modeling in the mid-infrared region (MIR), but all of them have aimed to estimate the emissivity in MIR from the bidirectional reflectance derived from AVHRR and MSG/SEVIRI data [Jiang et al., 2006; Li et al., 2000; Petitcolin et al., 2002].

This chapter will be devoted to estimate the land surface directional emissivity in MIR channel from the bidirectional reflectance derived from MODIS data in two adjacent MIR channels. Section 3.1 recalls the methodology to retrieve directional emissivity in MIR channel. Section 3.2 describes the study area, MODIS data and data processing. Section 3.3 presents some preliminary results and cross-validation with the MODIS land surface temperature/emissivity product MYD11B1 data. Finally, conclusions are given in section 3.4.

3.1 Determination of directional emissivity in MIR channel from MODIS data

3.1.1 Retrieval of the bidirectional reflectivity in MIR channel from MODIS data

The instrument MODIS onboard Terra and Aqua satellites has two adjacent MIR channels 22 and 23 centered at 3.97 *um* and 4.06 *um* respectively. Based on the difference in the solar reflection in these two channels, and assuming that the surface bidirectional reflectivities are equal in channels 22 and 23, and that the ground brightness temperatures in these two adjacent channels are the same if the contribution of the direct solar radiation is not considered, Tang and Li [2008a] developed a method to retrieve the bidirectional reflectivity (ρ_b) in the MIR channel from MODIS channels 22 and 23 with

$$\rho_b = \frac{B(T_{g\_22}) - B(T_g^0)}{R_{22}^s} \tag{3.1}$$

where B is the Planck function, T_{g_22} is the daytime ground brightness temperature of MODIS channel 22, R_{22}^s is the solar irradiance at ground level in MODIS channel 22, T_g^0 is the MIR ground brightness temperature without the contribution of the solar direct beam and can be estimated from the ground brightness temperatures T_{g_22} and T_{g_23} in the channels 22 and 23 using

$$T_g^0 = T_{g\_22} + a_1 + a_2\left(T_{g\_22} - T_{g\_23}\right) + a_3\left(T_{g\_22} - T_{g\_23}\right)^2 \tag{3.2}$$

in which the coefficients $a_1 - a_3$ are dependent only on the Solar Zenith Angle (SZA). More details concerning both the development and the application of this method with MODIS data can be found in Tang and Li [2008a].

3.1.2 Estimation of the directional emissivity in MIR channel from bidirectional reflectivity

For an opaque medium in thermal equilibrium, the directional emissivity $\varepsilon(\theta)$ is related to the hemispherical directional reflectance $\rho_h(\theta)$ by the Kirchhoff's law as:

$$\varepsilon(\theta) = 1 - \rho_h(\theta) \tag{3.3}$$

with

$$\rho_h(\theta) = \int_0^{2\pi}\int_0^{\pi/2} \rho_b(\theta, \theta_i, \varphi)\sin(\theta_i)\cos(\theta_i)d\theta_i d\varphi \tag{3.4}$$

where θ is the viewing zenith angle, θ_i is the incident radiation angle, φ is the relative azimuth angle between the observation and incident directions, and ρ_b is the bidirectional reflectance of land surface in MIR channel retrieved with Eq. (3.1).

Based on the theory that land surface reflectance typically consists of three components: the isotropic scattering, the volumetric scattering and the geometric-optical surface scattering, a kernel-driven BRDF model, the RossThick-LiSparse-R model, was proposed to describe the non-Lambertian reflective behavior of land surface in visible and near-infrared regions [Roujean et al., 1992; Lucht, 1998; Lucht and Roujean, 2000]:

$$\rho_b(\theta, \theta_i, \varphi) = k_{iso} + k_{vol} f_{vol}(\theta, \theta_i, \varphi) + k_{geo} f_{geo}(\theta, \theta_i, \varphi) \tag{3.5}$$

where k_{iso} is the isotropic scattering term, k_{vol} is the coefficient of the Roujean's volumetric kernel f_{vol}, and k_{geo} is the coefficient of the LiSparse-R geometric kernel f_{geo}.

For a plane-parallel dense vegetation canopy with uniform leaf angle distribution, and equal leaf reflectance and transmittance, the Roujean's volumetric kernel [Roujean et al., 1992] is given by

$$f_{vol}(\theta, \theta_i, \varphi) = \frac{4}{3\pi}\frac{1}{\cos\theta + \cos\theta_i}\left[(\frac{\pi}{2} - \xi)\cos\xi + \sin\xi\right] - \frac{1}{3} \tag{3.6}$$

where ξ is the phase angle, related to the conventional angles by

$$\cos\xi = \cos\theta\cos\theta_i + \sin\theta\sin\theta_i\cos\varphi \tag{3.7}$$

Considering the mutual shadowing between different protrusions of vegetation canopy, the reciprocal LiSparse geometric kernel f_{geo} derived by Wanner et al. [1995] and modified by Lucht [1998] is employed

$$f_{geo} = G(\theta, \theta_i, \varphi) - \sec\theta' - \sec\theta_i' + \frac{1}{2}(1 + \cos\xi')\sec\theta'\sec\theta_i' \tag{3.8}$$

where $G(\theta, \theta_i, \varphi)$ is the overlap area between the view and solar shadows and given by

$$G(\theta, \theta_i, \varphi) = \frac{1}{\pi}(t - \sin t\cos t)(\sec\theta' + \sec\theta_i') \tag{3.9}$$

in which

$$\theta' = \tan^{-1}(\frac{b}{r}\tan\theta\ ), \quad \theta_i' = \tan^{-1}(\frac{b}{r}\tan\theta_i)$$

$$\cos\xi' = \cos\theta'\cos\theta_i' + \sin\theta'\sin\theta_i'\cos\varphi$$

$$t = \cos^{-1}\left(\frac{h}{b}\frac{\sqrt{D^2 + (\tan\theta'\tan\theta_i'\sin\varphi)^2}}{\sec\theta' + \sec\theta_i'}\right)$$

with

$$D = \sqrt{\tan^2\theta' + \tan^2\theta_i' - 2\tan\theta'\tan\theta_i'\cos\varphi}$$

h/b and b/r are the dimensionless crown relative height and shape parameters, respectively.

According to Eqs. (3.3), (3.4) and (3.5) and assuming that the BRDF shapes in the MIR spectral region are the same as the ones in visible and near-infrared regions [Jiang and Li, 2008], the directional emissivity in MODIS MIR channel is given by

$$\varepsilon(\theta) = 1 - \pi k_{iso} - k_{vol} If_{vol}(\theta) - k_{geo} If_{geo}(\theta) \tag{3.10}$$

with $If_x(\theta) = \int_0^{2\pi}\int_0^{\pi/2} f_x(\theta,\theta_i,\varphi)\sin(\theta_i)\cos(\theta_i)d\theta_i d\varphi$

in which the subscription *x* represents *vol* or *geo*.

As shown in Eq. (3.10), the integrals of $If_{vol}(\theta)$ and $If_{geo}(\theta)$ over the incident radiation angle θ_i and the relative azimuth angle φ are complicated mathematical expressions and can not be analytically derived. As used in MODIS BRDF/Albedo products, taking h/b=2 and b/r=1, i.e., the spherical crowns are separated from the ground by half their diameter, Jiang and Li [2008] showed numerically that the integrals of the Roujean's volumetric kernel f_{vol} (Eq.(3.6)) and the reciprocal LiSparse geometric kernel f_{geo} (Eq.(3.8)) can be written with a good approximation as

$$If_{vol}(\theta) = -0.0299 + 0.0128\exp(\theta / 21.4382) \tag{3.11}$$

$$If_{geo}(\theta) = -2.0112 - 0.3410\exp\left[-2(\frac{\theta - 90.9545}{68.8171})^2\right] \tag{3.12}$$

It should be noted that if a series of ρ_b with different angular configurations are retrieved from the MODIS data using Eq. (3.1), one can get the parameters k_{iso}, k_{vol} and k_{geo} from Eq. (3.5). Knowing these three parameters, the directional emissivity in MIR channel can be obtained with Eqs. (3.10), (3.11) and (3.12).

3.2 Study area and data processing

A region of Egypt and Israel with latitude from 28.0° N to 32.0° N and longitude from 30.0° E to 36.0° E was chosen in this study. Fig.3-1 shows the land use map of this study area generated from MODIS land cover type 2004 L3 global 1 km product MOD12Q1 (http://edcdaac.usgs.gov/modis/mod12q1v4.asp) and classified by the International Geosphere-Biosphere Programme (IGBP). From this Figure, we can see that the major land cover types in this area are barren or sparsely vegetated, croplands, and open shrubland. Since the classification scheme of IGBP does not include bare soil surface, to discriminate from barren or sparsely vegetated, this surface type will be used in our following work. The reason to choose this region is that a series of cloud-free MODIS data are available over this region from July 12 to July 30 of 2005. Therefore, the three parameters k_{iso}, k_{vol} and k_{geo} in Eq. (3.5) can be determined with the retrieved bidirectional reflectivity ρ_b under the assumption that the land surface remains unchanged during this period.

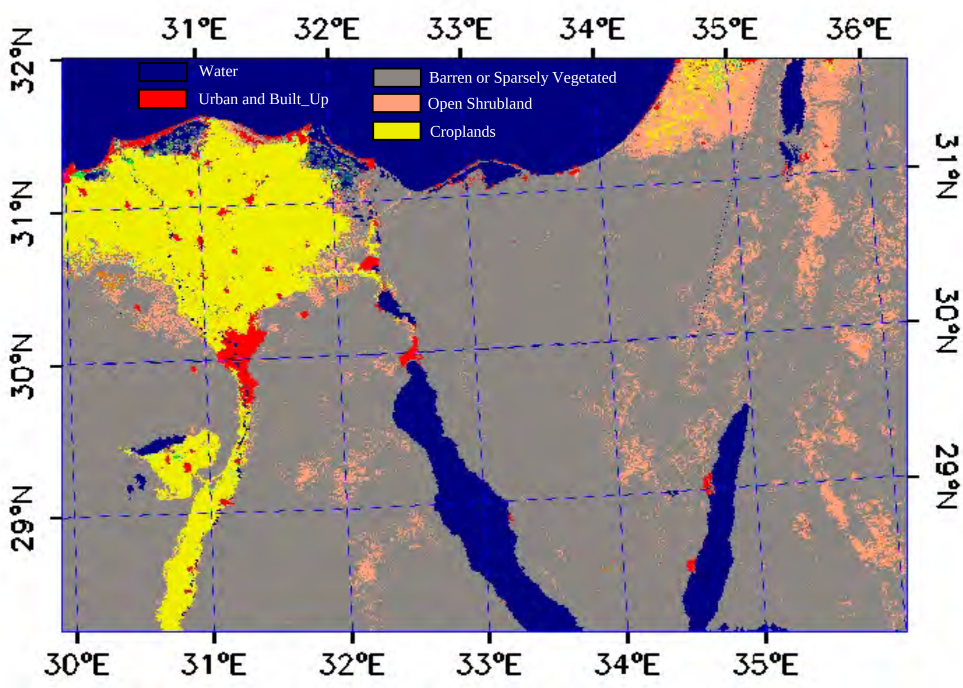

Fig.3-1 Land use map of the study area generated from MODIS land cover type 2004 L3 global 1 km product (MOD12Q1) and classified by IGBP classification scheme.

The MYD021KM, MYD03 and MYD35_L2 product files provided by the National Aeronautics and Space Administration (NASA) Goddard Space Flight Center (GSFC) Level 1 and Atmosphere Archive and Distribution System (LAADS) (http://ladsweb.nas.com.nasa.gov/data/) were used in our work. The MYD021KM data, calibrated Earth View data at 1 km resolution by the MODIS Characterization and Support Team (MCST), are the Top of Atmosphere (TOA) radiances and reflectances. The geolocation dataset, MYD03, provides latitude, longitude, ground elevation, solar zenith and azimuth angles, and satellite zenith and azimuth angles for each 1 km sample. The MYD35_L2 is a cloud mask product which gives a clear-sky confidence level (clear, probably clear, uncertain, cloudy) to each IFOV (Instantaneous Field Of-View). More details about these product files can be found in [Wan, 2008]. Ten days MODIS data with cloud-free conditions at the moment of MODIS overpasses, from July 12 to July 30 of 2005 were selected. Table 3-1 gives the dates and acquisition times of these ten days MODIS data. The European Centre of Median-range Weather Forecast (ECMWF) reanalysis (ERA) operational deterministic model data directly obtained from the French Meteorological Center with latticed resolution of 0.5° in both latitude and longitude [Uppala et al., 2005] were used to perform atmospheric corrections for MODIS MIR data in this work. In addition, taking into account the real atmospheric path length between the surface and the satellite, global DEM data at 30 arc-s (1 km) resolutions (http://edc.usgs.gov/products/elevation/gtopo30/gtopo30.html) were also used.

Table 3-1. Date and acquisition time for ten days MODIS data used in this study

Date (dd/mm/year)	UTC time (hh:mm)	Date (dd/mm/year)	UTC time (hh:mm)
12/07/2005	11:00	23/07/2005	10:40
14/07/2005	10:45	24/07/2005	11:25
15/07/2005	11:30	26/07/2005	11:10
16/07/2005	10:35	28/07/2005	11:00
19/07/2005	11:05	30/07/2005	10:45

Based on the clear-sky confidence level (clear, probably clear, uncertain, cloudy) assigned to each IFOV in MYD35_L2, clear and probably clear pixels were taken as clear, and uncertain and cloudy pixels were taken as cloudy in our study. The cloudy pixels assigned in this study were then firstly screened out in the retrieval of ρ_b. Since the satellite instrument measures only the radiances at the Top of Atmosphere (TOA), the data acquired by MODIS MIR channels 22 and 23 have to be corrected for the atmospheric effects in order to obtain the radiances or brightness temperatures at ground level. These atmospheric corrections were performed using the atmospheric radiative transfer model-MODTRAN 4 with the ECMWF data and DEM data. Selection of ECMWF output data as atmospheric profiles is due to the fact that the MIR channels 22 and 23 are not too sensitive to the change of water vapor content in the atmosphere. More details of atmospheric corrections for MODIS MIR channels can be found in Tang and Li [2008a]. After having performed the atmospheric corrections, the bidirectional reflectances in MODIS MIR channel 22 can be estimated with Eqs. (3.1) and (3.2).

The three parameters k_{iso}, k_{vol} and k_{geo} in Eq. (3.5) for each pixel are then determined by a Levenberg-Marquardt minimization scheme with the retrieved ρ_b and corresponding illumination and view angles extracted from MYD03 data. Finally, the directional emissivities at each view zenith angle for MODIS MIR channel are obtained with Eq. (3.10).

3.3 Results and validations

The objective of the present work is to estimate the directional emissivity from MODIS MIR channels. Fig.3-2 gives an example of the retrieved directional emissivity map for July 24, 2005 at 11:25 UTC time.

As shown in Fig.3-1, points A, B, C, and D marked in Fig.3-2 represent bare soil, open shrubland, barren or sparsely vegetated, and croplands surfaces respectively. For the entire study area, the directional emissivities in MODIS MIR channel 22 vary from 0.6 to 1.0, and they are usually less than 0.80 over the bare areas, while the opposite is observed over the vegetated areas. Fig.3-3 illustrates histograms of the estimated directional emissivities for the four major land covers (bare soil, open shrubland, barren or sparsely vegetated, and croplands surfaces) in the entire study area. As displayed in Fig.3-3, the directional emissivity in MIR channel varies from 0.67 to 0.78 with mean=0.73 and standard deviation (std)=0.021 for the bare soil surfaces, and from 0.83 to 0.94 with mean=0.89 and std=0.019 for the open shrubland, while for barren or sparsely vegetated surfaces the directional emissivity in MIR channel ranges from 0.89 to 0.98 with mean value of 0.94 and std=0.013, and for croplands, the emissivity in MIR channel is the highest and ranges from 0.92 to 0.99 with mean=0.97 and std=0.012.

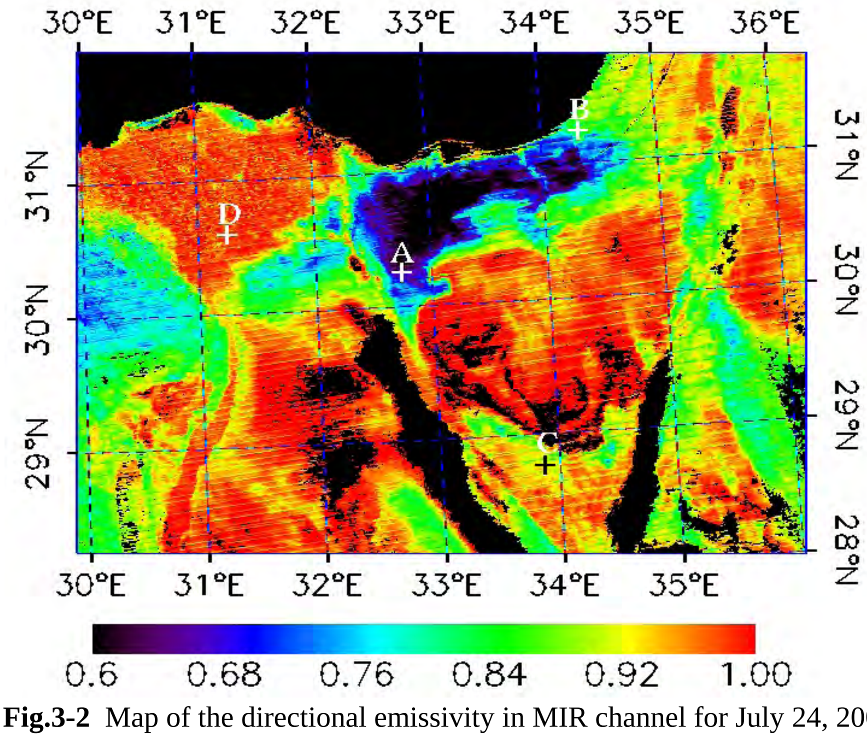

Fig.3-2 Map of the directional emissivity in MIR channel for July 24, 2005.

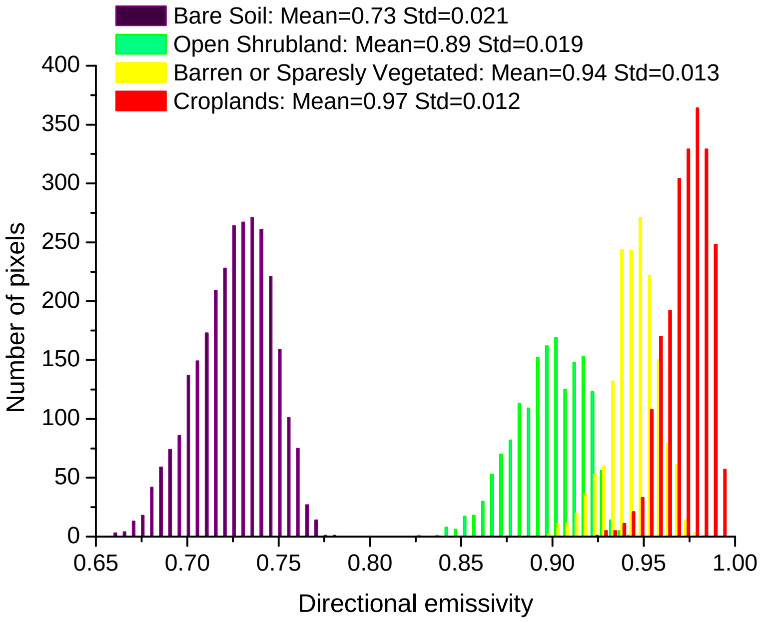

Fig.3-3 Histogram of the directional emissivity in MIR channel estimated from MODIS data for the major land cover types in the study area. Std=standard deviation.

Fig.3-4 displays the sun and satellite zenith and azimuth angles in polar representation at four locations for ten clear days from July 12 to July 30 of 2005 which we used to retrieve the directional emissivity. For these locations, the sun is in the West direction and coincides nearly with the satellite along track direction. The observation directions are almost in the principal plane and lie in the east and west directions according to the instrument scanning directions. It should be pointed out here that although the change of solar zenith angle is very small during this period for a given pixel, the viewing zenith angle of each pixel (location) varies significantly from 0° to 60° from July 12 to July 30. We can, consequently, get the parameters k_{iso}, k_{vol} and k_{geo} using Eq. (3.5) with a series of ρ_b and different angular configurations.

Fig.3-5(a) shows the comparison of the bidirectional reflectance ρ_b estimated directly from MODIS MIR data (Eq.(3.1)) with ρ_{b} modeled using Eq. (3.5) at four locations for the ten clear days. The Root Mean Square Error (RMSE) and Mean Error (ME) are respectively 0.005 and zero. From this Figure, one can notice that the bidirectional reflectances for locations A and B are larger, while for locations C and D, they are relatively smaller. In addition, Fig.3-5(b) gives the histogram of the differences between the retrieved and modeled bidirectional reflectances for the entire study area. From this Figure, one can see that the difference of the retrieved and modeled ρ_b ranges from -0.03 to 0.03 with mean of -0.001 and standard deviation of 0.008.

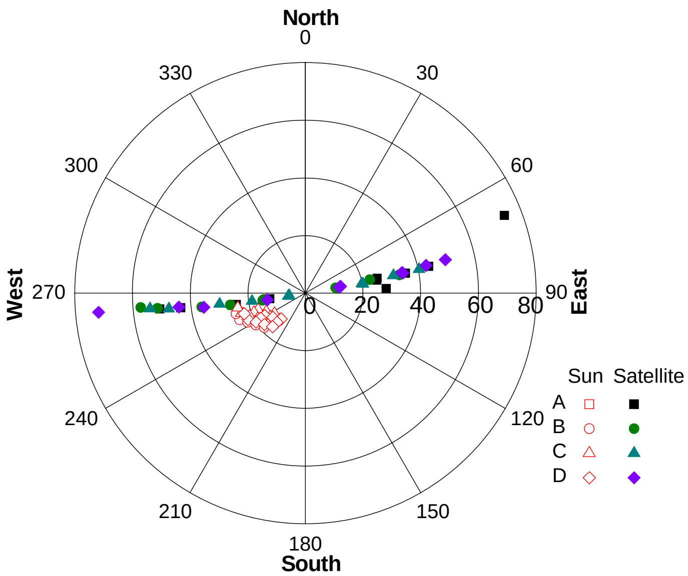

Fig.3-4 Sun and satellite zenith and azimuth angles in polar representation at four locations for ten clear days during the period of July 12 to July 30 of 2005.

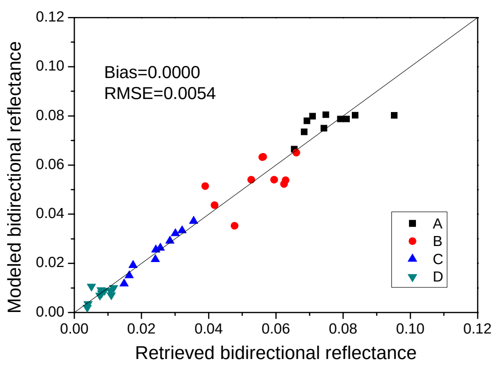

(a)

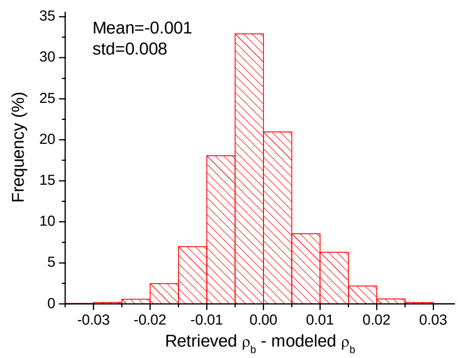

(b)

Fig.3-5 Comparison of the bidirectional reflectances estimated using Eq. (3.1) with those modeled using Eq. (3.5): (a) for locations A, B, C and D, (b) for the entire area.

Table 3-2 gives the fitting parameters of k_{iso}, k_{vol}, and k_{geo} in Eq. (3.5) for locations A, B, C and D. In addition, values of the Normalized Difference Vegetation Index (NDVI) derived with the TOA reflectances in near-infrared and red channels from MYD021KM data for these four locations on July 24, 2005, are also given in this table.

Table 3-2. Fitting parameters k_{iso}, k_{vol}, and k_{geo} in Eq. (3.5) for locations A, B, C, and D

Locations	A	B	C	D
Longitude(°)	32.72	34.31	33.86	31.23
Latitude(°)	30.27	31.24	28.78	30.61
k_{iso}	0.0945	0.0034	0.0450	0.0187
k_{vol}	-0.1699	-0.1316	-0.1474	-0.1351
k_{geo}	0.0274	-0.0574	0.0312	0.0157
NDVI	0.12	0.20	0.08	0.63

To preliminarily validate the directional emissivity estimated using the present method, the MODIS land surface temperature/emissivity product MYD11B1 data were used in our investigation. Taking into account that the MYD11B1 product provides the land surface emissivity values at 5 km resolution, the mean value of estimated directional emissivities for 5×5 pixels with 1 km resolution was selected to match the one from MYD11B1 data with regard to the nearest latitude and longitude coordinates. Fig.3-6(a) displays the directional emissivities estimated using the present method versus those extracted from MODIS land surface temperature/emissivity product MYD11B1 data at four locations for the ten clear days. From this Fig. we can see that the Mean Error (ME) and the Root Mean Square Error (RMSE) are 0.002 and 0.021 respectively. In addition, Fig.3-6(b) shows cross-comparisons of the estimated directional emissivities and those extracted from MYD11B1 data for the entire region for these ten clear days. The ME and RMSE between the directional emissivities estimated in this study and those extracted from MYD11B1 data are of -0.007 and 0.024 respectively. The result of this comparison shows that, at least for our cases, the method described in this paper for estimating the directional emissivity in MIR channel gives results comparable to those in MYD11B1 product.

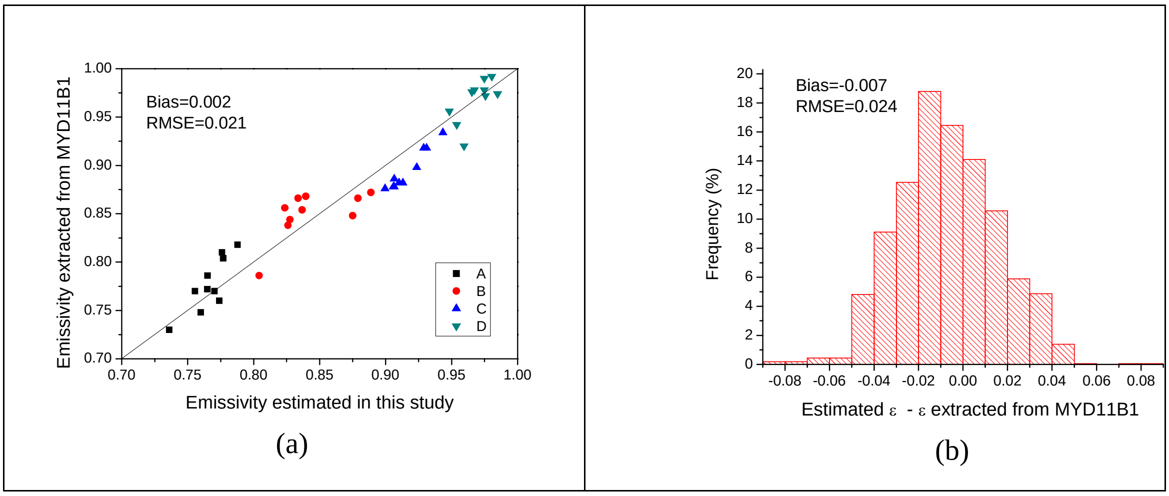

Fig.3-6 Comparison of the directional emissivities estimated from MODIS MIR channels using Eqs. (3.1), (3.5) and (10) with those from MYD11B1 product for ten clear days during July 12 to 30, 2005: (a) for four locations (b) for entire regions.

3.4 Conclusions

In this work, the directional emissivity in MODIS MIR channel has been estimated with the retrieved bidirectional reflectivity and the RossThick-LiSparse-R model. Ten days of MODIS MIR data with cloud-free conditions at the moment of MODIS overpasses, from July 12 to July 30 of 2005 were used to determine the three parameters kiso, kvol and kgeo in Eq. (3.5) for each pixel. The directional emissivities of these days were mapped for a region of Egypt and Israel with latitude varying from 28.0° N to 32.0° N and longitude from 30.0° E to 36.0° E.

In order to show the retrieval accuracy of the proposed method, the MODIS land surface temperature/emissivity product MYD11B1 data have been used to cross-validate preliminarily the directional emissivities derived directly from MODIS MIR data with the method presented in this paper. The results of this comparison showed that, at least for our cases, the proposed method for estimating the directional emissivity gives results comparable to those of MYD11B1 product with Mean Error =-0.007 and Root Mean Square Error =0.024.

Chapter 4

Impact of Spatial LAI Heterogeneity on Estimate of Directional Gap Fraction from SPOT-Satellite Data

Directional gap probability or gap fraction is defined originally as the probability of a beam transferring at a given incident zenith angle through the vegetative canopy without any interception. As a key variable describing canopy structure and biomass spatial distribution, it is used to simplify the 3-D light interception problem to a 1-D problem [Pinty et al., 2004], and has been employed to estimate surface component temperatures from multi-spectral and multi-angular measurements [Francois et al. , 1997; Li et al., 2001; Francois, 2002; Menenti et al, 2008]. Though gap probability can be estimated in situ from optical instrument data such as hemispherical photographs [Leblanc et al., 2005] and usually used to derive leaf area index (LAI) at local scale in field [Jonckheere et al., 2004; Weiss et al., 2004], the field measurements cannot meet the practical demands at large scale. An attractive and unique way to map and monitor LAI and directional gap probability at large scale is to use the space observation from satellite data in the visible and near-infrared bands. Nowadays LAI is widely estimated directly from satellite measurements using different methods [Myneni et al., 1997; Weiss and Baret, 1999; Chen et al., 2002; Fernandes et al., 2003] and the directional gap probability P is estimated from the spatially retrieved LAI by means of the following relationship [Norman et al., 1995; Menenti et al., 2001],

$$P(\theta, LAI) = e^{-A_p LAI/\cos(\theta)} \tag{4.1}$$

where θ is the viewing zenith angle, A_p is the projection of leaf area in perpendicular to incident beam and is related to the leaf angle distribution [Wang et al., 2007]. With this relationship, directional gap probability can be estimated through vegetation structure information including LAI, leaf angle distribution.

Through observation and studies in different scales including foliage [Rochdi et al., 2006], shoot [Smolander and Stenberg, 2003], canopy [Kotz et al., 2004] and landscape [Garrigues et al., 2006a] by remote sensing, ecological and agricultural community, scientists have realized spatial heterogeneity is universal. Besides the spatial heterogeneity of the land surface, non-linearity of the transfer function is another source of uncertainties in the estimation of land surface variables/parameters from remotely sensed data [Hall et al., 1992; Friedl et al., 1995; Pelgrum, 2000; Garrigues, 2006b]. We can notice that the directional gap probability P estimated from Eq.(4.1) is highly non-linear with respect to LAI, which will inevitably induce scaling bias when applied to a coarse pixel. Consequently it is necessary to analyze the scaling effect of the directional gap probability at different scales, and to improve the retrieval accuracy of directional gap probability, and subsequently to improve the accuracy of land surface component temperatures retrieved from multi-spectral and multi-angular satellite data. However, up to now, there are no many efforts in literature devoted to study the scaling effect of the directional gap probability.

This study focuses on the analysis of the scaling effect on the directional gap probability by means of a simple scaling-up scheme and LAI derived from high resolution spatial data. The section 4.1 provides the theoretical framework to estimate the scaling effect of directional gap probability raised by two different aggregation schemes from local scale to larger scale. In section 4.2, we present the different types of remotely sensed LAI images obtained from VALERI (Validation of Land European Remote sensing Instruments) database. In section 4.3, the scaling effect associated with the non-linear relationship between LAI and gap probability is quantified over several types of landscape. In section 4.4, the conclusions of this chapter will be given.

4.1 Theoretical framework

4.1.1 Up-scaling of directional gap probability

There are two different schemes generally used to aggregate the parameters/variables from the local scale to regional or global scale [Pelgrum, 2000], which are depicted in Fig.4-1 and described roughly below: 1) The aggregation of the results which are derived from a distributed model *f* using distributed input variables. Spatially distributed variables $p(x,y)$ (here $LAI^{i}_{sub-pixel}$) are input to a distributed model *f* (here Eq.(4.1)), results of the distributed model *f* are denoted as $f(p)$ (here $P^{i}_{sub-pixel}(\theta)$), then the aggregative result $\overline{f}(p)$ (here $\overline{P}_{pixel}(\theta)$) on a larger scale are deduced (Eq.(4.2)) from distributed results;(see left flow chart of Fig.4-1). 2) The aggregation of input variables before use in an aggregative model *F* (here Eq.(4.3)), thereby producing an aggregative result. Spatially distributed input data $p(x,y)$ (here $LAI^{i}_{sub-pixel}$) are first averaged to $\overline{p}$ (here LAI_{pixel}) from local scale to a larger scale, then $\overline{p}$ is input to aggregative model *F* (Eq. (4.4)), produces aggregative result $F(\overline{p})$ (here$P_{pixel}(\theta)$). (see right flowchart of Fig.4-1)

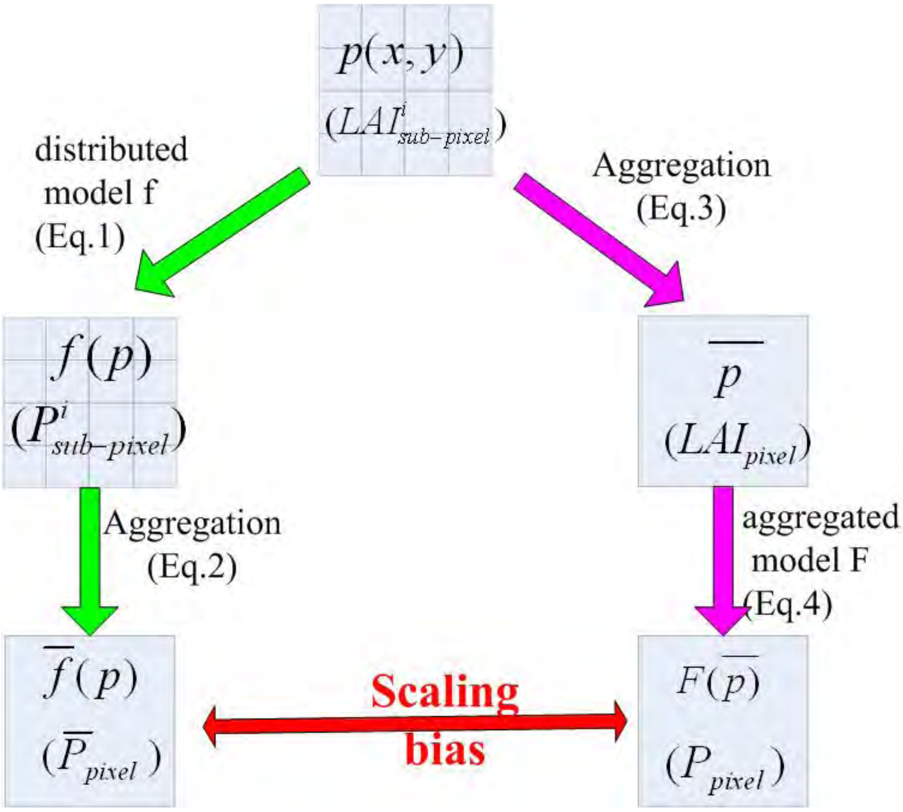

Fig.4-1 General schemes of two aggregation schemes.

As it concerned to gap probability, supposing that the pixel whose area is *S* is composed by *N* homogeneous sub-pixels, each sub-pixel *i* has an area of s_i, $S=\sum_{i=1}^{N} s_i$, the directional gap probability for a given direction (i.e. Viewing Zenith Angle θ) is computed using the first aggregation scheme (see left flowchart of Fig.4-1) with,

$$\overline{P}_{pixel}(\theta) = \frac{\sum_{i=1}^{N} s_i P_{sub-pixel}(\theta)}{S} \tag{4.2}$$

where $P^i_{sub-pixel}$ is the directional gap probability for sub-pixel i, which can be estimated from Eq.(4.1).

The directional gap probability can also be aggregated following the second aggregation scheme (see right flowchart of Fig.4-1) by

$$LAI_{pixel} = \frac{\sum_{i=1}^{N} s_i LAI^i_{sub-pixel}}{S}, \tag{4.3}$$

Then computing the directional gap probability with help of the same formula as Eq.(4.1) by

$$P_{pixel}(\theta) = e^{-A_p LAI_{pixel}/\cos(\theta)} \tag{4.4}$$

4.1.2 Scaling bias of directional gap probability

Since the distributed model related LAI to P is nonlinear (see Eq.(4.1)) and the input LAI data at coarse pixel is heterogeneous, there exists a difference between $\overline{P}_{pixel}$ and P_{pixel}. This difference comes from the different aggregations. To assess the scaling effect of the directional gap probability, inserting Eq.(4.1) into Eq.(4.2) and neglecting the third and higher order terms of the Taylor series expansion, one gets:

$$\overline{P}_{pixel}(\theta) - P_{pixel}(\theta) = P_{pixel}(\theta)\frac{A_p^2}{2\cos^2(\theta)}\delta^2_{LAI} \tag{4.5}$$

With δ_{LAI} is the standard deviation of LAI inside the coarse pixel, i.e. $\delta^2_{LAI} = \frac{\sum_{i=1}^{N} s_i (LAI_i - LAI_{pixel})^2}{S}$

The relative scaling bias (RE) is therefore obtained

$$RE = \frac{\overline{P}_{pixel}(\theta) - P_{pixel}(\theta)}{P_{pixel}(\theta)} = \frac{A_p^2}{2\cos^2(\theta)}\delta^2_{LAI} \tag{4.6}$$

From Eq.(4.6), we notice that the relative scaling bias is only dependent on the A_p, θ and the spatial heterogeneity of LAI within a coarse pixel, but independent on the LAI value itself.

4.1.3 Redefinition of clumping index

In order to take into account the scaling effects of spatial heterogeneity of LAI on estimate of the directional gap fraction and to make the estimation of the directional gap fraction independent on the observation scale and the aggregation schemes used, a parameter Ĉ is introduced in the formula (4.4) so that

$$\exp(-A_p \hat{C}_{pixel} LAI_{pixel} / \cos(\theta)) = \overline{P}_{pixel} \tag{4.7}$$

Following the same development made by Wang and Li [2008], combining Eqs(4.4), (4.5) and (4.7), one gets:

$$\hat{C}_{pixel} = 1 - \frac{\cos(\theta)}{A_p LAI_{pixel}} \ln(1 + \frac{A_p^2}{2\cos^2(\theta)} \delta_{LAI}^2 \tag{4.8}$$

As shown by this equation, the parameter Ĉ is directly proportional to the mean LAI and inversely proportional to the spatial heterogeneity of LAI (δ_{LAI}^2) for given A_p function and direction.

It should be noted that the parameter Ĉ introduced in Eq.(4.7) compensate not only the scaling bias in the estimation of the gap probability, but also has the similar meaning as the so-called leaf dispersion parameter or clumping index (Ω). Traditionally, clumping index is generally used to quantify the heterogeneity of the foliage distribution based on Beer-Lambert's law considering a non-random distribution of foliage in a forest canopy, as vegetation foliage is more often grouped together than regularly spaced relative to the random distribution case [Chen, 1996], and vegetative canopies have different levels of foliage organizations, which contribute to non-random distribution [Chen, 1999]. For Ω = 1, canopy elements are randomly distributed. In clumped canopies, Ω is always less than unity. The smaller the value of Ω, the more the canopy is clumped.

Foliage clumping affects the gap probability for the same LAI by delaying the occurrence of the saturation in reflectance as LAI increases. There have been some studies mostly concentrated on the estimation of clumping index with multi-angular data. Walter et al. [2003] has conducted an experiment involving hemispherical photographs of simulated and real forest canopies to determine clumping index. Leblanc et al. [2005] and Chen et al. [2005] mapped the foliage clumping index over Canada and at the global scale based on the simulated NDHD-clumping index relationships for different cover types. But the capability of clumping index for representing spatial heterogeneity and eliminating scaling bias is rarely concerned.

4.2 Description of the data

The data used here are part of the VALERI database which provides high spatial resolution (20 m) SPOT-HRV scenes for several landscapes sampled (including crops, forest, grassland and shrubs) around world [Baret et al., 2005]. This wide coverage of landscape makes the conclusion of this study more general. Each site has an enough sampling size (about 3km by 3km). Detailed information about each site (including land cover type, location and the date of measurement) is given in table 4-1. More details on the data set and methodology concerned for leaf area index retrieval is referred to Baret et al [2005] and the VALERI web site (www.avignon.inra.fr/valeri).

Table 4-1. Detailed information of remote sensing images used in this research. The last two columns represent the mean (m) and the standard deviation (δ) of LAI respectively

Site name	Land cover type	Date	Lat.	Lon.	m_{LAI}	δ_{LAI}
Aekloba-May01	Palm tree plantation	1/Jun./2001	2.63	99.58	3.54	0.671
Alpilles-March01	Crops	15/Mar./2001	43.81	4.74	0.93	1.15
Barrax-July03	Cropland	3/Jul./2003	39.07	-2.10	0.97	1.41
Fundulea-May02	Crops	9/Jun./2002	44.41	26.59	1.53	1.30
Gilching-July02	Crops and forest	8/Jul./2002	48.08	11.32	5.39	1.79
Hirsikangas-August03	Forest	2/Aug./2003	62.64	27.01	2.55	1.14
Jarvselja-June02	Boreal forest	13/Jul./2002	58.30	27.26	4.20	1.09
Laprida-November01	Grassland	3/Nov./2001	-36.99	-60.55	5.66	2.07
Larose-August03	Mixed forest	18/Sep./2003	45.38	-75.21	5.87	2.00
Larzac-July02	Grassland	12/Jul./2002	43.94	3.12	0.81	0.20
Nezer-April02	Pine forest	21/Apr./2002	44.57	-1.04	2.38	1.11
Rovaniemi-June04	Forest	23/Jul./2004	66.46	25.35	1.25	0.52
Turco-August02	Shrubs	29/Aug./2002	-18.24	-68.19	0.04	0.03

4.3 Results and Discussion

4.3.1 Simulation of relative scaling bias of gap probability

In this study, we adopt a simple formula proposed by Fuchs et al. [1984] to compute the projection value of leaf area in perpendicular to incident beam with mean leaf angle,

$$A_p = \cos(\overline{\theta_L}) \tag{4.9}$$

where $\overline{\theta}_L$ is the mean of leaf inclination angle.

Inserting Eq.(4.9) into Eq.(4.6), we get relative scaling bias of gap probability,

$$RE = \frac{\cos^2(\overline{\theta_L})}{2\cos^2(\theta)}\delta_{LAI}^2 . \tag{4.10}$$

Fig.4-2 displays the results of RE conducted using Eq.(4.10) for $\theta = 0$ and different A_p functions through different mean of leaf inclination angles $\overline{\theta}_L$ given in (4.9).

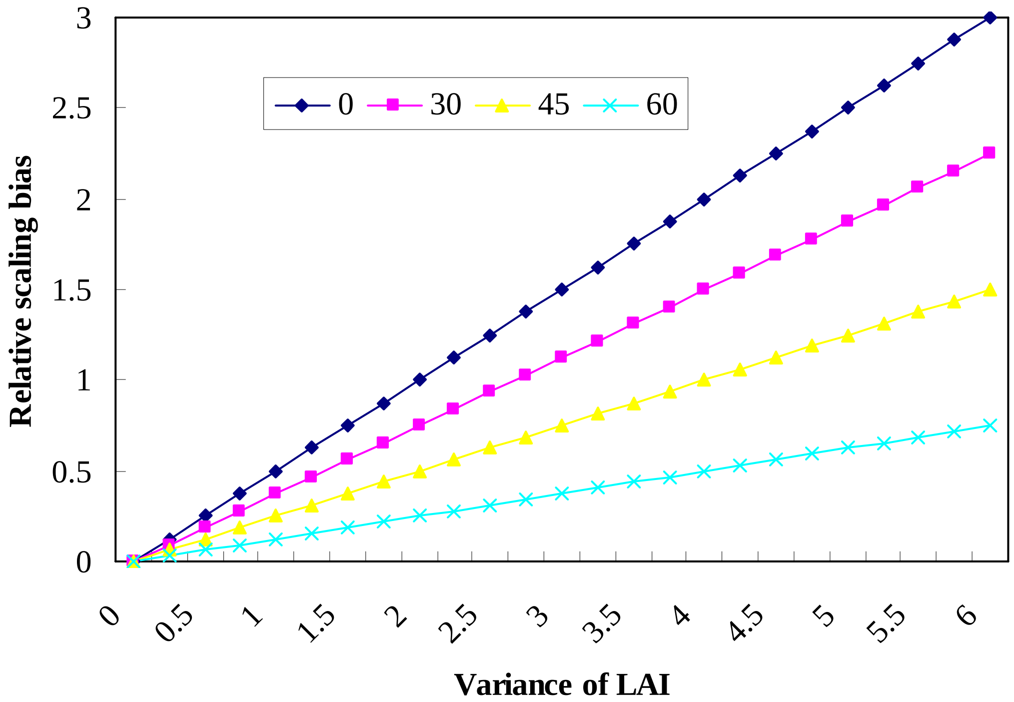

Fig.4-2 Relative scaling bias of gap probability versus the variance of LAI for different mean of leaf inclination angles $\overline{\theta}_L$ (0, 30, 45 and 60 degree) and view zenith angle $\theta = 0$

As shown in Fig.4-2, the relative scaling bias of gap probability is linearly related to the variation of LAI inside the coarse pixel for a given mean of leave inclination angle $\overline{\theta}_L$. As predicted by Eq.(4.10), the slope of this linearity is equal to $\frac{\cos^2(\overline{\theta_L})}{2\cos^2(\theta)}$, and for a given variance of LAI, the larger leaf inclination angle is, the smaller relative error of directional gap probability is. On the other hand, we can conclude that the relative scaling bias varies seasonally since it has relationship with the variance of LAI which is a seasonal variable.

4.3.2 Spatial scaling bias of gap probability obtained from the VALERI dataset

In order to see the magnitude of the spatial scaling bias of directional gap probability with real scenarios, the VALERI dataset is used in this study. Three assumptions are made in the following calculations:

1) Beer's law used to retrieve gap probability from LAI (Eq.(4.1)) is assumed without any scaling bias at 20 m spatial resolution, because no satellite data are available to us at the spatial resolution finer than 20m.

2) Incident beam is assumed to be vertical, i.e. $\cos(\theta) = 1$.

3) A spherical leaf angle distribution is assumed, i.e. A_p=0.5, which is a reasonable assumption for many conifer shoots and closed, broad-leaved canopies [Walter et al., 2003].

Following the schemes proposed and showed in Fig.4-1, with the VALERI dataset described in table 4-1, we compute relative scaling bias of gap probability for each site at different spatial scales using Eq.(4.6). Fig.4-3 displays the relative scaling bias of gap probability in function of the pixel size for different types of land surfaces, such as forest, cropland, grassland and shrubs.

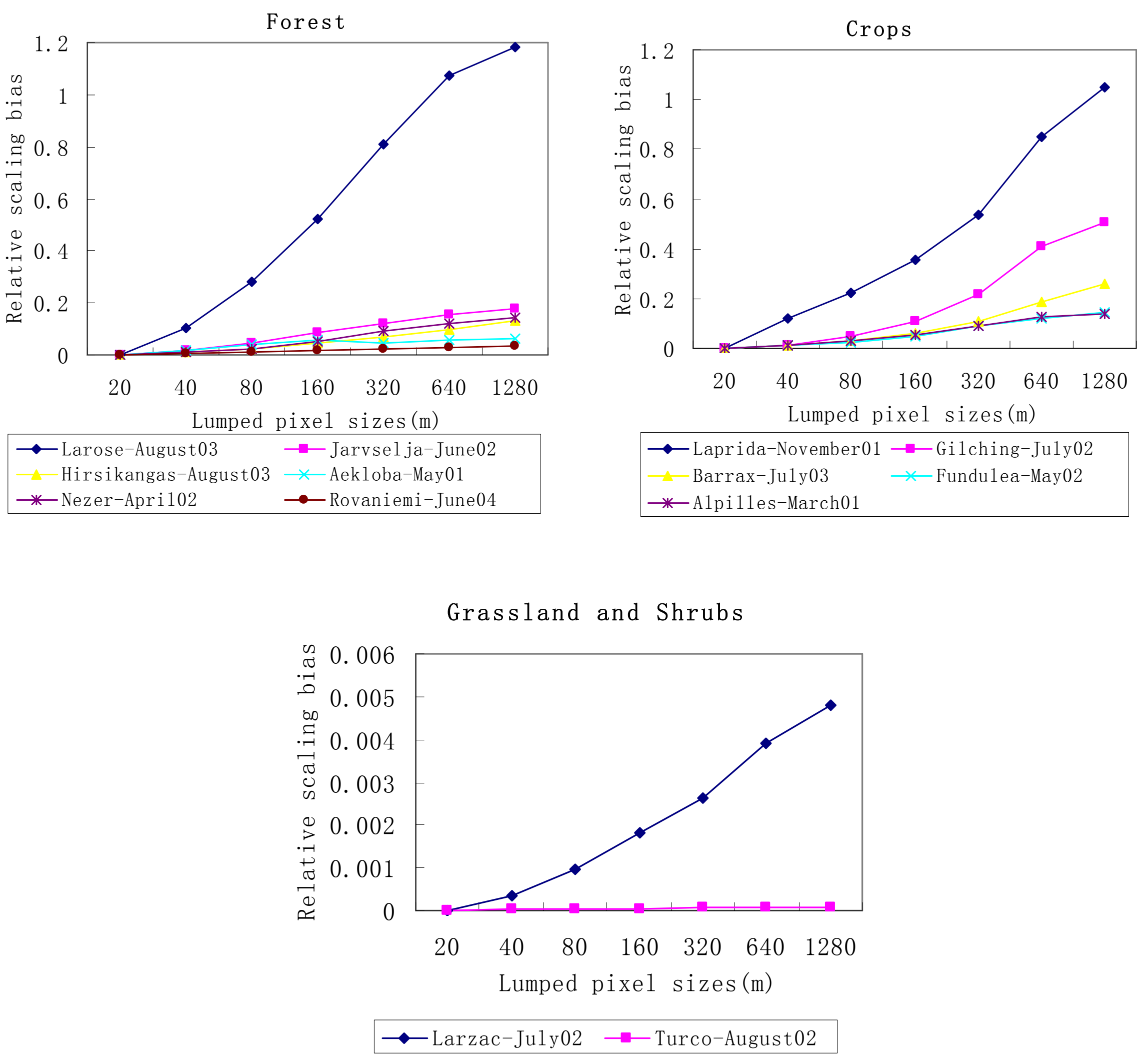

Fig.4-3 Relative scaling bias of gap probability against pixel size for different landscapes: six forest sites, five crops sites, one grassland site and one shrubs site.

From this figure, we notice that the relative scaling bias of gap probability increases with decreasing spatial resolution for most of land cover types. Larger relative bias occurs at crops (104%, 50%, 26%, 14%, at pixel size of 1280m, respectively) than pure forest sites ($\leq 20\%$ at pixel size of 1280m except for the mixed forest (Larose-August03) which has relative bias of 120% at pixel size of 1280m), grassland and shrubs ($\leq 0.5\%$ at pixel size of 1280m), demonstrating that our crops sites are relatively more heterogeneous than forest, grassland and shrubs sites. Previous research conducted by Garrigues et al. [2006b] has gained same conclusion. A large bias occurs over mixed forest site (Larose-August03) due to large variance of LAI with this site, while very small relative biases occur over grassland and shrubs because the variance of LAI over these two sites are small (<0.2) as indicated in table 4-1.

As a result, a large uncertainty (bias) is introduced in estimate of the gap probability from low spatial resolution data such as NOAA-AVHRR or MODIS over large heterogeneous sites if the scaling effects are not considered.

4.3.3 "Clumping index" $\hat{C}$ for VALERI sites

Letting Eq.(4.8) equal to Eq.(4.2), with VALERI dataset, "clumping index" $\hat{C}$ introduced in Eq.(4.7) can be easily obtained for each site at different spatial scales. Fig.4-4 shows the mean value of "clumping index" against the pixel size for different types of land surfaces, such as forest, cropland, grassland and shrubs. Since the SPOT-HRV pixel is supposed to be homogeneous at 20m spatial resolution, the corresponding "clumping index" $\hat{C}$ at original scale is unity (not displayed in Fig.4-4).

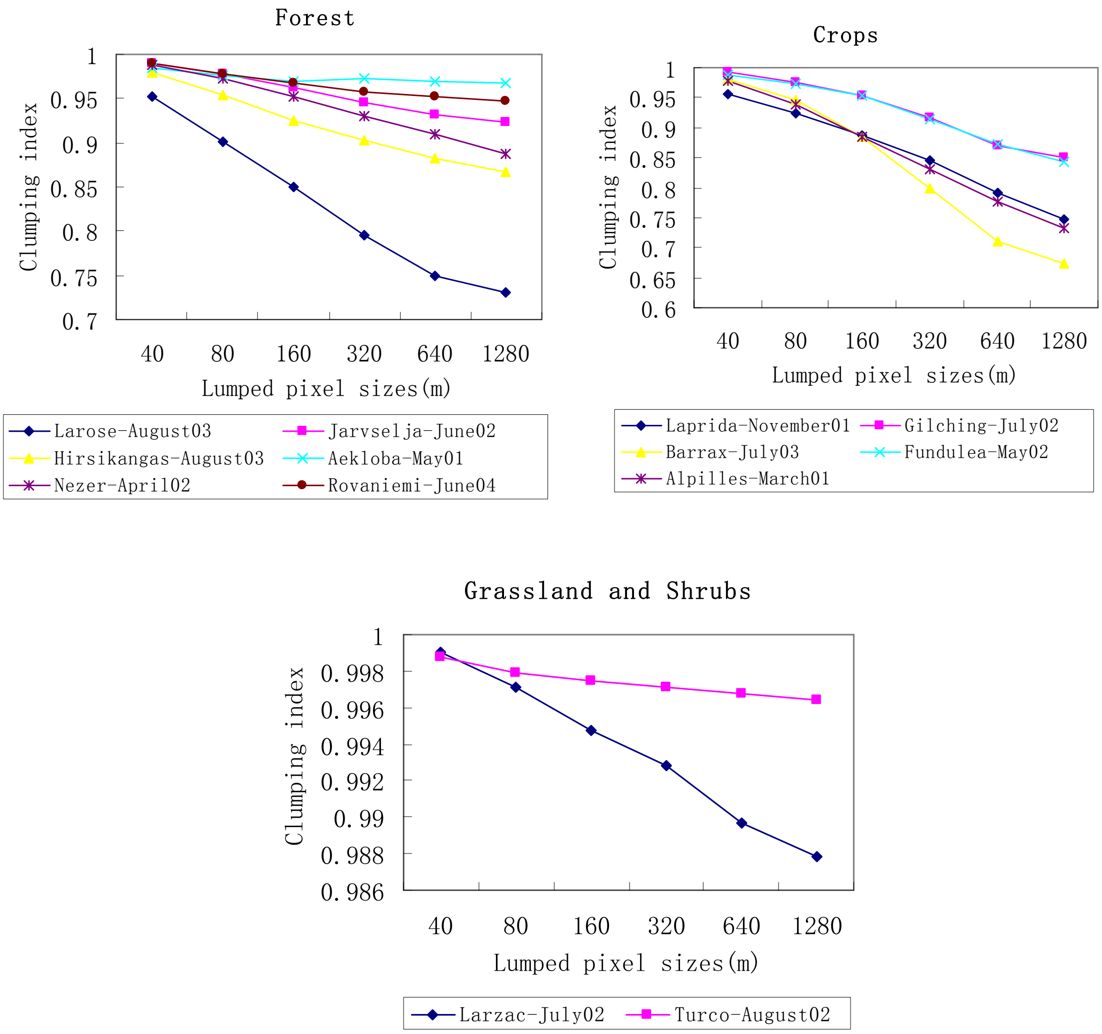

Fig.4-4 Same as Fig.4-3, but with the mean value of clumping index.

As shown in Fig.4-4, "clumping index" varies much for different land cover types and different aggregated sizes. It decreases as aggregative levels increase, indicating that pixel becomes more heterogeneous as demonstrated by the analysis of the relative scaling bias of gap probability given above. Particularly a relative large variation of "clumping index" occurs at Larose-August03, very similar to the relative scaling bias of gap probability. In addition, “clumping index” varies slowly in pure forest, grassland and shrubs sites and more significantly in crops and mixed forest in our cases study. The results demonstrate that less scaling effect correction should be performed for forest and grass sites than crops sites, which is in good agreement with the result shown in Fig.4-3.

As far as sites with the same land cover type are concerned, the magnitude of “clumping index” also varies at different aggregated sizes, and mostly is inversely proportional to the spatial heterogeneity of LAI (δ^2_{LAI}). For example, among forest sites, “clumping index” is minimum at Aekloba-May01, then Rovaniemi-June04, Jarvselja-June02, Nezer-April02, Hirsikangas-August03, and maximum is at Larose-August03, whose δ^2_{LAI} are 0.671, 0.52, 1.09, 1.11, 1.14, 2.00, respectively.

Therefore “clumping index” redefined by Eq.(4.8) has the capability of representing and eliminating scaling bias of directional gap probability induced by the heterogeneity of LAI.

4.4 Conclusion

In this study, spatial scaling effect of the gap probability based on Beer’s law for different types of land cover is analyzed and corrected for by introducing an extension of the “clumping index”, Ĉ which accounts for the spatial heterogeneity.

Analytical expressions developed in this paper show that: 1) relative scaling bias is only dependent on the A_p function and the spatial heterogeneity of LAI, but independent on the LAI value itself, and 2) extension of “clumping index” Ĉ is directly proportional to the mean value of LAI and inversely proportional to the spatial heterogeneity of LAI for given A_p function and direction.

With the VALERI dataset, this study shows that relative scaling bias of gap probability increases and “clumping index” value decreases with decreasing spatial resolution for most of land cover types. Large relative biases and large variation of “clumping index” Ĉ are found for most of crops sites and a mixed forest site due to their relative large variance of LAI, while very small biases and small variation of clumping index are found for grassland and shrubs sites.

The parameters introduced in this paper has endowed a new significance to traditional clumping index and provided evidence to the utility of clumping index as an improvement of the estimate of gap probability from LAI. The results exhibit the capability of clumping index for scaling Beer’ law and representing spatial heterogeneity, as well as the feasibility of the inversion approach for gap probability from remote sensing data. Meanwhile a simple and feasible method to estimate “clumping index” from remote sensing data is also explored from the above experiment, which will provide a support to global mapping of the vegetation clumping index.

Chapter 5

Triangle Feature Space Algorithm for Estimating Land Surface Evapotranspiration from MODIS Data in Arid and Semi-arid Regions

Accurate estimates of spatially averaged Evapotranspiration (ET) over distances of few kilometers equivalent to the spatial scale of satellite remote sensing data and the grid size of numerical models are of crucial importance in disciplines of hydrology, meteorology and agriculture. Though direct measurements of turbulent heat fluxes representative of scales of hundreds and thousands of meters can be conducted by the use of either the radiosonde-based vertical profiles of regionally averaged atmospheric variables in the planetary boundary layer or the flight-path averaged turbulence statistics measured with a turbulence measurement instrument onboard an aircraft [Asanuma and Iemoto, 2007], these direct measurements can only be conducted in large scale field programs occasionally due to the high cost and discontinuity of these measurements. Remote sensing technology can provide land surface parameters such as surface temperature, albedo and vegetation indices, etc which are indispensable to remotely sensed ET models for estimating the area averaged turbulent heat fluxes at regional scale. It is recognized as the only viable means to map regional, meso- and macro-scale patterns of ET at the earth's surface in a globally consistent and economically feasible manner.

Several remotely sensed ET models with varying complexity have been developed to map turbulent heat fluxes at various spatial scales from small "point" scale to large "continental" scale with remotely sensed surface temperature retrieved from thermal infrared channels, albedo and vegetation indices estimated from visible and near infrared spectral bands, and ground based meteorological measurements. These ET models mainly include the simplified empirical method [Jackson et al., 1977], surface energy balance based single- and dual-source models [Hatfield, 1983; Norman et al., 1995], spatial contexture information based on surface temperature-vegetation indices triangular and trapezoidal method [Jiang and Islam, 1999; Moran et al., 1994] and data assimilation techniques [Boni et al., 2001]. (See chapter 1 for more details). Overviews of these models and methods have been provided by a number of authors since 1990s [Kairu, 1991; Kustas and Norman, 1996; Courault et al., 2005; Glenn et al., 2007; Kalma et al., 2008; Li et al., 2009]. Although great progress has been made on the regional remotely sensed estimate of ET with models incorporating land surface parameters retrieved quantitatively from satellite remote sensing data in the past more than 30 years, there are several related problems that have not yet been solved properly. On the one hand, for lack of the validation ET data at large scale, particularly over heterogeneous surfaces with complex geographic terrains and partial vegetative covers, all developed ET models or methods have not been rigorously validated and consequently can not be used in confidence. On the other hand, due to the extra difficulty presented or the lack of the feasible methods to get the spatially representative of ground-based measurements at large scale, such as near surface air temperature, wind speed, vapor pressure deficit and vegetation height, etc from the limited observation networks on the Earth, most of the currently commonly applied remotely sensed ET models can not be used operationally to map ET at large scale.

In order to overcome the latter problem, attempts have been made to develop a parameterization of regional ET with only satellite derived surface parameters, such as the so-called Surface Temperature - Vegetation Index (Ts-VI) triangle method developed by Jiang and Islam [1999; 2001] and improved by Jiang and Islam [2003], Venturini et al. [2004] and Batra et al. [2006]. This type of method relies on the triangular shape formed by the scatter plot of surface temperature (*Ts*) versus vegetation index (*VI*) under a full range of vegetation cover and soil moisture availability within the interesting study region to estimate Evaporative Fraction (EF) and ET at satellite pixel scale. The success of *Ts-VI* triangle method on the estimation of EF and ET depends mainly on the correct choice of the dry and wet edges in the *Ts-VI* triangle space. However, up to now, no rules have been proposed to determine these two edges in the *Ts-VI* triangle space, their determination is somewhat subjective and arbitrary leading to a great uncertainty in the estimation of EF and ET.

The objectives of this work are twofold: (1) to develop an operational algorithm to determine automatically and quantitatively the dry and wet edges for the *Ts-VI* triangular space in arid and semi-arid areas where wet pixels are not generally easily identified, (2) to validate with the in-situ ET measurements made by the Large Aperture Scintillometer (LAS) the ET derived from MODIS/TERRA products using the developed algorithm. Section 5.1 recalls the principle of the *Ts-VI* triangle method and highlights the assumptions involved in the methodological development and the advantages and disadvantages of the *Ts-VI* method. Section 5.2 gives the implementation and application of the proposed method to MODIS data. Section 5.3 describes the study region and data used in the present study and gives a preliminary validation of satellite derived sensible heat flux with the field measurements made by the LAS. Finally, the conclusion is given in section 5.4.

5.1 Methodology

Ts-VI triangle (see Fig.1-3) method applied in this work is originated from the parameterization of Jiang and Islam [1999], in which a simplified Priestley-Taylor formulation [Priestley and Taylor, 1972] with fully remotely sensed data is utilized to estimate regional ET and EF by interpreting the scatter plot constructed from remotely sensed *Ts* and *VI* under conditions of full ranges of soil moisture availability and vegetation cover. This approach is based on an extension of Priestly-Taylor's equation and the existence of physically meaningful relationship between EF and remotely detectable surface characteristic parameters (*Ts, NDVI,* soil moisture, vegetation fraction). The mathematical expression of latent heat flux (LE) is taken as follows [Jiang and Islam, 1999]:

$$LE = \Phi[(R_n - G)\frac{\Delta}{\Delta + \gamma}] \tag{5.1}$$

and according to the definition of EF, EF can be directly estimated from Eq. (5.2) as:

$$EF = \frac{LE}{R_n - G} = \Phi\frac{\Delta}{\Delta + \gamma} \tag{5.2}$$

and LE, can be wrote as:

$$LE = EF(R_n - G) \tag{5.3}$$

with

$$\Delta = 0.20(0.00738Ta + 0.8072)^7 - 0.000116 \tag{5.4}$$

$$\gamma = 0.00163P / L = 0.00163[(101.3 - 0.01055H_{al})/(2.501 - 0.002361T_a)] \tag{5.5}$$

where Φ is a combined-effect parameter which accounts for aerodynamic resistance (-), R_n is surface net radiation (W/m^2), G is soil heat flux (W/m^2), Δ is slope of saturated vapor pressure versus air temperature (kPa/°C), γ is Psychrometric constant(kPa/°C), P is atmospheric pressure (kPa), L is latent heat of vaporization (MJ/kg), T_a is air temperature (℃), H_{al} is altitude height (m).

As shown by Jiang and Islam [1999], the sensitivity of Δ on the variation of temperature is very small. Air temperature (*Ta*) required in Eq. (5.4) and (5.5) to calculate Δ and γ can be obtained either by a linear regression between *Ts* and *Ta* or by using mean surface temperature or mean water surface temperature as a surrogate [Jiang and Islam, 1999; Venturini et al., 2004]. In this work, taking into account and the correlation of *Ts* with air temperature, remotely sensed *Ts* will be used to estimate the parameter Δ and γ instead of the use of air temperature.

Many papers have demonstrated that the *Rn* and *G* in Eq. (5.1) can be estimated with only satellite data. Therefore, in Eq. (5.1), estimation of LE from satellite data alone is to estimate the Φ values from combined *Ts* and *VI* measurements after the *Rn, G* have been determined from remotely sensed data.

Although parameter Φ in Eq. (5.1) looks apparently the same as α in Priestley-Taylor's equation, there is a distinct difference in the physical meaning between these two parameters. In Priestley-Taylor's equation, α is generally interpreted as the ratio of actual evaporation to the equilibrium evaporation and a series of paper has demonstrated this parameter with a good approximate to be 1.26 [Crago and Brutsaert, 1992; Jiang and Islam, 2001]. Priestley-Taylor's equation is generally applicable for wet surfaces whereas Eq. (5.1) holds true for a wide range of surface evaporative conditions with Φ varying from 0 to (Δ+γ)/Δ when significant advection and convection are absent. Jiang and Islam [Jiang and Islam, 1999] have found the upper bound of derived Φ (corresponding to the wet edge in the Ts-VI triangle space) for each NDVI value is very closed to 1.26.

In order to estimate pixel by pixel ET using Eq. (5.1), both dry and wet edges in the *Ts-VI* space have to be first determined. As mentioned above in this chapter, their determination is extreme difficult and often arbitrary. Previous papers [Jiang and Islam, 1999; Carlson, 2007] have recommended taking the surface temperature of a water body and/or a well-irrigated agricultural field as the temperature of wet edge with potential ET. However, these two land surface types can not be easily identified or may not exist at all in most arid and semi-arid areas, an automatic and practical algorithm needs to be developed to determine the dry and wet edges in the triangular space for these areas.

Taking into account that NDVI is just a surface greenness parameter and dependent on spatial resolution of remote sensors [Price, 1990], the commonly employed NDVI in the construction of *Ts-VI* triangle space will be replaced in this work by the fraction of vegetation (*Fr*) which seems to be more representative of the relative proportionality between soil and vegetation within the pixel. As depicted in Fig.1-3, once the two edges (dry and wet) in the *Ts-Fr* space are determined, the value of Φ corresponding to the driest bare soil pixel (at the position *Fr*=0 and maximum surface temperature $T_{s,max}$ in the dry edge line) is set to 0 (denoted as Φ_{min}=0 at pixel ($Fr=0$, $T_{s,max}$)) and the value of Φ at the position *Fr*=1 and the minimum surface temperature $T_{s,min}$ in the dry edge line is set to 1.26 (denoted as Φ_{max}=1.26 at (Fr=1, $T_{s,min}$)). A two-step linear interpolation is then used to get the Φ value for the pixel *i* ($Fr_{,i}$,$T_{s,i}$) in the *Ts-Fr* triangle space：

1) determining Φ_{min} value in the dry edge line for the pixel *i* ($\Phi_{min,i}$) by assuming that $\Phi_{min,i}$ varies linearly with $F_{r,i}$ between Φ_{min}=0 at ($Fr=0$, $T_{s,max}$) and Φ_{max}=1.26 at ($Fr=1$, $T_{s,min}$), and determining Φ_{max} value for the pixel *i* ($\Phi_{max,i}$) in the wet edge line by assuming that $\Phi_{max,i}$ is constant in the wet edge line, i.e. $\Phi_{max,i}$=Φ_{max}=1.26 as the wet edge line is defined as T_s=$T_{s,min}$. The lower limiting value of

Φ for any *Fr* ($\Phi_{min,i}$) in the dry edge can be first derived by a linear interpolation between Φ_{min}=0 at *Fr=0* and Φ_{max}=1.26 at *Fr=1*, namely:

$$\Phi_{\min,i} = 1.26Fr \tag{5.6}$$

2) determining Φ value for the pixel *i* (Φ_i), by assuming that for given *Fr*, Φ increases linearly with the decrease of *Ts* between $\Phi_{min,i}$ and $\Phi_{max,i}$ in the *Ts*-*Fr* triangle, i.e.,

$$\Phi_i = \frac{T_{\max,i} - T_{s,i}}{T_{\max,i} - T_{\min,i}}(\Phi_{\max,i} - \Phi_{\min,i}) + \Phi_{\min,i} \tag{5.7}$$

in which

$$T_{\max,i} = T_{s,\max} + F_r(T_{s,\min} - T_{s,\max})$$

$$T_{\min,i} = T_{s,\min}$$

$$\Phi_{\max,i} = \Phi_{\max} = 1.26$$

5.2 Implementation and application of the method to MODIS data

To apply the above proposed *Ts*-*Fr* triangle method to MODIS data, several steps are needed to be performed as shown in Fig.5-1. The input MODIS data and products are MODIS land surface temperature/emissivity products (MOD11), NDVI (MOD13), together with MODIS calibrated radiances (MOD021KM), MODIS geolocation (MOD03) and MODIS precipitable water product (MOD05). The output datasets consist of the derived R_n, G, EF and ET. Below is the description of each step involved in the algorithm.

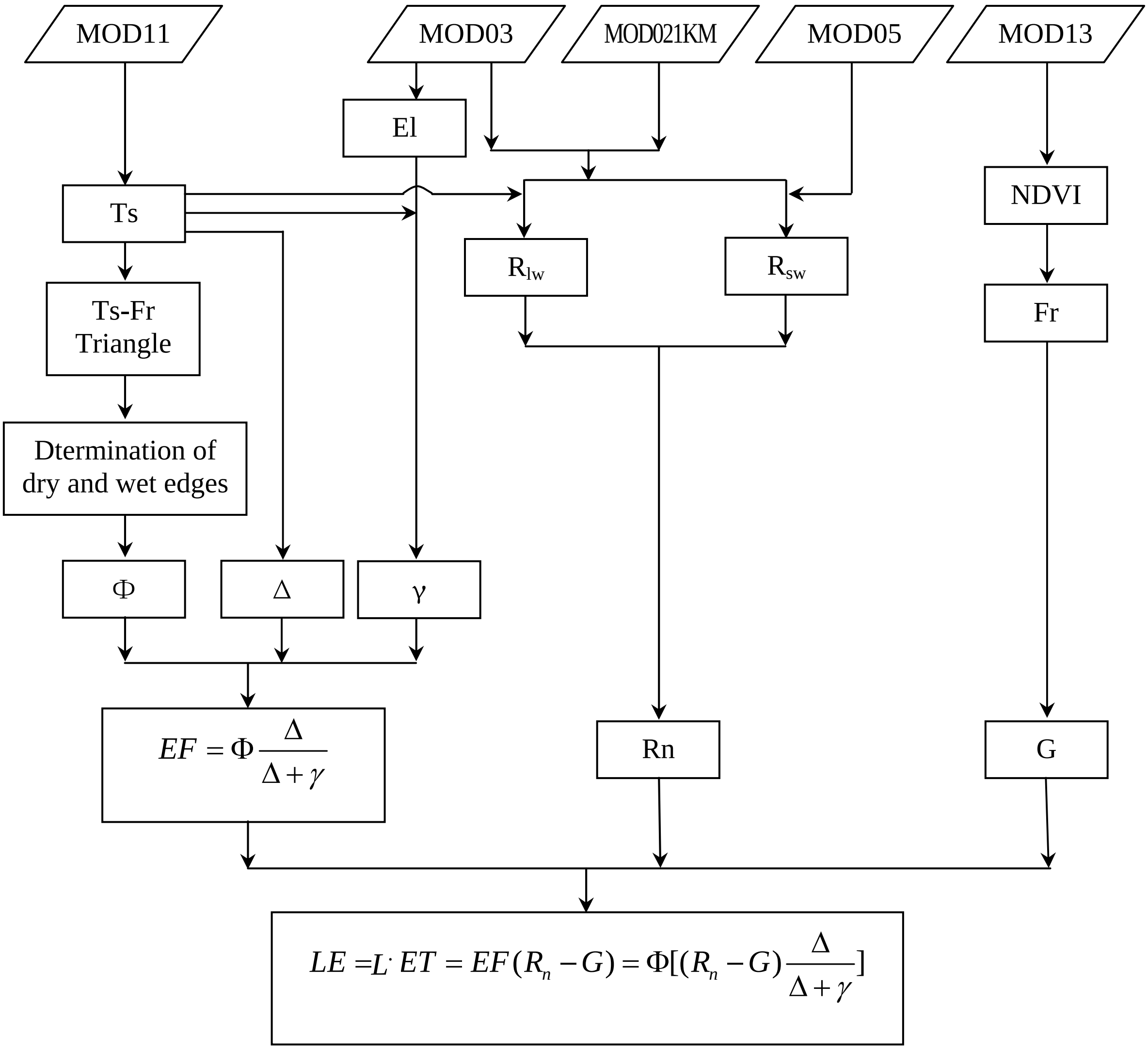

Fig.5-1 Flow chart of the proposed algorithm to estimate the regional surface net radiation, soil heat flux, evaporative fraction and latent heat flux from MODIS data.

5.2.1 Data downloading

MODIS land surface temperature/emissivity and NDVI products, MODIS calibrated radiances and geolocation products, as well as MODIS atmospheric precipitable water product are downloaded from the MODIS data and products centers. In order to establish the *Ts-Fr* triangle space, MODIS land surface temperature/emissivity product (MOD11A1 and MOD11_L2) and NDVI product (MOD13A2) are needed to be first downloaded from the Land Processes Distributed Active Archive Center (LPDAAC) (https://lpdaac.usgs.gov/). In addition, MODIS calibrated radiances (MOD021KM), geolocation (MOD03) and atmospheric precipitable water (MOD05_L2) products are used to estimate the surface net radiation R_n and they can be downloaded from the LAADS (Level 1 and Atmosphere Archive and Distribution System) web (http://ladsweb.nascom.nasa.gov).

5.2.2 Screening out the pixels contaminated by cloud and also the pixels with surface elevation far apart from the average of surface elevation in the study area

Having successfully downloaded all MODIS data and products, some preliminary processing are needed to be performed using MODIS Reprojection Tool (MRT) and MODIS Swath Reprojection Tool (MRTSwath) so that all data and products are well georeferenced and subset corresponding to the study area is easily accomplished. As well known, the cloud affects significantly the satellite-derived Ts, pixel contaminated by cloud in the study area are therefore screened out. In order to satisfy the assumptions involved in the development of Ts-Fr triangle method described in section 5.1, all pixels in the Ts-Fr triangle space should have about the same surface elevation, thus pixels having much higher or lower surface elevation with respect to the average of elevation in the study area are also removed out.

It is worth noting that the subset selected should be as large as possible so that the large ranges of both soil moisture availability and vegetative coverage could be found in the study area.

5.2.3 Calculating Φ pixel by pixel

1) Estimating the fraction of vegetation (*Fr*) within the pixel for each pixel in the study area. As stated in section 5.1, to construct the *Ts-VI* triangle space, *Fr* is used in this work to replace the NDVI. Pixel by pixel *Fr* is therefore estimated from MODIS NDVI product using the formula proposed by Carlson and Ripley [1997]:

$$F_r = (\frac{NDVI - NDVI_{\min}}{NDVI_{\max} - NDVI_{\min}})^2 \tag{5.8}$$

where $NDVI_{min}$ and $NDVI_{max}$ are respectively the minimum NDVI corresponding to bare soil (LAI=0) and the maximum NDVI corresponding to full vegetated surface (LAI=∞). They are assigned respectively to be 0.2 and 0.86 in this work as done by Prihodko and Goward [1997].

2) Constructing the *Ts-Fr* triangle space. Knowing *Ts* and *Fr*, a plot of *Ts* against *Fr* (Ts represents the ordinate axis and *Fr* represents the abscissa) for all remained pixels after the step 2 (i.e. section 5.2.2) in the study area is used to construct the *Ts-Fr* triangle feature space bounded with an upper decreasing envelope (dry edge) and a lower nearly horizontal envelope (wet edge).

3) Determining automatically the dry and wet edges in the *Ts-Fr* triangle space. After having plotted the pixels in our study region in two-dimensional space (Fr, Ts), one needs to determine carefully the dry and wet edges in this *Ts-Fr* space because accurate determination of these two edges has direct impact on the accuracy of the derived EF and turbulent heat fluxes. An iterative process is proposed to determine automatically these two edges and is described as follows: (i) Dividing the range of *Fr* in the *Ts-Fr* triangle space into *M* intervals evenly (M≦20 is recommended) and then dividing each interval into N subintervals (N≧5 is recommended). (ii) For a given interval, finding and saving the maximum temperature within each subinterval. (iii) The average value (T_{aver}) and standard deviation (δ) of the N maximum surface temperatures for N subinterval of this given interval are computed as an initial state. (iv) If the maximum surface temperature of each subinterval of this given interval is less than T_{aver}-δ, this subinterval is discarded in the following steps. (v) The new average value (T_{aver}) and standard deviation (δ) of the maximum surface temperatures of the remaining

subintervals after step (iv) are recomputed. (vi) If the number of remaining subintervals in the given interval is greater than a given threshold value and δ is larger than a given threshold value, go back to step (iv) and repeat the steps (iv)-(vi), otherwise go to step (vii). (vii) Taking Taver as the maximum surface temperature of this given interval and going back to step (ii) until all the maximum surface temperatures are found for all M intervals. (viii) A linear regression between the maximum surface temperature within each Fr interval and Fr value is performed and the Root Mean Square Error (RMSE) is computed. (ix) If the maximum surface temperature for a given interval is 2 times RMSE or more less than the temperature value in the regressed line, this interval will be discarded and the program will go back to step (viii) until the minimum number of intervals is reached or no interval can be further discarded. (x) A final linear regression is performed to obtain the dry edge:

$$T_{\max,i} = a + bF_r \tag{5.9}$$

with the two extreme points ($T_{\max,i} = T_{s,\max}$ at Fr=0 and $T_{\max,i} = T_{s,\min}$ at Fr=1) depicted in Fig.1-3, one gets:

$$a = T_{s,\max} \text{ and } b = T_{s,\min} - T_{s,\max}$$

As mentioned in section 5.1, this work assumes that the wet edge is the line with a constant surface temperature which is equal to that of dry edge at Fr=1, i.e.

$$T_{\min,i} = T_{s,\min}$$

4) Calculating pixel by pixel the combined-effect parameter Φ according to the above-mentioned two-step interpolation scheme. After having determined the dry and wet edges in the *Ts-Fr* triangle space, Eqs.(5.6) and (5.7) are used to compute the Φ value for the pixel *i* ($Fr_{,i}$,$T_{s,i}$).

5.2.4 Calculating EF pixel by pixel

Once the combined-effect parameter Φ is obtained, the evaporative fraction (EF) can be straightforward estimated using Eq. (5.2) with Δ calculated with *Ts* instead of *Ta*.

5.2.5 Estimation of surface net radiation (Rn) directly from MODIS data and products

Surface net radiation is defined as the sum of surface net shortwave radiation (R_{sw}) and net longwave radiation (R_{lw}). In this work, a parameterization of R_{sw} fully based on MODIS products proposed by Tang et al. [2006] is used, namely:

$$R_{sw} = \frac{E_0 \cos(\theta_z)}{D_a^2}(\alpha' - \beta' r) \tag{5.10}$$

with

$$\alpha' = 1 - a_1/\mu - a_2/\mu^x - (1-\exp(-\mu))(a_3 + a_4 w^y)/\mu$$

$$\beta' = 1 + a_5 + a_6 \ln\mu + a_7 w^z$$

$$r = b_0 + \sum_{i=1}^{7} b_i \rho_i$$

where E_0 is solar irradiance at Top Of Atmosphere (TOA), θ_z is the solar zenith angle extracted from MODIS geolocation product (MOD03), D_a is the earth-sun distance in astronomical unit, r is the broadband albedo at TOA, μ is the cosine of solar zenith angle, a_1-a_7, x, y, z are constants for various types of surfaces (Land, Ocean, Snow/Ice) and predefined by Tang et al. [2006] and listed in table 5-1 in this work, w is the precipitable water extracted from MODIS atmospheric precipitable water product (MOD05_L2), b_0-b_7 are the coefficients depending on the viewing zenith angle and the solar zenith angle both retrieved from MOD03, ρ_i is the TOA narrowband reflectance measured by MODIS band i (i=1-7) retrieved from MODIS calibrated radiance product (MOD021KM).

Table5-1. Coefficients for estimating the net surface shortwave radiation from the TOA broadband albedos [Tang et al., 2006]

Surface type	a_1	a_2	a_3	a_4	a_5	a_6	a_7	x	y	z
Land	−0.011	0.179	−0.980	0.929	−0.701	0.090	0.846	0.478	0.052	−0.020
Ocean	0.003	0.166	−0.774	0.733	−0.511	0.059	0.637	0.342	0.067	−0.034
Snow/ice	−0.011	0.163	−0.648	0.631	−0.867	−0.013	0.927	0.510	0.060	0.018

Similar to the calculation of surface net shortwave radiation, Tang and Li [2008b] further proposed a scheme to directly estimate the downward longwave radiation (L_d) from only radiances measured at the TOA by six MODIS thermal infrared channels-28, 29, 31, 33, 34 and 36 and surface emitted radiation from the MODIS land surface temperature/emissivity products (MOD11) using the following formulae:

$$L_d = c_0 + c_1 \times M_{29} + c_2 \times M_{34} + c_3 \times M_{33} + c_4 \times M_{36} + c_5 \times M_{28} + c_6 \times M_{31} \tag{5.11}$$

$$R_{lw} = \varepsilon_s L_d - \sigma \varepsilon_s T_s^4 \tag{5.12}$$

$$\varepsilon_s = 0.273 + 1.778\varepsilon_{31} - 1.807\varepsilon_{31}\varepsilon_{32} - 1.037\varepsilon_{32} + 1.774\varepsilon_{32}^2 \tag{5.13}$$

where c_i (i=0-6) are coefficients depending on the view zenith angle and surface altitude both extracted from MOD03, M is the TOA radiance measured by the MODIS thermal infrared channel extracted from MOD021KM and the number in the subscript indicates the thermal channel of MODIS sensor, ε_s is the surface emissivity, σ is the Stefan-Boltzmann constant (5.67×10^{-8} W/(m^2 K^4)), Ts is surface temperature (K), ε_{31} and ε_{32} are respectively surface emissivity in MODIS channels 31 and 32 retrieved with Ts from MOD11.

Readers are recommended to refer to Tang et al. [2006] and Tang and Li [2008b] for detailed information about these algorithms of retrieving surface net radiation from MODIS products.

5.2.6 Estimating soil heat flux (G) from MODIS data

Soil heat flux (*G*) is the heat energy used to cool or warm the subsurface soil. It is theoretically proportional to the thermal conductivity and vertical temperature gradient in the subsurface soil. Since it is impossible to measure *G* at regional scale at ground, a great number of papers has been devoted to estimating soil heat flux indirectly from certain land surface parameters accessible to satellite data such as Ts, NDVI, LAI, Albedo and *Fr* [Choudhury, 1989; Bastiaanssen, 2000; Allen et al., 2007]. In this work, the ratio of *G* to R_n (Γ) is assumed to be linearly decreased from the dry bare soil to full vegetation cover with the increase of Fr as proposed by Su [2002]:

$$\Gamma = G / R_n = \Gamma_v + (1 - F_r)(\Gamma_s - \Gamma_v) \tag{5.14}$$

where Γ_v and Γ_s are respectively fractions for the full vegetation cover and dry bare soil, according to the in-situ point measurements, Γ=G/Rn ranges from 0.05 for full vegetative cover (*Fr*=1) to a maximum of 0.3 to 0.5 for dry bare soil (*Fr=0*) depending on the different types of soils [Daughtry et al., 1990; Li and Lyons, 1999]. In this work, Γ_v =0.05 and Γ_s = 0.4 (average of 0.3 and 0.5) are assumed.

5.2.7 Estimating ET

Knowing the surface net radiation (Rn), soil heat flux (G) and EF, the ET can be straightforward derived using Eq. (5.1) or (5.3).

5.3 Results and Validation

5.3.1 Study area

Our study area is located in the middle reach of Heihe river basin, northwest China, with the climate being arid in temperate zone and the latitude ranging from 38.7˚N to 39.8˚N and longitude being 98.5˚-102˚E. Heihe river basin is influenced by East Asian Monsoon climate and has heterogeneous distribution of precipitation during the year. Mean annual rainfall in this basin is approximately 174 mm and more than 73 percent of annual rainfall occurs during the rainfall season from June to September. A large and intensive field experiment was conducted in Heihe river basin from May 20th to August 21st 2008. This experiment aims to better understand the hydrological and related ecological processes at watershed scale and to promote the applicability of quantitative remote sensing in watershed science related studies. In the experiment, a very dense network of stations, including automatic meteorological stations, hydrological stations, rain gauges, rainfall radar and flux towers, etc., has been installed to collect atmospheric and ground data. For further information about the Heihe field experiment, readers are referred to Li et al. [2008].

The left image in Fig.5-2 is a yearly IGBP land cover classification map in 2004 over the study area derived from the MODIS land cover (MOD12Q1). Surface elevation in most areas is approximately 1200-1600 m above sea level. A mountain, surface elevation of which is about 3000 m, lies in the southwestern part of the study area. The zone where our LAS instrument was set up is sparsely vegetated surfaces with short grass and agricultural crops as shown in the right image of Fig.5-2.

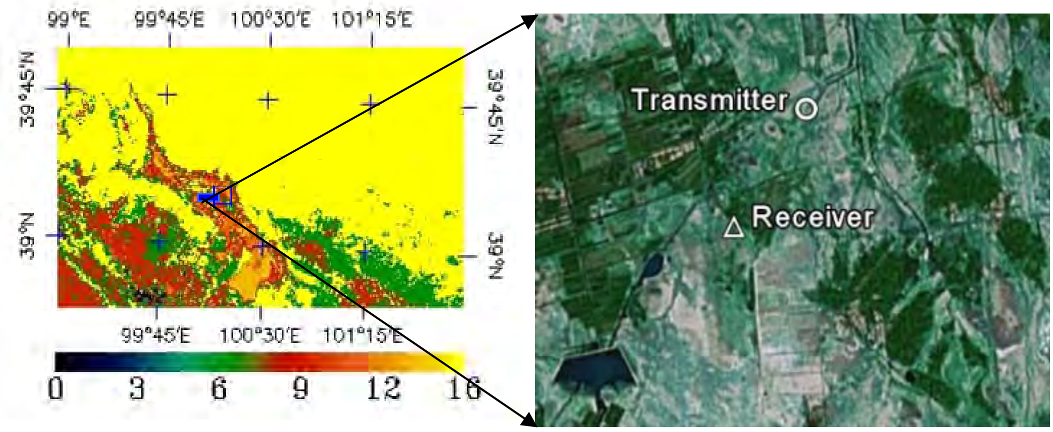

Fig.5-2 A quick view of study area and location of the LAS instrument. The left image is a yearly IGBP land cover classification map in 2004 from MOD12Q1. 0=water, 1=evergreen needleleaf forest, 2=evergreen broadleaf forest, 3=deciduous needleleaf forest, 4=deciduous broadleaf forest, 5=mixed forests, 6=closed shrubland, 7=open shrublands, 8=woody savannas, 9=savannas, 10=grasslands, 11=permanent wetlands, 12=croplands, 13=urban and built-up, 14=cropland/natural vegetation mosaic, 15=snow and ice, 16=barren or sparsely vegetated; The blue filled rectangle in the left image indicates location of the LAS instrument; The right image is the magnified map of the LAS instrument site.

5.3.2 LAS and meteorological data

LAS operations were continually conducted during the Heihe field experiment over flat grassland with Northeast-Southwest orientation from May 20th to August 21st, 2008. Calibration of LAS measurements was made with observations from an Eddy Correlation (EC) system (later dismantled for unknown reasons) nearby the transmitter of the LAS during the first several days after LAS was installed. Location of the LAS is indicated by the blue filled rectangle in the left image of Fig.5-2 and the magnified map of LAS installed area is given in the right image of Fig.5-2. Length path between transmitter and receiver of LAS is 1550 m and the surface elevations of the sites of transmitter and receiver are respectively 1384 m and 1395 m. Both the transmitter and receiver were installed on two tripods fixed with two towers at the heights about 9.25 and 9.1 m respectively above ground. Power was supplied by two different solar power panels and a battery. 10-min interval values of both UCn^2 and signal strength, and the variance of UCn^2 were stored in a built-in data logger.

Two meteorological stations surrounding the transmitter of LAS, namely a station jointly setup by China and Japan (hereinafter referred to as "China-Japan station") before the field experiment and an automatically recorded station (hereinafter referred to as "automatic station") installed during the field experiment, equipped with a set of standard meteorological instruments to measure air temperature, wind speed and direction, relative humidity and atmospheric pressure, etc. were deployed respectively before and during the period of LAS measurements. The meteorological measurements are made respectively at 10 m for China-Japan station and at 1.5 m for the automatic station and are recorded every ten minutes as that of LAS.

Post-processing of the LAS measured data is performed with the support of WINLAS software developed by Kipp and Zonen to calculate sensible heat fluxes representative of spatial averaged values. Inputs to the WINLAS mainly include LAS measurements of UCn^2 and signal strength and additional meteorological observations of wind speed, atmospheric pressure, air temperature, relative humidity and Bowen ratio, surface roughness and displacement height. As Bowen ratio is not a constant during the period of LAS operations and no other Bowen ratio data can be acquired, this work attempts to first estimate Bowen ratio (β) from few-day measurements of the EC system (temporal interval also being 10-min) and then to apply the average values of these Bowen ratio data derived from the same time among different days when EC system was in operation to fill in the vacancy encountered in the subsequent period of measurements of LAS. Since there is no remarkable variation visually in the vegetation height during the period of operation of LAS, surface roughness and displacement height are respectively assigned to the fixed values using rule of thumb assumptions with z_{0m}=0.1m and d=0.5m for simplicity and operational convenience. A sensitivity test is carried out to figure out the impacts of both surface roughness and Bowen ratio on the value of sensible heat flux (H) measured by LAS and processed by the WINLAS software. As an example, LAS-measured sensible heat fluxes calculated with the meteorological measurements at automatic station from 8h to 18h on May 30th are used to perform this sensitivity test. In this test, sensible heat fluxes are first calculated with both Bowen ratio and surface roughness length and displacement height being increased or decreased respectively by 40% to their original values. Then, they are compared with H derived with the original β, z_{0m} and d values. Comparison of this test result is given in Table 5-2. From this table, one can see that the increase/decrease of β value by 40% results only in the increase/decrease of estimated H from LAS by a mean of about 2W/m^2 and RMSE less than 2.5W/m^2, while the increase/decrease of z_{0m} and d values by 40% results in the increase/decrease of estimated H from LAS by a mean less than 9W/m^2 and RMSE less than 15W/m^2 and the impact of errors in z_{0m} and d on the derived H from LAS is larger than that of error in β.

Table 5-2. Sensitivity analysis of LAS-measured sensible heat on two groups of parameters: (1) Bowen ratio (β), (2) Surface roughness length for momentum (z_{0m}) and displacement height (d).

	0.6β	1.4β	0.6z_{0m} and 0.6d	1.4z_{0m} and 1.4d
Bias(W/m^2)	-2.1	0.9	-3.8	8.6
RMSE(W/m^2)	2.3	1.0	7.7	14.1

As two meteorological stations operated near our LAS instrument, one is the China-Japan station which was in operation during the whole period of the field experiment and another is the automatic station operated only from May 26th to July 16th. Since the LAS instrument can not measure directly the sensible heat flux (H), H can only be derived from LAS measured data in combination with Bowen ratio, surface roughness length, displacement height and the atmospheric parameters/variables measured at meteorological station as described above. Fig.5-3 shows that the sensible heat fluxes estimated from LAS data with atmospheric parameters/variables measured at China-Japan station are in good agreement with H derived from LAS data using the atmospheric parameters/variables measured at automatic station at the time overlapped with MODIS overpass although H estimated using automatic station seems slightly larger than that derived using China-Japan station at higher H values. The RMSE between them is 9.41W/m^2 and R^2 is 0.962. Therefore, in the following, only H derived from LAS data using atmospheric parameters/variables measured at the China-Japan station will be compared with H derived from MODIS data using the *Ts-Fr* triangle method.

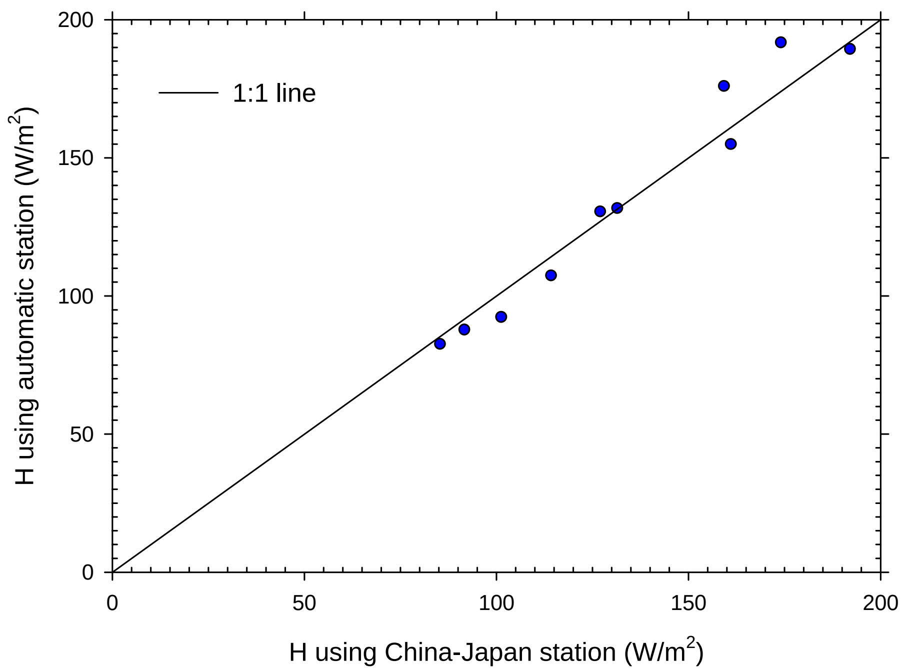

Fig.5-3 Comparison of LAS-measured sensible heat fluxes calculated respectively using measurements at China-Japan station and automatic station.

In order to evaluate the reliability of inferred LAS-measured sensible heat fluxes H, a comparison of H derived respectively from EC (Eddy Correlation) system and LAS measurements on May 20th from 8h to 18h. The results showed that relatively good agreement is observed between LAS-measured and EC-measured H though EC-measured H is slightly higher than that deduced from LAS measurements, and LAS-measured H is much more stable in the daytime evolution whereas H derived from EC fluctuates seriously with time.

5.3.3 Remote sensing data

MODIS data products used in this work are land surface temperature/emissivity (MOD11A1 and MOD11_L2), NDVI (MOD13A2), Calibrated radiances (MOD021KM), Geolocation (MOD03), Precipitable water (MOD05_L2) products. All 24 clear-sky MODIS data from May 23rd to August 21st over our study area are used to estimate the EF, ET and H using the Ts-Fr triangle method/algorithm proposed in this work. The overpass time (local solar time) corresponding to the 24 clear-sky MODIS data varies approximately from 10:06 to 11:42AM.

MOD11A1 (MODIS/Terra Land Surface Temperature/Emissivity Daily L3 Global 1km SIN Grid) and MOD13A2 (MODIS/Terra Vegetation Indices 16-Day L3 Global 1km SIN Grid)，generated by the MODIS Adaptive Processing System (MODAPS) at the U. S. Geological Survey EROS Data Center (EDC), are stored as gridded level 3 products in the Integerized Sinusoidal projection with a nominal spatial resolution of 1 km (about 926 m) in the HDF (Hierarchical Data Format) format. Daytime surface temperature data (LST_Day_1km), daytime overpass time (Day_view_time) and 16-day NDVI data (1_km_16_days_NDVI) extracted respectively from the MOD11A1 and MOD13A2 products are re-projected to Albers Equal Area (AEA) projection with the MRT (MODIS Reprojection Tool). The difference between MOD11_L2 and MOD11A1 is the different spatial resolution, in which the spatial resolution of MOD11_L2 product is 1000 m same as that of the following three MODIS products.

MOD021KM, MOD03 and MOD05 can be accessed from the LAADS (Level 1 and Atmosphere Archive and Distribution System) web. MOD021KM is consisted of calibrated and geolocated TOA radiances and reflectances for 36 bands. MOD03 product mainly includes datasets of geodetic coordinates (latitude and longitude), solar zenith and azimuth angle, satellite zenith and azimuth angle, and ground elevation for each 1-km sample (pixel). MOD05_L2 contains column water-vapor amounts over clear land areas and above clouds over both land and ocean.

5.3.4 Results and Validation

The algorithm described in section 5.2 is applied to all 24 clear-sky MODIS data acquired over our study area. As an example, Fig.5-4 shows a plot of *Ts* against *Fr* in the two-dimensional space for MODIS data acquired on Julian day 201 and the corresponding dry and wet edges determined automatically by the proposed algorithm. This figure confirms the hypothesis that the pixels in the study area forms a triangle in the two-dimensional space *Ts-Fr* and the dry and wet edges can be determined on the basis of the triangle space using our proposed algorithm. Similar results are obtained for other 23 clear-sky days.

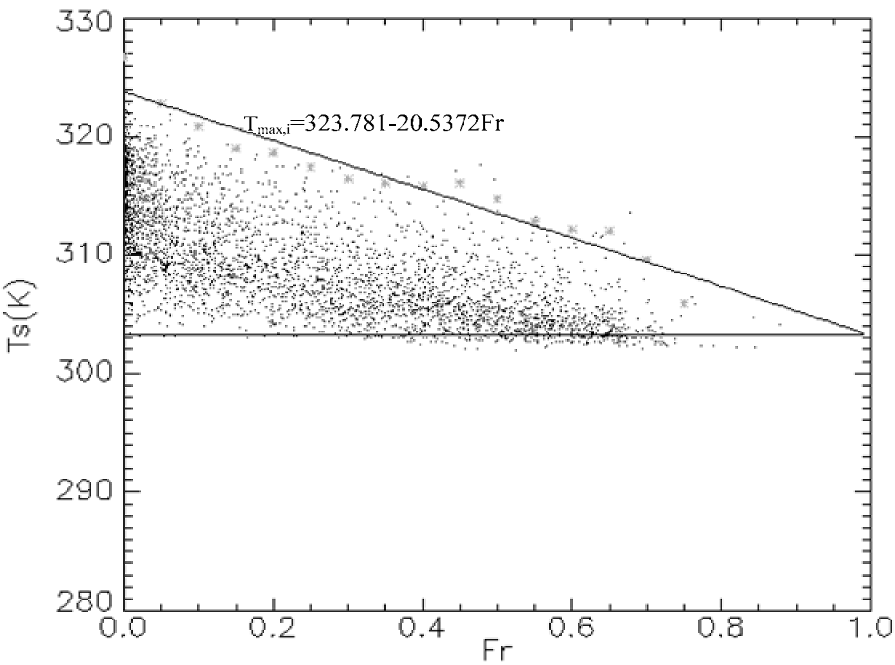

Fig.5-4 A plot of *Ts* against *Fr* in the two-dimensional space for MODIS data acquired on day 201 and the corresponding dry and wet edges determined automatically by the proposed algorithm.

Fig.5-5 shows the surface net radiation (*Rn*), soil heat flux (*G*) and sensible heat flux (H) estimated from MODIS data alone on the LAS instrument site using our proposed method and algorithm for 24 clear-sky days at MODIS overpass time. From this figure, one can see that the Rn for all 24 clear-sky days varies from about 518 to 739 W/m^2 with the mean value of 618 W/m^2. The minimum and maximum Rn values occur on Julian days 226 and 177 respectively. There is no remarkable variation in the soil heat flux as the fractional vegetation cover changes a bit from 0.02 to 0.29 during this period. The mean, minimum and maximum values of soil heat flux are 209, 172 and 248W/m^2 respectively. In most cases, MODIS-derived sensible heat flux is smaller than the soil heat flux at the LAS site.

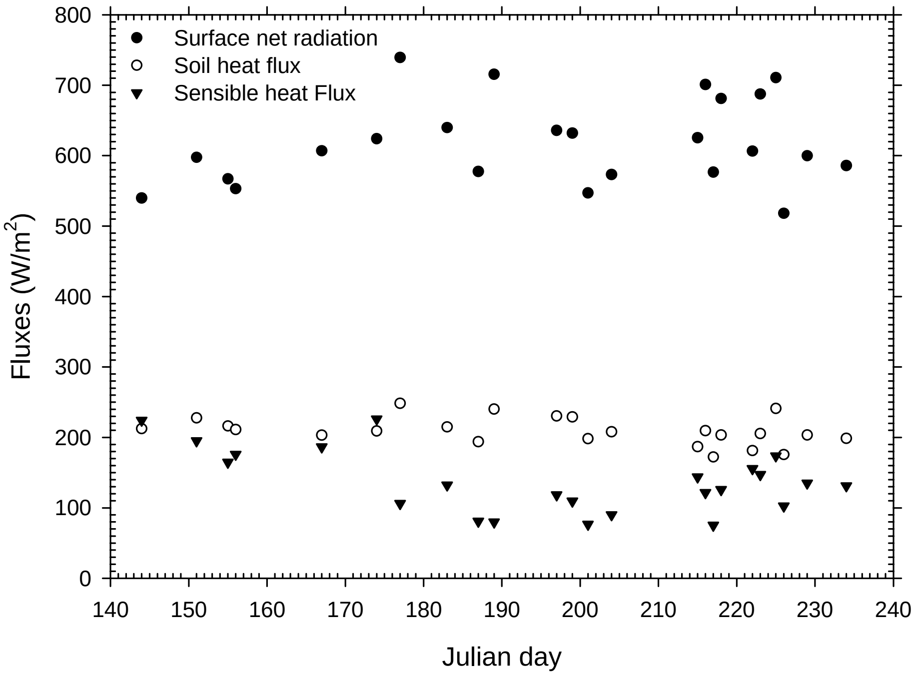

Fig.5-5 Surface net radiation, soil heat flux and sensible heat flux of the LAS site derived from MODIS data using our proposed algorithm for 24 clear-sky days.

Fig.5-6 displays EF estimated from MODIS data alone on the LAS site using our proposed method and algorithm for 24 clear-sky days at MODIS overpass time. One can see from this figure that EF varies from 0.315 (day 144) to 0.832 (day 189) with the mean value of 0.659. EF increases rapidly from the end of May to the end of June, Before June 30th, EF is generally lower than 0.55 (an exception occurs on Julian day 177 while during the period of July to August, EF varies mainly from 0.63 to 0.83. This relatively high EF during the period from the end of June to August may be due to the fact that this period is within the period of rainfall season in our study area.

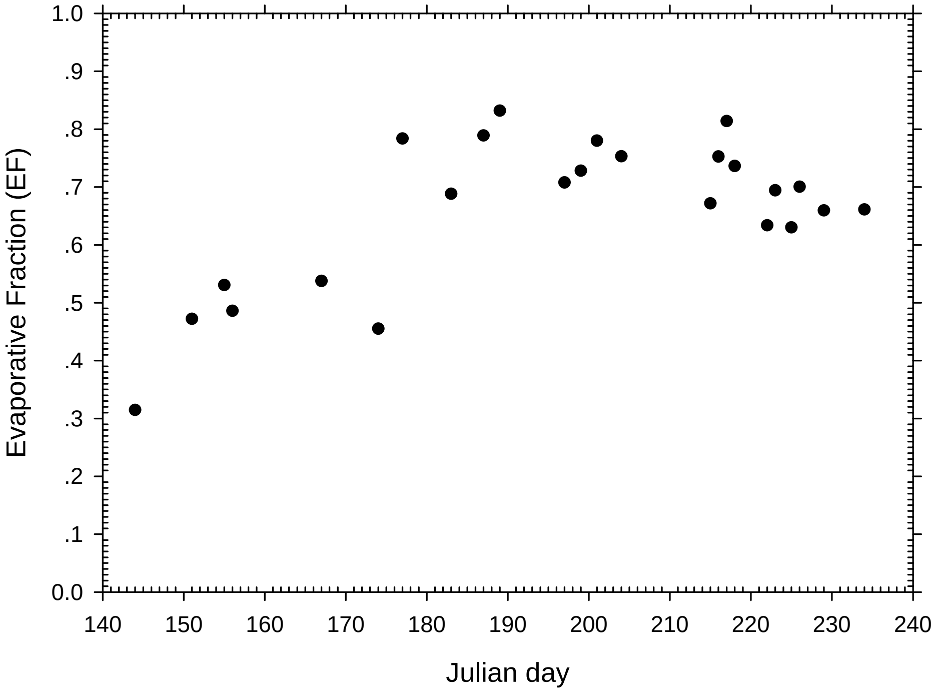

Fig.5-6 Evaporative fraction of the LAS site estimated from MODIS data using the proposed algorithm for 24 clear-sky days

Fig.5-7 illustrates the highest surface temperature ($T_{s,max}$) at the dry edge and surface temperature for the wet edge ($T_{s,min}$, the lowest surface temperature at the dry edge) obtained using our proposed method and algorithm for 24 clear-sky days at MODIS overpass time. These surface temperatures are deduced from the determined dry edges for the 24 Ts-Fr triangles. $T_{s,max}$ varies from 316.8 (Julian day 222) to 332.2 K (Julian day 204) and $T_{s,min}$ from 277.8 (Julian day 144) to 308.6 K (Julian day 183). It should be noted that full ranges of fractional vegetation cover is of crucial importance for the determination of dry and wet edges in our work, which gives a possible explanation to the relatively low $T_{s,min}$ on Julian day 144 over the study area since the variation of Fr is only from 0 to 0.4. R^2 for the linear fit of the dry edge in all 24 constructed Ts-Fr triangles ranges from 0.829 to 0.982, implying that Eq. (5.9) can well depict the relationship between Ts and Fr in the dry edge.

As a validation, Fig.5-8 shows a comparison of MODIS-derived H using our proposed method and algorithm with LAS-measured H for 24 clear-sky days during the period of LAS operation. A very good agreement can be found in this figure with RMSE = 25.07 W/m^2. MODIS-derived H varies from about 75.3 to 226.2 W/m^2 with the mean value of 136.7 W/m^2. Large discrepancies (ΔH) between MODIS-derived H and LAS-measured H occur on Julian days 167 (ΔH=55.3 W/m^2), 174 (ΔH=67 W/m^2), 217 (ΔH=-49.7 W/m^2), and 226 (ΔH=-40.6 W/m^2). On Julian days 165 and 173, heavy rainfalls were took place in the study area, leading to an inaccurate determination of dry and wet edges (i.e. $T_{s,max}$ and ($T_{s,max}$-$T_{s,min}$) decrease), and causing probably an underestimation of EF and an overestimation of H on Julian days 167 and 174.

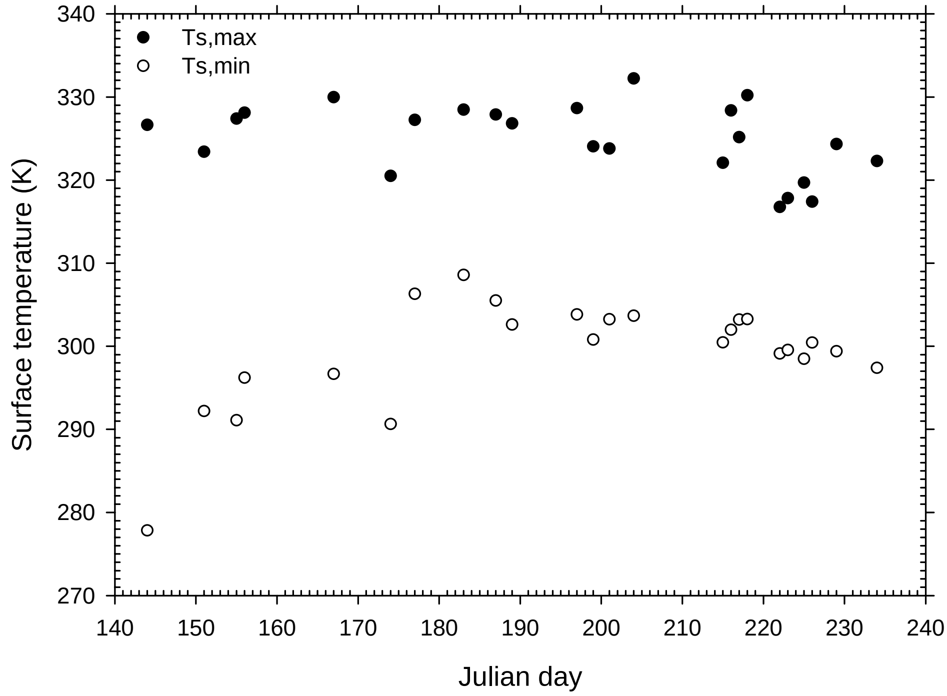

Fig.5-7 The highest surface temperature at the dry edge ($T_{s,max}$) and surface temperature at the wet edge ($T_{s,min}$) inferred from MODIS data using our proposed algorithm for 24 clear-sky days.

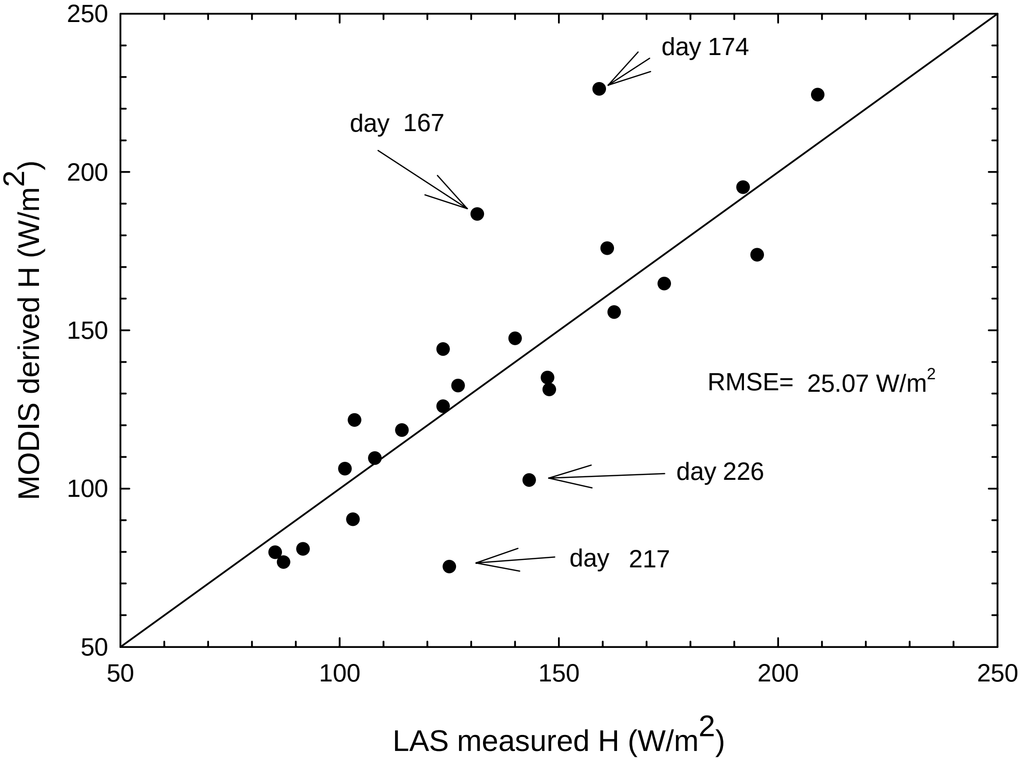

Fig.5-8 Comparisons of sensible heat flux estimated from MODIS data using our proposed algorithm with that measured by LAS instrument for 24 clear-sky days

Due to the lack of sufficient information, it is not yet possible for us to explain the possible reasons for relatively large discrepancies found on Julian days 217 and 226. It might be related to the relatively low surface net radiation (R_n=576 W/m^2, 518W/m^2 for Julian days 217 and 226 respectively) derived at MODIS overpass time on these days when compared with values estimated on Julian days 216 (Rn=710 W/m^2) and 225 (Rn=710 W/m^2). An advantage in the Ts-Fr triangle method is that inaccurate determination of dry and wet edges can also result in an accurate combined-effect parameter Φ and evaporative fraction for a given pixel ($T_{s,i}$, Fr) as long as the ratio of difference between $T_{s,i}$ and $T_{max,i}$ to the difference between $T_{max,i}$ and $T_{min,i}$ (see Fig.1-3) does not change for a given Fr.

It should be emphasized that uncertainties in the sensible heat flux derived from Ts-Fr triangle is partly attributed to the uncertainty related to the estimation of both R_n and G. Tang et al. [2006] reported the RMSE of less than 20 W/m^2 for clear sky days by comparing the estimated surface net shortwave radiation with MODIS products with in-situ measured values at YuCheng field site during an extended period of time covering all seasons in 2003. A comparison of estimated surface net longwave radiation from Tang and Li [2008b] with field measurements at six sites of the Surface Radiation Budget Network in United States has shown a RMSE of approximately 26 W/m^2 at MODIS overpass time of cloud-free days in 2006. Though G accounts for merely a small portion of R_n over partially vegetated areas, it will have more or less influences on the uncertainties of the estimated sensible and latent heat fluxes. Unfortunately, as there are no in-situ measurements of both R_n and G available at the grassland where LAS was placed from May to August, 2008, it is impossible to further investigate the sources of uncertainties in sensible and latent heat fluxes.

5.4 Conclusions

A practical algorithm is developed for quantitative determination of dry and wet edges for the *Ts-VI* triangle method from MODIS/Terra data and products. This algorithm can provide an estimation of surface net radiation, soil heat flux, evaporative fraction and evapotranspiration at regional scale from MODIS data and products alone. Advantages of *Ts-Fr* triangle method over the residual method of surface energy balance are that 1) absolute high accuracy in remotely *Ts* retrieval and atmospheric correction are not indispensable and 2) complex parameterization of aerodynamic resistance and uncertainty originated from replacement of aerodynamic temperature by remotely sensed *Ts* is bypassed, and 3) no ground-based near surface measurements are needed rather than remotely sensed *Ts* and *Fr*, 4) a direct calculation of evaporative fraction (EF), defined as the ratio of latent heat flux to surface available energy, can be obtained without resort to surface energy balance. Limitations of *Ts-Fr* triangle mainly lie in the arbitrary determination of both dry and wet edges and a large number of pixels over a flat area with a wide range of soil moisture and fractional vegetation cover are required.

Determination of dry and wet wedges in *Ts-VI* triangle space generally involves a large degree of subjectivity and uncertainty. The rules and algorithm proposed in this paper give a feasible way to estimate the highest surface temperature at each Fr interval and subsequently determine the dry and wet edges in arid and semi-arid climate region from the *Ts-Fr* triangle space. Although assumption of two-step linear interpolation scheme involved in the estimation of the combined-effect parameter Φ and EF is still questionable and not yet verified directly, a very good agreement is found with the RMSE = 25.07 W/m2 when sensible heat flux estimated from MODIS data is compared with that measured by LAS instrument.

To reduce the uncertainty in the estimation of turbulent heat fluxes from the *Ts-Fr* method, further work needs to be carried out to verify the relevant parameters/variables step by step provided that data required are available in the future and more validation work needs to be performed in other different regions for the proposed algorithm.

Chapter 6

Conclusions and Prospects

This chapter presents the general conclusions of this thesis and gives some prospects and directions for future improvement of the land surface evapotranspiration estimation.

6.1 Conclusions

This work concerns the methodological development permitting to determine the regional land surface EvapoTranspiration (ET) from the MODIS data onboard the polar satellite Terra. It focuses mainly on the retrieval of land surface temperature (LST), the restitution of the directional land surface emissivity, the study of the scaling effects of satellite-derived surface parameters/variables and the estimation of regional ET from remote sensing data alone.

In terms of the retrieval of land surface temperature, on the basis of the radiative transfer theory, this work addressed the estimate of LST from the Chinese first operational geostationary meteorological satellite-FengYun-2C (FY-2C) data in two thermal infrared channels (IR1, 10.3-11.3   m and IR2, 11.5-12.5   m), using the Generalized Split-Window (GSW) algorithm proposed by Wan and Dozier (1996). Following conclusions can be made: 1) taking into account the fact that the S-VISSR sensor onboard FY-2C has no atmospheric sounding channels, the coefficients in the GSW algorithm were derived by dividing the ranges of the mean emissivity, the atmospheric Water Vapor Content (WVC), and the LST into tractable sub-ranges, and were recalculated using a statistical regression method from the numerical values simulated with an accurate atmospheric radiative transfer model MODTRAN 4 over a wide range of the atmospheric and surface conditions. The simulation analysis showed that the LST could be estimated by the GSW algorithm with the Root Mean Square Error (RMSE) less than 1 K for the sub-ranges with the Viewing Zenith Angle (VZA) less than 30° or for the sub-ranges with VZA less than 60° and the atmospheric WVC less than 3.5 g/cm^2 provided that the Land Surface Emissivities (LSEs) are known. 2) as the GSW algorithm requires WVC and LSE as model input, the MODIS total precipitable water product MOD05 providing the atmospheric column water vapor amounts, was used to obtain the WVC when the scanning times of the sensors MODIS and S-VISSR are close to each other. As for the other scanning times of S-VISSR, the atmospheric WVC can be determined using the method developed by Li et al. (2003). As for LSE, the MODIS/Terra LST product MOD11B1 providing the LSEs with 5 km resolution for the thermal infrared channels 31 and 32, was used to derive the LSEs in S-VISSR channels IR1 and IR2, respectively. 3) the sensitivities and error analyses in term of the uncertainty of the LSE and WVC as well as the instrumental noise showed that the accuracy of retrieval LST can be affected by 3% for NEΔT(Noise Equivalent Temperature Difference)=0.1K, by 16% for NEΔT=0.2K, and by 81% for NEΔT=0.5K for the sub-range $\varepsilon \in [0.94,1.0]$, WVC$\in$[1.0,2.5], and Ts$\in$[290K,310K]; given the uncertainties of $(1-\varepsilon)/\varepsilon$ and $\Delta\varepsilon/\varepsilon^2$ around 1%, the LST error is [1.3K, 1.5K] with the mean of 1.4 K for the dry atmosphere and [0.2K, 0.8K] with the mean of 0.5 K for the wet atmosphere; and the effect of the uncertainty of the WVC on the retrieval LST could be around 0.3 K. 4) in order to compare the different formulations of the split-window algorithm, several split-window algorithms were used to estimate the LST with the same simulated FY-2C data. The result of the intercomparsion showed that most of the algorithms give comparable results, which indicates that the split-window algorithm can be successfully applied to the LST retrievals from FY-2C data.

As for the restitution of the directional land surface emissivity, this work proposed a two steps method to estimate the directional emissivity in the mid-infrared (MIR) channel around 4.0 μm from MODIS data. The first step is to retrieve the bidirectional reflectivity in MIR channel from two adjacent MIR channels 22 and 23 of MODIS centered at 3.97 *um* and 4.06 *um* respectively onboard Terra and Aqua satellites. On the basis of the difference in the solar reflection in these two channels, and assuming that the surface bidirectional reflectivities are equal in channels 22 and 23, and that the ground brightness temperatures in these two adjacent channels are the same if the contribution of the direct solar radiation is not considered, the method developed by Tang and Li [2008a] can be used to retrieve the bidirectional reflectivity (ρ_b) in the MIR channel from MODIS channels 22 and 23. The second step is then used to estimate the directional emissivity in MIR channel from the bidirectional reflectivity with the model developed by Jiang and Li [2008]. In order to show the retrieval accuracy of the proposed method, firstly a region of Egypt and Israel with latitude from 28.0° N to 32.0° N and longitude from 30.0° E to 36.0° E and its MODIS images were taken as an example to estimate the directional emissivity directly from MODIS MIR data using the proposed method, then the MODIS land surface temperature/emissivity product MYD11B1 data have been used to cross-validate preliminary estimating values. The results of this comparison showed that, at least for our cases, the proposed method for estimating the directional emissivity gives results comparable to those of MYD11B1 product with Mean Error =-0.007 and Root Mean Square Error =0.024.

In terms of the study of the scaling effects of satellite-derived surface parameters/variables, this work was devoted to study the impact of spatial heterogeneity of leaf area index (LAI) on the estimate of directional gap fraction through aggregating the high-resolution directional gap probability (pixel size of 20 meters) estimated from LAI images of VALERI (Validation of Land European Remote sensing Instruments) database by means of Beer's law. An extension of clumping index, $\hat{C}$, was introduced to compensate the scaling bias. The results obtained in this work showed that the scaling effect depends on both the surface heterogeneity and the nonlinearity degree of the retrieved function. Analytical expressions for the scaling bias of gap probability and $\hat{C}$ were established in function of the variance of LAI and the mean value of LAI in a coarse pixel. With the VALERI dataset, the study in this work showed that relative scaling bias of gap probability increases with decreasing spatial resolution for most of land cover types. Large relative biases were found for most of crops sites and a mixed forest site due to their relative large variance of LAI, while very small biases occurred over grassland and shrubs sites. As for a new parameter $\hat{C}$, it varied slowly in the pure forest, grassland and shrubs sites, while more significantly in crops and mixed forest. The parameters $\hat{C}$ has endowed a new significance to traditional clumping index and provided evidence to the utility of clumping index as an improvement of the estimate of gap probability from LAI. The results exhibited also the capability of clumping index for scaling Beer' law and representing spatial heterogeneity, as well as the feasibility of the inversion approach for gap probability from remote sensing data. Meanwhile a simple and feasible method to estimate "clumping index" from remote sensing data was also explored in this work, which would provide a support to global mapping of the vegetation clumping index.

In terms of the estimation of regional ET from fully remote sensing data, this work was a trial to develop a parameterization of regional ET with only satellite derived surface parameters, such as the so-called Ts-VI triangle method. This type of method relies on the triangular shape formed by the scatter plot of surface temperature (Ts) versus vegetation index (VI) under a full range of vegetation cover and soil moisture availability within the interesting study region to estimate EF and ET at satellite pixel scale. This algorithm can provide an estimation of surface net radiation, soil heat flux, EF and ET at regional scale from MODIS data and products alone. The success of Ts-VI triangle method on the estimation of EF and ET depends mainly on the correct choice of the dry and wet edges in the Ts-VI triangle space. An arid and semi-arid area is usually selected to estimate the ET with Ts-VI triangle method because the dry edge of Ts-VI triangle feature space can be successfully determined in such areas where wet pixels are not generally easily identified. The wet edge is assumed to be a horizontal straight line in this work. By means of formula derivation, the estimation of ET can be converted into the estimation of Φ which represents a combined-effect parameter accounting for aerodynamic resistance. Once the two edges (dry and wet) in the Ts-Fr space are determined, the value of Φ corresponding to the driest bare soil pixel (at the position Fr=0 and maximum surface temperature $T_{s,max}$ in the dry edge line) is set to 0 (denoted as $\Phi_{min}=0$ at pixel (Fr=0, $T_{s,max}$)) and the value of Φ at the position Fr=1 and the minimum surface temperature $T_{s,min}$ in the dry edge line is set to 1.26 (denoted as $\Phi_{max}=1.26$ at (Fr=1, $T_{s,min}$)). A two-step linear interpolation is then used to get the Φ value for the pixel *i* ($Fr_{,i}$,$T_{s,i}$) in the Ts-Fr triangle space.

This work gave a preliminary validation of satellite derived sensible heat flux with the field measurements made by the LAS during the Heihe Field Experiment from May 20th to August 21st, 2008. The sensible heat fluxes retrieved using MODIS data from a grassland located in the middle reach of Heihe river basin, Northwest China, are in good agreement with those measured from LAS. The Root Mean Square Error of this comparison is 25.07 W/m^2. It is shown that determination of dry and wet edges using the proposed algorithm is accurate enough at least in most cases of our study for the estimates of regional surface ET. This work also showed the advantage of the Ts-VI triangle method compared to the other methods traditionally employed for the determination of the regional ET and proposed methods to calculate land surface temperature and emissivity from the radiances measured by the satellites. This work also showed that only from the satellite data with an acceptable precision it was possible to estimate ET in arid and semi-arid areas.

This work opens interesting prospects. In the restitution of regional ET, the exactitude of this restitution depends mainly on the exactitude of the dry and wet edges determination in the Ts-VI triangle and on the performance of the interpolation model involved in the evaluation of the evaporative fraction in the ET estimation model. The performances of the model and the new algorithm developed in this study have to be evaluated in the future in a precise and attentive way. Determination of dry and wet wedges in Ts-VI triangle space generally involves a large degree of subjectivity and uncertainty. The rules and algorithm proposed in this thesis give a feasible way to estimate the highest surface temperature at each fractional cover interval and subsequently determine the dry and wet edges in arid and semi-arid climate region from the Ts-VI triangle space.

Although assumption of two-step linear interpolation scheme involved in the estimation of the combined-effect parameter Φ and evaporative fraction is still questionable and not yet verified directly, a very good agreement is found when sensible heat flux estimated from MODIS data is compared with that measured by LAS instrument. To reduce the uncertainty in the estimation of turbulent heat fluxes from the Ts-VI method, further work needs to be carried out to verify the relevant parameters/variables step by step provided that data required are available in the future and more validation work needs to be performed in other different regions for the proposed algorithm.

6.2 Future trends and prospects

From what was mentioned previously, if there are no innovated methods in acquisition of remotely sensed data and meteorological variables or newly-developed ET models, the main restricting factors in the estimates of actual instantaneous/daily/weekly/monthly ET over regional scale from remote sensing techniques are actually the retrieval accuracy and physical interpretation of different surface variables retrieved from satellite data, parameterization of land surface fluxes at regional scale, temporal and spatial data/model scaling among different scales, validation of the latent heat flux obtained from models at regional scale, acquisition of near-surface meteorological data over different satellite pixel scales etc.

As known, the sensors onboard satellites measure only radiances at the top of the atmosphere. These measured radiances are in general the quantities integrated over very heterogeneous and large surfaces. One can thus ask following questions: Can one extract from these radiances the macroscopic parameters (variables) describing such a surface? Do such macroscopic parameters exist? How to define them? One can also wonder whether the description of the physical processes at the land/atmosphere interface developed at local scale is applicable to the larger (spatial) scale with surface parameters (variables) integrated over this surface. The attempts to answer all these questions lead to study the fundamental and conceptual aspects of the definition of the macroscopic parameters (variables) and the scaling effects. The passage of the radiances measured at the top of the atmosphere to the macroscopic parameters (variables) and physics of surfaces requires the corrections for the atmospheric effects and the connection of the surface parameters (variables) derived directly from satellite data to other surface parameters (variables) through physical models. These problems lead to study the methodological aspects of the derivation of the surface parameters (variables) which can not be retrieved directly from satellite data and the metrology aspects of the atmospheric corrections necessary to the determination of other surface parameters (variables) directly from satellite data.

Study will be recommended to focus on the following subjects in the future for quantifying regional and global ET.

6.2.1 Modeling of land surface processes at interface of soil-biosphere-atmosphere at regional scale

This modeling aims to formulate the processes of exchanges between soil-biosphere-atmosphere in terms of macroscopic parameters which have significant physical meaning at regional scale and are measurable from satellites. The required formulation should permit to specify both the physical meaning of the measurements by satellite and the passage of local scale to regional and global scales. It concerns a semi-phenomenological analysis which could lead to a new method to assimilate effectively satellite data for the land surfaces.

6.2.1.1 Dialectical approach to model the spatial-temporal variations of land surface processes at various scales

Two modeling methods (one is based on the other) are possible to be developed to study what occurs at regional and global scales.

6.2.1.1.1 Integrating method

This method consists in describing all the elements that compose a pixel, in modeling the processes for each one of these elements and extrapolating these models by a process of “surface integration” to deduce what occurs to large scales. It is about a type of up-scaling. Because of the non-linearity of the processes, this integration is complex and is based on assumptions not always easy to control. This method is very useful to understand what occurs, and can direct the research of the “integrating” variables (parameters) directly describing the processes at the scale considered. It is, however, difficult with this method:

1) to benefit from “simplifications” which must appear at large scale, due to the fact that one cannot measure all the characteristics of the elements composed the pixel.

2) to highlight “the good” variables representative of the system at large scales.

This method can lead to models having a very great number of parameters and variables whose determination at large scales is not possible without arbitrary, taking into account the extreme local variability of these in-situ quantities.

6.2.1.1.2 “Autonomous” method at large scales

Although the integrating method is very rich and useful, it must be supplemented, in a dialectical way, by a method that analyzes and models (parameterizes) the observations made directly at satellite pixel scale. This second method is founded on the principle of “scale autonomy” which implies that the processes at a given scale can be described and understood at this scale in an autonomous way and without making reference to the phenomena and processes intervening at a lower scale, even if they are the consequence. The passage from one scale to others permits to describe the parameters and variables defined in a given scale in function of the variables and processes of under systems intervening on a lower scale.

This raises obviously the question about whether this autonomous description with large scales exists and whether necessary and sufficient measures are currently available to carry out this study. As only satellite measurements are available, the question is whether necessary and sufficient variables (parameters) can be defined with these satellite measurements to describe the state of surface and processes of the land surface at satellite pixel scale. The answer is not obvious [Morel, 1985] and is not really known. However, experiments showed that it is possible to highlight spatial indicators which are sensitive to the variations of the state of the biosphere [Rasool, 1987; Roerink and Menenti, 2000; Roerink et al., 2000b; Moody and Johnson, 2001]. It is not possible to currently give an exhaustive list of these indicators. One can nevertheless quote a certain number of it: surface temperature, temporal sums of temperature, vegetation indices, Microwave Polarization Difference Indices (MPDI), complex inertia, Albedo, precipitation indices, moisture indices, roughness indices, resistance indices and temporal sums of some of these indices, etc

It was shown that these indices are not independent and it is possible to establish laws between their variations. Indeed, recent studies seem to indicate that this method is possible and can constitute an original approach of the processes at regional scale or global scale without going into the details of the local scale. For example, it was shown that relations NDVI/Ts could be correlated with evapotranspiration resistance, with surface moisture [Nemani et al., 1993; Nemani and Running, 1989; Whitehead et al., 1986; Carlson et al., 1995b] and that the correlations albedo/Ts could provide an indicator permitting to monitor extension of the area affected by the desertification [Becker and Séguin, 1985; Séguin et al., 1987]. It was also showed that the correlations between visible reflectances and

MPDI could characterize the interannual variations of the soil surface due to the hydrous deficit [Choudhury, 1990; Choudhury, 1991]. They are yet only the preliminary studies, but they indicate nevertheless potential and very interesting research for such an “autonomous” approach.

Although still very little developed, such an “autonomous” approach is now feasible. Indeed, huge space measurements provided by the earth observation satellites are now available to scientists and the scientists begin to be able to derive an ensemble of important surface variables (parameters) and/or spatial indicators from these measurements.

6.2.1.2 Reformulation of the energy balance at large scales

Efforts will be made by introducing “integrating parameters” and a parameterization of the diurnal variation of surface temperature with a minimum number of parameters into the reformulation of the energy balance at large scales [Goettsche and Olesen, 2001] in order to use the temporal information provided by satellite data. To simulate complicated phenomena, one can try to introduce measurable parameters from space, such as a complex inertia or complex coefficients of transfer [Abdellaoui et al., 1986; Raffy and Becker, 1986] .

6.2.1.3 Phenomenological analysis of the spatial-temporal variations of the spatial indicators characterizing surface states and processes at satellite pixel scale

The suggested phenomenological analysis will be carried out to allow: 1) description of phenomenological relations between surface variables and/or spatial indicators and to reveal possibly new parameters characterizing land surface states and processes, to highlight characteristic thresholds of the release of certain phenomena (erosion, release of sandstorm, degradation etc.), 2) establishment of the laws and properties which take into account these variations, and 3) to study these laws and the stability of the processes which they describe in function of the parameters controlling these laws.

According to the above cases, this analysis could be performed using the signal processing methods for nonlinear systems, and one will focus to study the way in which the variations observed and modeled change in function of the value of the parameters controlling the equations which will be established.

6.2.1.4 Modeling and assimilation of the data

A big challenge in the development of remote sensing ET models is to develop a new fully remote sensing data-based parameterization of land surface ET with only land surface variables and parameters directly or indirectly derived from satellite data.

Associating the measurements taken from satellites with land surface models is essential to connect between measurements and models, the various surface characteristic state variables (parameters) (or other relevant parameters), the parameters of process, and the space observations. Efforts will be made to introduce modifications of the existed land surface models by assimilating satellite data and if possible by introducing a new parameterization of land surface evapotranspiration process and evaporative fraction based on the relevant parameters observed from space. This aspect is very important to correctly take into account the effects of feedback. Accordingly, it will undoubtedly be necessary to reformulate certain equations to introduce parameters directly accessible to space measurement, or to re-compute these parameters from the models.

6.2.2 Further improvement of the accuracy of land surface variables (parameters) retrieved from remotely sensed data

Land surface temperature is the direct indicator of how much energy and water could be available over the land surface and is one of the most key factors affecting the accuracy of the ET estimates. Land surface temperature along with other related remotely sensed surface variable (parameters) such as surface albedo, emissivity, NDVI, soil moisture, fractional vegetation cover and LAI in the energy balance models have significant impact on the precise partition of the four energy components in these models and consequently on the accuracy of the retrieved regional ET. Although great progress has been made nowadays to retrieve quantitatively land surface variables (parameters) from remotely sensed data, accuracy of some surface variables (parameters) required in remote sensing ET models still needs to be improved and more attention should be paid also to the physical interpretation of these surface variables (parameters) retrieved directly or indirectly from satellite data.

6.2.3 Research in-depth on the impact of the advection on regional estimates of ET

Advection is another factor influencing the accuracy of the partition of surface available energy into turbulent fluxes. It often occurs in the urban area and desert and directly causes the imbalance of surface energy especially over small spatial scales (high spatial-resolution) and is another source of energy to evaporate the water from surface. At present, it is still uncertain over what scale advection will have to be considered and how the energy is exchanged between neighboring pixels in the horizontal direction.

6.2.4 Calibration of land surface process models with the remote sensing ET to map regional and time-integrated ET

Theoretically, remote sensing ET models can be able to provide relatively accurate spatial distributions of instantaneous ET while land surface process models driven by atmospheric forcing data, and run with related surface data and physical properties of soil and vegetation as model inputs, can simulate the long-term development trend of the turbulent heat fluxes, soil water content and other related corresponding physical, chemical and biological processes that might occur over both temporal and spatial scales. Land surface process models may help to overcome the limitation of the current remote sensing ET models, the latter is merely employed under clear sky conditions and at instantaneous scale. However, because of both the low spatial resolution and the uncertainties in the model inputs in the land surface process models, it is hard, sometimes impossible to estimate correctly the latent heat flux at large scale with land surface process models without adding information provided by satellite data. Remote sensing has the unique advantages on the acquisition of spatial land surface variables (parameters) needed in the land surface process models from a scale of several meters to a scale of several kilometers. It may be an effective way to reduce the uncertainties existing in the current land surface process models. Efforts will be made therefore to develop methodologies to calibrate the ET simulated by land surface models with remote sensing ET values and use as many as possible all the land surface variables (parameters) derived from satellite data under clear sky conditions. In addition, with the rapid development of multi-spectral, multi-temporal and multi-spatial satellite technology, computer processing technique and optimization algorithms in the geosciences, data assimilation is believed to be another promising way to integrate the models, data and optimization methods together to estimate temporal and spatial ET continuously.

6.2.5 Validation of the ET and land surface variables (parameters) at satellite pixel scale

Validation is the process of assessing by independent means the uncertainty of the data products derived from the system outputs. Without validation, any methods, models, algorithms, and parameters derived from remotely sensed data can not be used in confident. Both the fundamental physical measurements made by the sensor (e.g. radiance) and the derived geophysical variables (e.g. biomass) must be properly validated. Validation is the most key and urgent issue to be dealt with because validation can help to understand the combined effects of errors in the remotely sensed data, uncertainty in the remote sensing ET models and uncertainty in the retrieved land surface variables (parameters), and thus can provide feedback and some clues to optimize models, improve accuracies of both the remotely sensed data and the retrieved land surface physical variables (parameters).

Currently, validation of estimated ET is one of the most troublesome problems mainly because of both the scaling effects, i.e., comparisons between remote sensing ET and ground-based ET measurements, and the advection effects. Several validation techniques have to be developed. These may include comparisons of remote sensing ET with ground-based ET measurements conducted over validation test sites, inter-comparisons with ET estimated from satellite data at different spatial resolution or estimated using combined various data sources and land surface process models, inter-comparison of trends derived from independently obtained reference data and remotely sensed data, and analysis of process model results which are driven or constrained by remotely sensed data and ET. However, due to the surface heterogeneity and scaling effects, it may be questionable to validate the turbulent heat fluxes at satellite pixel scale with the “point” scale measurements obtained from the Bowen ratio, lysimeter and eddy correlation system over non-uniform and heterogeneous surfaces. The newly developed LAS (XLAS) can provide a promising approach to validate the remote sensing ET at much larger scales.

Appendix

Nomenclatures and Acronyms

Nomenclatures or Acronyms	Meanings or Full Names
ABL	Atmospheric Boundary Layer
AEA	Albers Equal Area
ALEXI	Atmosphere-Land Exchange Inverse
A_p	the projection of leaf area in perpendicular to incident beam
ARM	Atmospheric Radiation Measurement
ASCE	American Society of Civil Engineers
ASL	Atmospheric Surface Layer
ASTER	Advanced Space-borne Thermal Emission and Reflection Radiometer
ATSR	Along Track Scanning Radiometer
AVHRR	Advanced Very High Resolution Radiometer
B	Planck function
BAS	Bulk Atmospheric Similarity
$B_i(T_i)$	Channel radiance measured in channel i at the TOA
$B_i(T_s)$	Radiance measured in channel i if the surface was a blackbody with surface temperature T_s
BRDF	Bidirectional Reflectance Distribution Function
BREB	Bowen Ratio Energy Balance
$\hat{C}$	Clumping index at coarse pixel
CAST	China Academy of Space Technology
CMA	China Meteorological Administration
c_p	Specific heat of air at constant pressure
C_{rad}	Correction coefficient used in sloping terrain
CWSI	Crop Water Stress Index
d	Zero plane displacement height
D_y	Day of year
D_a	Earth-sun distance in astronomical unit
DEM	Digital Elevation Model
DISALEXI	DISaggregated ALEXI
dT	Surface-air temperature difference
DTD	Dual Temperature Difference
dT_{dry}	Surface-air temperature difference at dry pixel
dTs	Surface temperature difference of two times in the morning
dT_{wet}	Surface-air temperature difference at wet pixel
E_0	Solar irradiance at TOA
EBBR	Energy Balance Bowen Ration
EC	Eddy Correlation
ECMWF	European Centre of Median-range Weather Forecast
EDAS	Eta Data Assimilation System
EDC	EROS Data Center

Nomenclatures or Acronyms	Meanings or Full Names
EF	Evaporative fraction
EF_i	Instantaneous EF
EF_r	Relative evaporative fraction
ET	EvapoTranspiration
ET_d	Cumulative daily ET
ET_i	Instantaneous ET
ET_r	Reference ET (over the standardized 0.5m tall alfalfa)
ET_{r_d}	Cumulative daily reference ET
ET_rF	Reference ET fraction
$f(\theta)$	vegetation *f*raction viewed at angle θ
FIFE	First ISLSCP Field Experiment
F_r	Fractional vegetation cover
$F_{r,i}$	Fractional vegetation cover for each VI or NDVI interval (i)
g	Acceleration due to gravity of the earth
G	Soil heat flux density
GOES	Geostationary Operational Environmental Satellites
GSFC	Goddard Space Flight Center
GSW	Generalized Split-Window
H	Sensible heat flux
H_c	Sensible heat flux for canopy
HCMM	Heat Capacity Mapping Mission
HDF	Hierarchical Data Format
H_{dry}	Sensible heat flux at dry limit
h_{pbl}	Height of the PBL
HRV	High Resolution Visible
H_s	Sensible heat flux of bare soil
H_{wet}	Sensible heat flux at wet limit
IFOV	Instantaneous Field Of-View
IGBP	International Geosphere-Biosphere Programme
IPCC	Intergovernmental Panel on Climate Change
IR	Infra-Red
ISLSCP	International Satellite Land-Surface Climatology Project
JHU	Johns Hopkins University
k	Von Karman’s constant
L	Latent heat of vaporizaiton
LAADS	Level 1 and Atmosphere Archive and Distribution System
LAI	Leaf Area Index
LAI_{pixel}	LAI at coarse pixel
$LAI^{i}_{sub-pixel}$	LAI of sub-pixel *i* within a coarse pixel

Nomenclatures or Acronyms	Meanings or Full Names
LAS	Large Aperture Scintillometer
LE	Latent heat flux density
LE_c	Canopy-covered *ET*
LE_d	Daily ET
LE_{dry}	Latent heat flux at dry limit
LE_i	Instantaneous *LE*
LE_p	Potential ET
LE_s	ET of bare soil
LE_{wet}	Latent heat flux at wet limit
LMD	Laboratoire de Meteorologie Dynamique
LPDAAC	Land Processes Distributed Active Archive Center
LSE	Land Surface Emissivity
LST	Land Surface Temperature
MCST	MODIS Characterization and Support Team
ME	Mean Error
METRIC	Mapping EvapoTranspiration at high Resolution with Internalized Calibration
MIR	Middle InfreRed
MISR	Multi-angle Imaging Spectra-Radiometer
MODAPS	MODIS Adaptive Processing System
MODIS	MODerate resolution Imaging Spectroradiometer
MODTRAN	MODerate spectral resolution atmospheric TRANsmittance algorithm and computer model
MRT	MODIS Reprojection Tool
MSG/SEVIRI	Meteosat Second Generation/Spinning Enhanced Visible and Infrared Imager
NASA	National Aeronautics and Space Administration
$NDVI$	Normalized Difference Vegetation Index
$NDVI_{max}$	Maximum Normalized Difference Vegetation Index
$NDVI_{min}$	Minimum Normalized Difference Vegetation Index
$NE\Delta T$	Noise Equivalent Temperature Difference
NIR	Near Infrared
NOAA	National Oceanic and Atmospheric Administration
NWP	Numerical Weather Prediction
P	Directional gap probability
PBL	Planetary Boundary Layer
POLDER	Polarization and Directionality of Earth Reflectance
r	Broadband albedo at TOA
r_a	Aerodynamic resistance to heat transfer between surface and reference height
$r_{a,max}$	Maximum aerodynamic resistance to sensible heat transfer
$r_{a,min}$	Minimum aerodynamic resistance to sensible heat transfer

Nomenclatures or Acronyms	Meanings or Full Names
r_c	Canopy-covered aerodynamic resistance to sensible heat transfer
RE	Relative Error
R_{lw}	Surface net longwave radiation
RMSE	Root Mean Square Error
R_n	Surface net radiation flux density
R_{nd}	Daily R_n
r_s	Aerodynamic resistance of bare soil to sensible heat transfer
R_s	Incoming shortwave solar radiation
$R_{s,d}$	Cumulative daily R_s
$R_{s,d,horizontal}$	Cumulative daily R_s for a horizontal surface
$R_{s,d,pixel}$	Cumulative daily R_s for a specific pixel
$R_{s,i}$	Instantaneous R_s
$R_{s,i,horizontal}$	Instantaneous R_s for a horizontal surface
$R_{s,i,pixel}$	Instantaneous R_s for a specific pixel
R_{sw}	Surface net shortwave radiation
S	Area of pixel
SAST	Shanghai Academy of Space Flight Technology
SAVI	Soil-Adjusted Vegetation Index
SEBAL	Surface Energy Balance Algorithm for Land
SEBI	Surface Energy Balance Index
SEBS	Surface Energy Balance System
SEVIRI	Spinning Enhanced Visible and Infrared Imager
SGP	Southern Great Plain
s_i	Area of sub-pixel i
SPOT	Systeme Probatoire d'Observation dela Tarre
S-SEBI	Simplified Surface Energy Balance Index
SVAT	Soil-Vegetation-Atmosphere Transfer
S-VISSR	Stretched-Visible and Infrared Spin-Scan Radiometer
SZA	Solar Zenith Angle
t	Duration time starting at sunrise
T_0	Surface temperature of bare soil
T_a	Air temperature measured at a reference height
T_{a_1st}	Atmospheric temperature in the first boundary layer of the atmospheric profiles used
T_{aero}	Aerodynamic temperature
$T_B(\theta)$	Brightness temperature viewed at angle θ
T_c	Canopy radiometric temperature
T_g^0	MIR ground brightness temperature without the contribution of the solar direct beam
T_{g_22}	Daytime ground brightness temperature of MODIS channel 22
T_{g_23}	Daytime ground brightness temperature of MODIS channel 23

Nomenclatures or Acronyms	Meanings or Full Names
T_i	Channel brightness temperature observed in channel *i* at the TOA
$\overline{T_i}$	Mean channel brightness temperature of pixels observed in channel *i* at the TOA
TIGR	Thermodynamic Initial Guess Retrieval
TIR	Thermal InfreRed
TIROS-N	Television Infrared Observation Satellite - N series
T_j	Channel brightness temperature observed in channel *j* at the TOA
$\overline{T_j}$	Mean channel brightness temperature of pixels observed in channel *j* at the TOA
TM	Thematic Mapper
TOA	Top Of the Atmosphere
T_{pbl}	Average planetary boundary layer temperature
$T_{RAD}(\theta)$	Directional radiometric surface temperature viewed at angle θ
T_s	Surface radiometric temperature
$T_{s,i}$	Surface radiometric temperature for each VI or NDVI interval (*i*)
$T_{s,max}$	Maximum surface temperature
$T_{s,max,i}$	Maximum surface temperature for each VI or NDVI interval (*i*)
$T_{s,min}$	Minimum surface temperature
$T_{s,mix,i}$	Minimum surface temperature for each VI or NDVI interval (*i*)
T_{SKY}	Air temperature or equivalent air temperature
TSM	Two-Source (soil+canopy) Model
TSTIM	Two-Source Time Integrated Model
u	Wind speed
u^*	Friction velocity
UCSB	University of California Santa Barbara
UNEP	United Nations Environment Program
VALERI	Validation of Land European Remote sensing Instruments
VI	Vegetation Index
VIT	Vegetation Index/Temperature
VPD	Vapor Pressure Deficit
VZA	Viewing Zenith Angle
WDI	Water Deficit Index
WMO	the World Meteorological Organization
WVC	Water Vapor Content
XLAS	eXtra-Large Aperture Scintillometers
z_a	Measurement height of wind speed and air temperature
z_{oh}	Surface roughness length for heat transfer
z_{om}	Surface roughness length for momentum transfer
α_s	Surface shortwave albedo
β	Bowen ratio

Nomenclatures or Acronyms	Meanings or Full Names
γ	Psychrometric constant
Δ	Slope of saturated vapor pressure as a function of Ta
δ	Standard deviation
δ_{LAI}	Standard deviation of LAI
δLST	LST error
$\Delta\varepsilon$	Difference between ε_i and ε_j
ε	Emissivity
$\varepsilon(\theta)$	Surface emissivity viewed at angle θ
ε_a	Atmospheric emissivity
ε_i	Channel emissivity in channel *i*
ε_j	Channel emissivity in channel *j*
ε_s	Surface emissivity
θ	Viewing angle
θ_i	Incident radiation angle
θ_z	Solar zenith angle
$\overline{\theta}_L$	Mean of leaf inclination angle
λ	Geographical latitude (expressed in decimal degrees)
Λ	Monin-Obukhov length
μ	Cosine of solar zenith angle
ξ	Phase angle
ρ	Density of a certain entity
ρ_b	Bidirectional reflectivity
$\rho_h(\theta)$	Hemispherical directional reflectance at viewing angle θ
$\rho_h(\theta_{VZA})$	Hemispherical directional reflectance at viewing zenith angle θ
ρ_i	Narrowband reflectance at the TOA
ρ_w	Density of water
σ	Stefan-Boltzman constant (5.67×10^{-8})
τ_i	Atmospheric transmittance in channel *i*
τ_j	Atmospheric transmittance in channel *j*
Φ	Combined-effects parameter which accounts for aerodynamic resistance
Φ_i	Φ for each VI or NDVI interval (*i*)
Φ_{max}	Maximum Φ
$\Phi_{max,i}$	Maximum Φ for each VI or NDVI interval (*i*)
Φ_{min}	Minimum Φ
$\Phi_{min,i}$	Minimum Φ for each VI or NDVI interval (*i*)
φ	Relative azimuth angle between the observation and incident directions
Ψ_1	Stability correction function for momentum transfer
Ψ_2	Stability correction function for heat transfer
Ω	Clumping index

Nomenclatures or Acronyms	Meanings or Full Names
Γ	Ratio of G to R_n
Γ_s	Γ of bare soil
Γ_v	Γ of full vegetation cover

References

Abdellaoui, A . ; Becker, F.; Olory-Hechinger, E. (1986). Use of Meteosat for mapping thermal inertia and evapotranspiration over a limited region of Mali. *J. Appl. Meteorol. 25*, 1489-1506.

Allen, R.G.; Morse A.; Tasumi, M.; Bastiaanssen, W.; Kramber, W.; Anderson, H. (2001). Evapotranspiration from Landsat (SEBAL) for water rights managementand compliance with multi-state water compacts. IGARSS. 2, 830-833.

Allen, R.G.; Tasumi, M.; Morse, A. (2005a). Satellite-based evapotranspiration by METRIC and Landsat for western states water management. Presented at the US Bureau of Reclamation Evapotranspiration Workshop, Ft. Collins, CO, USA, Feb. 2005.

Allen, R.G.; Tasumi, M.; Trezza, R. (2005b). METRIC: mapping evapotranspiration at high resolution—applications manual for Landsat satellite imagery. *University of Idaho*, Kimberly.

Allen, R.G.; Tasumi, M.; Trezza, R. (2007). Satellite-based energy balance for mapping evapotranspiration with internalized calibration (METRIC)-model. *J. Irrig. Drain. E. 133*, 380-394.

Anderson, J.L. (2001). An ensemble adjustment Kalman filter for data assimilation. *Mon. Wea. Rev. 129*, 2884-2903.

Anderson, M.C.; Norman, J.M.; Diak, G.R.; Kustas, W.P.; Mecikalski, J.R. (1997). A two-source time-integrated model for estimating surface fluxes using thermal infrared remote sensing. *Remote Sens. Environ. 60,* 195-216.

Anderson, M.C.; Norman, J.M.; Kustas, W.P.; Li, F.; Prueger, J.H.; Mecikalski, J.R. (2005). Effects of vegetation clumping on two-source model estimates of surface energy fluxes from an agricultural landscape during SMACEX. *J. Hydrometeor. 6*, 892−909.

Anderson, M.C.; Norman, J.M.; Mecikalski, J.R.; Torn, R.D.; Kustas, W.P.; Basara, J.B. (2004). A multi-scale remote sensing model for disaggregating regional fluxes to micrometeorological scales. *J. Hydrometeor. 5*, 343-363.

Angus, D.E.; Watts, P.J. (1984). Evapotranspiration — How good is the Bowen ratio method? *Agric. Water Manage. 8*, 133-150.

Asanuma, J.; Iemoto, K. (2007). Measurements of regional sensible heat flux over Mongolian grassland using large aperture scintillometer. *J. Hydrol., 333*, 58-67.

Baret, F.; Weiss, M.; Allard, D.; Garrigues, S.; Leroy, M.; Jeanjean, H.; Fernandes, R.; Myneni, R.; Morissette, J.; Privette, J.; Bohbot, H.; Bosseno, R.;Dedieu, G.; Bella, C.D.; Espana, M.; Gond, V.; Gu, X.; Guyon, D.; Lelong,C.; Maisongrande, P.; Mougin, E.; Nilson, T.; Veroustraete, F.; Vintilla, R. in press. Valeri: a network of sites and a methodology for the validation of medium spatial resolution land satellite product. Remote Sens. of Environ. (in press)

Bastiaanssen, W.G.M. (1995). Regionalization of surface flux densities and moisture indicators in composite terrain. Ph.D. Thesis，*Wageningen Agricultural University*. Wageningen. The Netherlands. 1995.

Bastiaanssen, W.G.M. (2000). SEBAL-based sensible and latent heat fluxes in the irrigated Gediz Basin, Turkey. *J. Hydrol.229*, 87-100.

Bastiaanssen, W.G.M.; Menenti, M.; Feddes, R.A.; Holtslag, A.A.M. (1998). A remote sensing surface energy balance algorithm for land (SEBAL): 1.Formulation. *J. Hydrol. 212-213*, 198-212.

Bastiaanssen, W.G.M.; Noordman, E.J.M.; Pelgrum, H.; Davids, G.; Thoreson, B.P.; Allen, R.G. (2005). SEBAL model with remotely sensed data to improve water-resources management under actual field conditions. *ASCE J. Irrig. Drain. E. 131*, 85–93.

Bastiaanssen, W.G.M.; Pelgrum, H.; Wang, J.; Ma, Y.; Moreno, J.F.; Roerink, G.J.; van der, W.T. (1998). A Surface Energy Balance Algorithm for Land (SEBAL): Part 2 validation. *J. Hydrol. 212-213*, 213-229.

Bates, B.C., Kundzewicz, Z.W., Wu, S., Palutikof, J.P., Eds. (2008). *Climate change and water. technical paper of the intergovernmental panel on climate change*. IPCC Secretariat, Geneva, Switzerland.

Batra, N.; Islam, S.; Venturini, V.; Bisht, G.; Jiang, L. (2006). Estimation and comparison of evapotranspiration from MODIS and AVHRR sensors for clear sky days over the Southern Great Plains. *Remote Sens. Environ. 103*, 1-15.

Becker, F.; Li, Z.-L. (1990). Toward a local split window method over land surface. *Int. J.Remote Sens.*.3, 369-393.

Becker, F.; Li, Z.-L. (1995). Surface temperature and emissivity at various scales: Definition, measurement and related problems. *Remote Sen. Environ.* 12, 225-253.

Becker, F.; Séguin, B. (1985). Determination of surface parameters and fluxes for climate studies from space observation. Methods, Results and Problems. *Adv. Space Res. 5*, 299-317.

Berk, A.; Bernstein, L.S.; Anderson, G.P.; Acharya, P.K.; Robertson, D.C.; Chetwynd, J.H.; et al. (1998). MODTRAN cloud and multiple scattering upgrades with application to AVHRIS. *Remote Sen. Environ.* 65, 367-375.

Bisht, G.; Venturini, V.; Islam, S.; Jiang, L. (2005). Estimation of the net radiation using MODIS (Moderate Resolution Imaging Spectroradiometer) data for clear sky days. *Remote Sens. Environ. 97*, 52 – 67.

Blad, B.L.; Rosenberg. N.J. (1974). Lysirmetric calibration of the Bowen ratio-energy balance method for evapotranspiration estimation in the Central Great Plains. *J. Appl. Meteorol. 13*, 227-236.

Blad, B.L.; Rosenberg, N.J. (1976). Measurement of crop temperature by leaf thermocouple, infrared thermometry and remotely sensed thermal imagery. *Agron J. 68*, 635-641.

Boni, G.; Entekhabi, D.; Castelli, F. (2001). Land data assimilation with satellite measurements for the estimation of surface energy balance components and surface control on evaporation. *Water Resour. Res. 37*, 1713-1722.

Bouttier, F.; Courtier, P. (1999). Data assimilation concepts and methods. Presented at the Meteorological Training Course Lecture Series. European Centre for Medium-Range Weather Forecasts, Reading, England, pp.1-58.

Brown, K.W.; Rosenberg, N.J. (1973). A resistance model to predict evapotranspiration and its application to a sugar beet field. *Agron. J. 65*, 199-209.

Brutsaert, W. (1986). Catchment-scale evaporation and the atmospheric boundary layer. *Water Resour. Res. 22*, 39-45.

Brutsaert, W. (1999). Aspect of bulk atmospheric boundary layer similarity under free-convective conditions. *Rev Geophys. 37*, 439–451.

Brutsaert, W.H. (1975). On a derivable formula for long-wave radiation from clear skies. *Water Resour. Res. 11*, 742–744.

Brutsaert, W.H. (1982). *Evaporation into the Atmosphere*. D. Reidel, London.

Businger, J.A.; Wyngaard, J.C.; Izumi, Y.; Bradley, E.F. (1971). Flux-Profile relationships in the atmospheric surface layer. *J. Atmos. Sci. 28*, 181-189.

Bussieres, No.; Louie, P.Y.T.; Hogg, W. (1990). Progress report on the implementation of an algorithm to estimate regional evaportanspiration using satellite data. Proceeding of the workshop on applications of remote sensing in hydrology, Saskaton Saskatchewan, 13-14 February 1990.

Campbell, G.S.; Norman, J.M. (1998). An introduction to environmental biophysics. 2nd ed. Ann Arbor, Mich., Edwards Brothers.

Caparrini, F.; Castelli, F. (2004). Variational estimation of soil and vegetation turbulent transfer and heat flux parameters from sequences of multisensor imagery. *Water Resour. Res. 40*, W12515 1-15,

Caparrini, F.; Castelli, F.; Entekhabi, D. (2003). Mapping of land–atmosphere heat fluxes and surface parameters with remote sensing data. *J. Hydrometeor. 5*, 145−159.

Caparrini, F.; Castelli, F.; Entekhabi, D. (2004). Estimation of surface turbulent fluxes through assimilation of radiometric surface temperature Sequences. *J. Hydrometeoro. 5*, 145-159.

Carlson, T. (2007). An overview of the "Triangle Method" for estimating surface evapotranspiration and soil moisture from satellite imagery. *Sensors. 7*, 1612-1629.

Carlson, T.; Ripley, D. (1997). On the relation between NDVI, fractional vegetation cover, and leaf area index. *Remote Sens. Environ*, *62*, 241-252.

Carlson, T.N.; Buffum, M.J. (1989). On estimating daily evapotranspiration from remote surface temperature measurements. *Remote Sens. Environ. 29*, 197-207.

Carlson, T.N.; Capehart, W.J.; Gillies, R.R. (1995a). A new look at the simplified method for remote sensing of daily evapotranspiration. *Remote Sens. Environ. 54*, 161-167.

Carlson, T.N.; Dodd, J.K.; Benjamin, S.G.; Cooper, J.N. (1981). Satellite estimation of the surface energy balance, moisture availability and thermal inertia. *Bull. Am. Meteorol. Soc.* January, 67-87.

Carlson, T.N.; Gillies, R.R.; Pery, E.M. (1995b). A method to make use of thermal infrared temperature and NDVI measurements to infer surface soil water content and fractional vegetation cover, *Remote Sens. Rev. 9*, 167-173.

Carlson, T.N.; Perry, E.M.; Schmugge, T.J. (1990). Remote estimation of soil moisture availability and fractional vegetation cover for agricultural fields. *Agric. For. Meteorol. 52*, 45-69.

Caselles, V.; Sobrino, J.A.; Coll, C. (1992). On the use of satellite thermal data for determining evapotranspiration in partially vegetated areas. *Int. J. Remote Sens. 13*, 2669-2682.

Chen, J.M. (1996). Canopy architecture and remote sensing of the fraction of photonsynthetically active radiation absorbed by boreal conifer forests. *IEEE Trans. Geosci. Remote Sens, 34*, 1353-1368.

Chen, J.M. (1999). Spatial scaling of a remotely sensed surface parameter by contexture. *Remote Sens. Environ. 69*, 30-42.

Chen, J.M.; Menges, C.H.; Leblanc, S.G. (2005). Global mapping of the foliage clumping index using multi-angular satellite data. *Remote Sens. Environ. 97* (4), 447-457.

Chen, J.M.; Pavlic, G.; Brown, L.; Cihlar, J.; Leblanc, S.G.; White, H.P.; Hall, R.J.; Peddle; D.; King, D.J.; Trofymow, J.A.; Swift, E.; Van der Sanden, J.; Pellikka, P. (2002). Derivation and validation of Canada-wide coarse resolution leaf area index maps using high resolution satellite imagery and ground measurements. *Remote Sens. Environ. 80*, 165-184.

Chen, Y.H.; Li, X.; Li, J.; Shi, P.; Dou, W. (2005). Estimation of daily evapotranspiration using a two-layer remote sensing model. *Int. J. Remote Sens. 26*, 1755–1762.

Choudhury, B.J. (1990). A comparative analysis of satellite-observed visible reflectance and 37 GHz polarization difference to assess land surface change over the Sahel zone, 1982-1986. *Climatic Change*. *17*, 193-208.

Choudhury, B.J. (1989). Estimating evaporation and carbon assimilation using infrared temperature data: vistas in modeling. In *Theory and applications of optical remote sensing*; Asrar, G., Ed; John Wiley and Sons: New York, USA, 1989; pp. 628–690.

Choudhury, B.J.; Reginato, R.J.; Idso, S.B. (1986). An analysis of infrared temperature observations over wheat and calculation of latent heat flux. *Agric. For. Meteorol. 37*, 75-88.

Choudhury, B.J. (1994). Synergism of multi-spectral satellite observations for estimating regional land surface evaporation. *Remote Sens. Environ. 49*, 264-274.

Choudhury, B.J. (1991). Synergistic use of visible, infrared and microwave observations for monitoring land surface change. In 5ème colloque International Mesures Physiques et Signatures en Télédétection, Courchevel, France, pp. 469-473.

Colaizzi, P.D.; Evett, S.R.; Howell, T.A.; Tolk, J.A. (2006). Comparison of five models to scale daily evapotranspiration from one-time-of-day measurements. *Trans. ASAE. 49*, 1409−1417.

Coll C.; Caselles, V. (1997). A split-window algorithm for land surface temperature from advanced very high resolution radiometer data: Validation and algorithm comparison. *J. Geophys. Res. Atmos.*, 102(D14), 16697-16713.

Courault, D.; Seguin, B.; Olioso, A. (2003). Review to estimate evapotranspiration from remote sensing data: some examples from the simplified relationship to the use of mesoscale atmospheric models. ICID workshop on remote sensing of ET for large regions, Montpellier, France, Sept. 2003; pp. 1-17.

Courault, D.; Seguin, B.; Olioso, A. (2005). Review on estimation of evapotranspiration from remote sensing data: From empirical to numerical modeling approaches. *Irrig. Drainage Sys.*, 19, 223-249.

Courtier, P.; Andersson, E.; Heckley, W.; Pailleux, J.; Vasiljevic, D.; Hamrud, M.; Hollingsworth, A.; Rabier, F.; Fisher, M. (1998). The ECMWF implementation of three-dimensional variational assimilation (3D-Var). I: Formulation. *Q. J. Roy. Meteorol. Soc. 124*, 1783-1807.

Crago, R.D. (1996). Conservation and variability of the evaporative fraction during the daytime. *J. Hydrol. 180*, 173–194.

Crago, R. D.; Brutsaert, W. (1992). A comparison of several evaporation equations. *Water Resour. Res*. 28, 951-954.

Crow, W.T.; Kustas, W.P. (2005). Utility of assimilating surface radiometric temperature observations for evaporative fraction and heat transfer coefficient retrieval. *Boundary-Layer Meteorol. 115*, 105–130.

Daughtry, C.S.T.; Kustas, W.P.; Moran, M.S.; Pinter, P.J.JR.; Jackson, R.D.; Brown, P.W.; Nichols, W.D.; Gay, L.W. (1990). Spectral estimates soil heat flux of net radiation and soil heat flux. *Remote Sens. Environ*. *32*, 111-124.

Diak, G.R. (1990). Evaluation of heat flux, moisture flux and aerodynamic roughness at the land surface from knowledge of the PBL height and satellite-derived skin temperatures. *Agric. For. Meteorol. 52*, 181-198.

Diak, G.R.; Rabin, R.M.; Gallo, K.P.; Neale, C.M. (1995). Regional-scale comparisons of NDVI, soil moisture indices from surface and microwave data and surface energy budgets evaluated from satellite and in-situ data. *Remote Sens. Rev. 12*, 355-382.

Engman, E.T.; Gurney, R.J. (1991). *Remote Sensing in Hydrology*. Chapman and Hall, London, UK.

Farah, H.O.; Bastiaanssen, W.G.M.; Feddes, R.A. (2004). Evaluation of the temporal variability of the evaporative fraction in a tropical watershed. *Int. J. Appl. Earth Obs. Geoinform. 5*, 129-140.

Farahani, H.J.; Howell, T.A.; Shuttleworth, W.J.; Bausch, W.C. (2007). Evapotranspiration: progress in measurement and modeling in agriculture. *Trans. ASABE*. *50*, 1627-1638.

Fernandes, R.; Butson, C.; Leblanc, S.; Latifovic, R. (2003). Landsat-5 TM and Landsat-7 ETM+ based accuracy assessment of leaf area index products for Canada derived from SPOT-4 VEGETATION data. *Can. J. Remote Sens, 29* (2), 241-258.

Francois, C. (2002). The potential of directional radiometric temperatures for monitoring soil and leaf temperature and soil moisture status. *Remote Sens. Environ, 80*, 122-133.

Francois, C.; Ottle, C.; Prevot, L. (1997). Analytical parameterization of canopy directional emissivity and directional radiance in thermal infrared. Application on the retrieval of soil and foliage temperatures using two directional measurements. *Int. J. Remote Sens, 18* (12), 2587-2612.

Franks, S.W.; Beven, K.J. (1997). Estimation of evapotranspiration at the landscape scale: a fuzzy disaggregation approach. *Water Resour. Res. 33*, 2929-2938.

Friedl, M.A.; Davis, F.W.; Michaelsen, J.; Moritz, M.A. (1995). Scaling and uncertainty in the relationship between the NDVI and land surface biophysical variables: An analysis using a scene simulation model and data from FIFE. *Remote Sens. Environ, 54*, 233-246.

Fuchs, M.; Asrar, G.; Kanemasu, E.; Hipps, L. (1984). Leaf area estimates from measurements of photosynthetically active radiation in wheat canopies. *Agric. For. Meteorol, 32*, 13-22.

Gao, W.; Coulter, R.L.; Lesht, B.M.; Qiu, J.; Wesely, M.L. (1998). Estimating clear-sky regional surface fluxes in the Southern Great Plains atmospheric radiation measurement site with ground measurements and satellite observations. *J. Appl. Meteorol. 37*, 5-22.

Garratt, J.H.; Hicks, B.B. (1973). Momentum, heat and water vapor transfer to and from natural surfaces. *Q. J. Roy. Meteorol. Soc. 99*, 680-687.

Garrigues, S.; Allard, D.; Baret, F.; Weiss, M. (2006a). Quantifying spatial heterogeneity at the landscape scale using variogram models. *Remote Sens. Environ, 103*, 81-96.

Garrigues, S.; Allard, D.; Baret, F.; Weiss, F. (2006b). Influence of the spatial heterogeneity on the non-linear estimation of Leaf Area Index from moderate resolution remote sensing data. *Remote Sens. Environ, 105* (4): 286-298.

Gillies, R.R.; Carlson, T.N. (1995). Thermal remote sensing of surface soil water content with partial vegetation cover for incorporation into mesoscale prediction models. *J. Appl. Meteorol. 34*, 745-756.

Glenn, E. P.; Huete, A. R.; Nagler, P. L.; Hirschboeck, K. K.; Brown, P. (2007). Integrating remote sensing and ground methods to estimate evapotranspiration. *Crit. Rev. Plant Sci. 26*, 139-168.

Goettsche, F.M.; Olesen F.S. (2001). Modelling of diurnal cycles of brightness temperature extracted from METEOSAT data. *Remote Sens. Environ. 7*6, 337-348.

Goward, S.; Cruickshanks, G.D.; Hope, A. (1985). Observed relation between thermal emission and reflected spectral radiance of a complex vegetated landscape. *Remote Sens. Environ. 18*, 137-146.

Gowda, P.H.; Chavez, J.L.; Colaizzi, P.D.; Evett, S.R.; Howell, T.A.; Tolk, J.A. (2007). ET mapping for agricultural water management: present status and challenges. *Irrig. Sci. 26*, 223-237.

Gurney, R.J.; Camillo, P.J. (1984). Modelling daily evapotranspiration using remotely sensed data. *J. Hydrol. 69*, 305-324.

Hall, F.G.; Huemmrich, K.F.; Geotz, S.J.; Sellers, P.J.; Nickerson, J.E. (1992). Satellite remote sensing of surface energy balance: success, failures and unresolved issues in FIFE. *J. Geophys. Res. 97*, 19061-19090.

Hatfield, J.L. (1983) Evapotranspiration Obtained from Remote Sensing Methods. *Adv. Irrig.* **1983**, *2*, 395-416.

Hatfield, J.L.; Perrier, A.; Jackson, R.D. (1983). Estimation of evapotranspiration at one time-of-day using remotely sensed surface temperatures. *Agri. Water Manage.* **1983**, *7*, 341-350.

Hemakumara, H.M.; Chandrapala, L.; Arnold, M.F. (2003). Evapotranspiration fluxes over mixed vegetation areas measured from large aperture scintillometer. *Agric. Water Manage. 58*, 109-122.

Hoedjes, J.C.B.; Chehbouni, A.; Ezzahar, J.; Escadafal, R.; De Bruin, H.A.R. (2007). Comparison of large aperture scintillometer and eddy covariance measurements: Can thermal infrared data be used to capture footprint-induced differences? *J. Hydrometeor. 8*, 144–159.

Hoedjesa, J.C.B.; Chehbounia, A.; Jacobb, F.; Ezzaharc, J.; Bouleta, G. (2008). Deriving daily evapotranspiration from remotely sensed instantaneous evaporative fraction over olive orchard in semi-arid Morocco. *J. Hydrol. 354*, 53-64

Hoedjes, J.C.B.; Zuurbier, R.M.; Watts, C.J. (2002). Large aperture scintillometer used over a homogeneous irrigated area, partly affected by regional advection. *Boundary-Layer Meteorol. 105*, 99-117.

Hope, A.S. (1988). Estimation of wheat canopy resistance using combined remotely sensed spectral reflectance and thermal observations. *Remote Sens. Environ. 24*, 369-383.

Huang, C.; Li, X.; Lu, L.; Gu, J. (2008). Experiments of one-dimensional soil moisture assimilation system based on ensemble Kalman filter. *Remote Sens. Environ. 112*, 888-900.

Idso, S.B.; Jackson, R.D.; Reginato, R.J. (1975a). Detection of soil moisture by remote surveillance. *Amer. Sci. 63*, 549-557.

Idso, S.B.; Jackson, R.D.; Reginato, R.J. (1975b). Estimating evaporation: a technique adaptable to remote sensing. *Science 189*, 991-992.

Idso, S.B.; Jackson, R.D.; Pinter, P.J.Jr.; Reginato, R.J.; Hatfield, J.L. (1981). Normalizing the stress-degree-day parameter or environmental variability, *Agric. Meteorol. 24,* 24-45.

Idso, S.B.; Reginato, R.J.; Jackson, R.D. (1977). An equation for potential evaporation from soil, water, and crop surfaces adaptable to use by remote sensing. *Geophys. Res. Lett. 4*, 187-188.

Idso, S.B.; Schmugge, T.J.; Jackson, R.D.; Reginato, R.J. (1975c). The utility of surface temperature measurements for the remote sensing of surface soil water status. *J. Geophys. Res. 80*, 3044-3049.

Jackson, R.D. (1985). Evaluating evapotranspiration at local and regional scales. *Proc. IEEE.* **1985**, *73*, 1086-1096.

Jackson, R.D.; Hatfield, J.L.; Reginato, R.J.; Idso, S.B.; Pinter, P.J.Jr. (1983). Estimation of daily evapotranspiration from one time of day measurements. *Agri. Water Manage. 7*, 351-362

Jackson, R.D.; Idso, S.B.; Reginato, R.J.; Pinter, P.J. (1981). Canopy temperature as a crop water stress indicator. *Water Resour. Res. 17*, 1133–1138.

Jackson, R.D.; Kustas, W.P.; Choudhury, B.J. (1988). A reexamination of the crop water stress index. *Irrig Sci. 9,* 309-317.

Jackson, R.D.; Reginato, R.J.; Idso, S.B. (1977). Wheat canopy temperature: a practical tool for evaluating water requirements. *Water Resour. Res. 13*, 651-656.

Jia, L.; Su, Z.; van den Hurk, B.; Menenti, M.; Moene, A.; De Bruin, H.A.R.; Yrisarry, J.J.B.; Ibanez, M.; Cuesta, A. (2003). Estimation of sensible heat flux using the Surface Energy Balance System (SEBS) and ATSR measurements. *Phys. Chem. Earth. 28*, 75-88.

Jiang, G.; Li, Z.-L. (2008). Intercomparison of two BRDF models in the estimation of the directional emissivity in MIR channel from MSG1-SEVIRI data. *Opt. Express.* 16, 19310-19321.

Jiang, G.-M.; Li, Z.-L.; Nerry, F. (2006). Land surface emissivity retrieval from combined mid-infrared and thermal infrared data of MSG-SEVIRI. *Remote Sens. Environ,* 105, 326-340.

Jiang, L.; Islam, S. (1999). A methodology for estimation of surface evapotranspiration over large areas using remote sensing observations. *Geophys. Res. Lett. 26*, 2773-2776.

Jiang, L.; Islam, S. (2001). Estimation of surface evaporation map over southern Great Plains using remote sensing data. *Water Resour. Res. 37*, 329-340.

Jiang, L.; Islam, S. (2003). An intercomparison of regional latent heat flux estimation using remote sensing data. *Int. J. Remote Sens. 24,* 2221–2236.

Jiménez-Muñoz, J.C.; Sobrino, J.A. (2003). A generalized single-channel method for retrieving land surface temperature from remote sensing data. *J. Geophys. Res*, 108(D22), 4688, doi: 10.1029/2003JD003480.

Jonckheere, I.; Fleck, S.; Nackaerts, K.; Muys, B.; Coppin, P.; Weiss, M.; Baret, F. (2004). Methods for leaf area index determination. Part I: Theories, techniques and instruments. *Agric. For. Meteorol, 121*, 19-35.

Kairu, E.N.D.R. (1991). A review of methods for estimating evapotranspiration particularly those that utilize remote sensing. *GeoJournal 25*, 371-376.

Kalma, J.D.; Jupp, D.L.B. (1990). Estimating evaporation from pasture using infrared thermometry: evaluation of a one-layer resistance model. *Agric. For. Meteorol. 51*, 223-246.

Kalma, J. D., McVicar, T. R., and McCabe, M. F. (2008). Estimating land surface evaporation: a review of methods using remotely sensed surface temperature data. *Surveys in Geophys. 29*, 421-469

Klaassen, W.; Van Den Berg, W. (1985). Evapotranspiration derived from satellite observed surface temperatures. *J. Clim. Appl. Meteorol. 24*, 412-424.

Kohsiek, W.; Meijninger, W.M.L.; Debruin, H.A.R.; Beyrich, F. (2006). Saturation of the large aperture scintillometer. *Boundary-Layer Meteorol. 121*, 111-126.

Kohsiek, W.; Meijninger, W.M.L.; Moene, A.F.; Heusinkveld, B.G.; Hartogensis, O.K.; Hillen, W.C.A.M.; De Bruin, H.A.R. (2002). An extra large aperture scintillometer for long range applications. *Boundary-Layer Meteorol. 105*, 119-127.

Kotz, B.; Schaepman, M.; Morsdorf, F.; Bowyer, P.; Itten, K. Allgower, B. (2004). Radiative transfer modeling within a heterogeneous canopy for estimation of forest fire fuel properties. *Remote Sens. Environ, 92*, 332-344.

Kumar S.V.; Reichle, R.H.; Peters-Lidard C.D. (2008). A land surface data assimilation framework using the landinformation system: Description and applications. *Adv. Water Resour. 31*, 1419-1432.

Kustas, W.P.; Choudhury, B.J.; Moran, M.S.; Reginato, R.J.; Jackson, R.D.; Gay, L.W.; Weaver, H.L. (1989). Determination of sensible heat flux over sparse canopy using thermal infrared data. *Agric. For. Meteorol. 44*, 197–216.

Kustas, W.P.; Daughtry, C.S.T. (1990). Estimation of the soil heat flux/net radiation ratio from spectral data. *Agric. For. Meteorol. 49*, 205-223.

Kustas, W.P.; Goodrich, D.C.; Moran, M.S.; et al. (1991). An interdisciplinary field study of the energy and water fluxes in the atmosphere-biosphere system over semiarid rangelands: description and some preliminary results. *Bull. Am. Meteorol. Soc. 72*, 1683-1705.

Kustas, W.P.; Norman, J.M. (1997). A two-source approach for estimating turbulent fluxes using multiple angle thermal infrared observations. *Water Resour. Res. 3*3, 1495–1508.

Kustas, W.P.; Norman, J.M. (1999). Evaluation of soil and vegetation heat flux predictions using a simple two-source model with radiometric temperatures for a partial canopy cover. *Agric. For. Meteorol. 94*, 13–29.

Kustas, W.P.; Norman, J.M. (2000). A two-source energy balance approach using directional radiometric temperature observations for sparse canopy covered surfaces. *Agron. J. 92*, 847-854.

Kustas, W.P.; Norman, J.M. (1996). Use of remote sensing for evapotranspiration monitoring over land surfaces. *Hydrol. Sci. J. 41*, 495-516.

Kustas, W.P.; Norman, J.M.; Anderson, M.C.; French, A.N. (2003). Estimating subpixel surface temperatures and energy fluxes from the vegetation index-radiometric temperature relationship. *Remote Sens. Environ. 85*, 429–440.

Kustas, W.P.; Schmugge, T.J.; Humes, K.S.; Jackson, T.J.; Parry, R.; Weltz, M.A., Moran, M.S. Relationships between evaporative fraction and remotely sensed vegetation index and microwave brightness temperature for semiarid rangelands. J. Appl. Meteor. 1993, 32, 1781-1790.

Kustas, W.P.; Perry, E.M.; Doraiswamy, P.C.; Moran, M.S. (1994). Using satellite remote sensing to extrapolate evapotranspiration estimates in time and space over a semiarid rangeland basin. *Remote Sens. Environ. 49*, 275-286.

Lambin, E.F.; Ehrlich, D. (1996). The surface temperature-vegetation index space for land cover and land-cover change analysis. *Int. J. Remote Sens. 17*, 463-487.

Leblanc, S.G.; Chen, J.M.; White, H.P.; Latifvic, R.(2005). Canadawide foliage clumping index mapping from multi-angular POLDER measurements. *Can. J. Remote Sens, 31* (5), 364-376.

Lhomme, J.P.; Elguero, E. (1999). Examination of evaporative fraction diurnal behaviour using a soil-vegetation model coupled with a mixed-layer model. *Hydrol. Earth Syst. Sci. 3*, 259-270.

Li, F.; Lyons, T.J. (1999). Estimation of regional evapotranspiration through remote sensing. *J. Appl. Meteorol. 38*, 1644-1654.

Li, F.; Kustas, W.P.; Prueger, J.H.; Neale, C.M.U.; Jackson, T.J. (2005). Utility of remote sensing based two-source energy balance model under low- and high-vegetation cover conditions. *J. Hydrometeor. 6*, 878−891.

Li, Z.-L.; Jia, L.; Su, Z.; Wan, Z.; Zhang, R. (2003). A new approach for retrieving precipitable water from ATSR2 split-window channel data over land area. *Int. J. Remote Sens*, 24(24), 5095-5117.

Li, Z.-L.; Petitcolin, F.; Zhang, R.H. (2000). A physically based algorithm for land surface emissivity retrieval from combined mid-infrared and thermal infrared data. *Science in China (Series E)*, 43, 23-33.

Li, Z.-L.; Stoll, M.P.; Zhang, R.H.; Jia, L.; Su, Z. (2001). On the separate retrieval of soil and vegetation temperatures from ATSR2 data. *Science in China, Series D. 44* (2) 97-111

Li, Z.-L.; Tang, R.; Wan, Z.; Bi, Y.; Zhou, C.; Tang, B.; Yan, G.; Zhang, X. (2009). A Review of current methodologies for regional evapotranspiration estimation from remotely sensed data.

Sensors, *9*, 3801-3853.

Li, X. ; Ma, M. G. ; Wang, J. ; Liu, Q. ; Che, T. ; Hu, Z., et al. (2008). Simultaneous remote sensing and ground-based experiment in the Heihe river basin: scientific objectives and experiment design. *Prog. in Geography*, *23,* 897-914 (In Chinese).

Liang, S. (2004). *Quantitative Remote Sensing of Land Surfaces*. Wiley-Interscience.

Lucht, W. (1998). Expected retrieval accuracies of bidirectional reflectance and albedo from EOS-MODIS and MISR angular sampling. *J. Geophys. Res.*103, 8763-8778.

Lucht, W.; Roujean, J. L. (2000). Considerations in the parametric modeling of BRDF and albedo from multiangular satellite sensor observations. *Remote Sens. Rev.* 18, 343-379.

Luquet, D.; Vidal, A.; Dauzat, J.; Begue, A.; Oliosod, A.; Clouvel, P. (2004). Using directional TIR measurements and 3D simulations to assess the limitations and opportunities of water stress indices. *Remote Sens. Environ. 90*, 53–62

Mannstein, H. (1987). Surface energy budget, surface temperature, and thermal inertia. *Remote Sensing Applications in Meteorology and Climatology*, Vaughan, R.A. and Reidel, D. Eds. Dordrecht: Netherlands, (NATO ASI Ser. C: Math. Phys. Sci., vol. 201).

Margulis, S.A.; Entekhabi, D. (2003). Variational assimilation of radiometric surface temperature and reference-level micrometeorology into a model of the atmospheric boundary layer and land surface. *Mon. Wea. Rev. 131*, 1272-1288.

Margulis, S.A.; Kim, J.; Hogue, T. (2005). A comparison of the triangle retrieval and variational data assimilation methods for surface turbulent flux estimation. *J. Hydrometeor. 6*, 1063-1072.

Margulis, S.A.; McLaughlin, D.; Entekhabi, D.; Dunne, S. (2002). Land data assimilation and estimation of soil moisture using measurements from the Southern Great Plains 1997 Field Experiment. *Water Resour. Res. 38*, 35 1-18.

Massman, W.J. (1999). A model study of kB_H^{-1} for vegetated surfaces using 'localized nearfield' Lagrangian theory. *J. Hydrol. 223*, 27–43.

Mauser, W.; Stephan, S. (1998). Modelling the spatial distribution of evapotranspiration on different scales using remote sensing data. *J. Hydrol. 212-213*, 250-267.

McCabe, M.F.; Wood, E.F. (2006). Scale influences on the remote estimation of evapotranspiration using multiple satellite sensors. *Remote Sens. Environ. 105*, 271-285.

McLaughlin, D. (1995). Recent developments in hydrologic data assimilation. *Rev. Geophys. Supplement. July*, 977-984.

McLaughlin, D.; Zhou, Y.; Entekhabi, D.; Chatdarong, V. (2006). Computational Issues for Large-Scale Land Surface Data Assimilation Problems. *J. Hydrometeor. 7*, 494-510.

McMillin, L.M. (1975). Estimation of sea surface temperature from two infrared window measurements with different absorption. *J. Geophys. Res.* 80, 5113-5117.

Mecikalski, J.R.; Diak, G.R.; Anderson, M.C.; Norman, J.M. (1999). Estimating fluxes on continental scales using remotely sensed data in an atmospheric-land exchange model. *J. Appl. Meteorol. 38*, 1352-1369.

Mecikalski, J.R.; Mackaro, S.M.; Anderson, M.C.; Norman, J.M.; Basara, J.B. (2005). Evaluating the use of the Atmospheric Land Exchange Inverse (ALEXI) model in short-term prediction and mesoscale diagnosis. Conference on Hydrology, San Diego, CA, USA, pp.8-13.

Meijninger, W.M.L.; Hartogensis, O.K.; Kohsiek, W.; Hoedjes, J.C.B.; Zuurbier, R.M.; De Bruin, H.A.R. (2002). Determination of Area-Averaged Sensible Heat Fluxes with a Large Aperture Scintillometer over a Heterogeneous Surface – Flevoland Field Experiment. *Boundary-Layer Meteorol. 105*, 37-62.

Menenti, M.; Choudhury, B. (1993). Parameterization of land surface evaporation by means of location dependent potential evaporation and surface temperature range. Proceedings of IAHS conference on Land Surface Processes. *IAHS Publ. 212*, 561-568.

Menenti, M.; Jia, L.; Li, Z.-L.; Djepa, V.; Wang, J.; Stoll, M. P.; Su, Z.; Rast, M. (2001). Estimation of soil and vegetation temperatures with multiangular thermal infrared observations: the HEIHE, SGP'97, IMGRASS. *J. Geophys. Res*, *106* (D11), 11997-12010.

Menenti, M.; Jia, L.; Li, Z.-L. (2008). Multi-angular thermal infrared observations of terrestrial vegetation. In *Advances in Land Remote Sensing: S*ystem, Modeling, Inversion and Application, Springer Verlag, 51-93

Morel, P. (1985). Perspectives spatiales dans le domaine des recherches sur le climat. In CNES-Séminaire de Prospective, Deauville, France, 25-30.

Moran, M.S.; Clarke, T.R.; Inoue, Y.; Vidal, A. (1994). Estimating crop water deficit using the relationship between surface-air temperature and spectral vegetation index. *Remote Sens. Environ. 49*, 246-363.

Moran, M.S.; Jackson, R.D. (1991). Assessing the spatial distribution of evapotranspiration using remotely sensed inputs. *J. Environm. Qual. 20*, 525-737.

Moran, M.S.; Jackson, R.D.; Raymond, L.H.; Gay, L.W.; Slater, P.N. (1989). Mapping surface energy balance components by combining Landsat Thematic Mapper and ground-based meteorological data. *Remote Sens. Environ*. *30*, 77-87.

Moran, M.S.; Rahman, A.F.; Washburne, J.C.; Goodrich, D.C.; Weltz, M.A.; Kustas, W.P. (1996). Combining the Penman–Monteith equation with measurements of surface temperature and reflectance to estimate evaporation rates of semiarid grassland. *Agric. For. Meteorol. 80*, 87–109.

Monin, A.S.; Obukhov, A.M. (1954). Basic laws of turbulent mixing in the atmosphere near the ground. *Tr. Akad. Nauk SSSR Geofiz. Inst. 24*, 163−187.

Monteith, J.L. (1965). Evaporation and environment. *Symp. Soc. Explor. Biol. 19*, 205–234.

Monteith, J.L. (1973). *Principles of environmental physics*. Edward Arnold Press.

Monteith, J.L.; Unsworth, M.H. (1990). *Principles of Environmental Physics*. Edward Arnold, London, UK.

Moody, A.; Johnson, D.M. (2001). Land-surface phenologies from AVHRR using the discrete fourier transform. *Remote Sens. Environ*. *75*, 305-323.

Myneni, R.B.; Nemani, R.R.; Running, E.W. (1997). Algorithm for the estimation of global land cover, LAI and FPAR based on radiative transfer models. *IEEE Trans. Geosci. Remote Sens, 35*, 1380-1393.

Nemani, R.R.; Pierce, L.; Running, S.W. (1993). Developing satellite-derived estimates of surface moisture status. *J. Appl. Meteorol. 32*, 548-557.

Nemani, RR.; Running, S.W. (1989). Estimation of regional surface resistance to evapotranspiration from NDVI and thermal-IR AVHRR Data. *J. Appl. Meteorol. 28*, 276-284.

Nichols, W.E.; Cuenca, R.H. (1993). Evaluation of the Evaporative Fraction for Parameterization of the Surface Energy Balance. *Water Resour. Res. 29*, 3681-3690.

Nieuwenhuis, G.J.A.; Schmidt, E.A.; Tunnissen, H.A.M. (1985). Estimation of regional evapotranspiration of arable crops from thermal infrared images. *Int. J. Remote Sens. 6*, 1319-1334.

Nilson, T.; Kuusk, A. (1989). A reflectance model for the homogeneous plant canopy and its inversion. *Remote Sens. Environ.* 27, 157-167.

Norman, J.M.; Anderson, M.C.; Kustas, W.P. (2005). Are single-source, remote-sensing surface-flux models too simple? In Proceedings of the international conference on earth observation for vegetation monitoring and water management; G. D'Urso, M.A. Osann Jochum, Eds; American Institute of Physics: Naples, Italy, 2005; Volume 852, pp. 170–177.

Norman, J.M.; Anderson, M.C.; Kustas, W.P.; French, A.N.; Mecikalski, J.; Torn, R.; Diak, G.R.; Schmugge, T.J.; Tanner, B.C.W. (2003). Remote sensing of surface energy fluxes at 101-m pixel resolutions. *Water Resour. Res. 39*, SWC 9 1-19.

Norman, J.M.; Becker, F. (1995). Terminology in thermal infrared remote sensing of natural surfaces. *Agric. For. Meteorol. 77*, 153-166.

Norman, J.M.; Kustas, W.P.; Humes, K.S. (1995). A two-source approach for estimating soil and vegetation energy fluxes in observations of directional radiometric surface temperature. *Agric. For. Meteor. 77*, 263–293.

Norman, J.M.; Kustas, W.P.; Prueger, J.H.; Diak, G.R. (2000). Surface flux estimation using radiometric temperature: A dual temperature difference method to minimize measurement errors. *Water Resour. Res. 36*, 2263–2273.

Ottlé, C.; Vidal-Madjar, D. (1992). Estimation of land surface temperature with NOAA9 data. *Remote Sens. Environ*, 40(1), 27-41.

Owe, M.; Van De Griend, A.A. (1990). Daily surface moisture model for large area semiarid land application with limited climate data. *J. Hydrol. 121*, 119-132.

Paulson, C.A. (1970). The mathematical representation of wind speed and temperature profiles in the unstable atmospheric surface layer. *J. Appl. Meteorol. 9*, 857–861.

Pelgrum, H. (2000). Spatial Aggregation of Land Surface Characteristics. *PhD thesis, Wageningen University, Netherlands*, 33-39.

Petitcolin, F.; Nerry, F.; Stoll, M.P. (2002). Directional emissivity from AVHRR: Application to a region of northern Africa and the Iberian peninsula 1. Mapping emissivity in channel 3. *Int. J.*

Remote Sens. 23, 3443-3472.

Pinty, B.; Govron, N.; Widlowski, J.-L; Lavergne, T.; Verstraete, M.M. (2004). Synergy between 1-D and 3-D radiation transfer models to retrieve vegetation canopy properties from remote sensing data. *J. Geophys. Res. 109*, D21205

Pipunic, R.C.; Walker, J.P.; Western, A. (2008). Assimilation of remotely sensed data for improved latent and sensible heat flux prediction: A comparative synthetic study. *Remote Sens. Environ. 112*, 1295–1305.

Pokrovsky, O.; Roujean, J. L. (2002). Land surface albedo retrieval via kernel-based BRDF modeling: I. Statistical inversion method and model comparison. *Remote Sens. Environ.* 84, 100-119.

Prata, A.J.; Platt, C.M.R. (1991). Land surface temperature measurements from the AVHRR. *Proceedings of the 5th AVHRR data users conference*, 1991, June 25-28, Tromso, Norway, EUM P09, 443-438.

Price, J.C. (1980). The potential of remotely sensed thermal infrared data to infer surface soil moisture and evaporation. *Water Resour. Res. 16*, 787-795.

Price, J.C. (1982). On the use of satellite data to infer surface fluxes at meteorological scales. *J. Appl. Meteorol. 21*, 1111–1122.

Price, J.C. (1984). Land surface temperature measurements from the split window channels of the NOAA 7 AVHRR. *J. Geophys. Res.* D5, 7231-7237.

Price, J.C. (1990). Using spatial context in satellite data to infer regional scale evapotranspiration. *IEEE Trans. Geosci. Remote Sens. 28*, 940-948.

Prihodko, L.; Goward, S. N. (1997). Estimation of air temperature from remotely sensed surface observations. *Remote Sens. Environ, 60*, 335-346.

Priestley, C.H.B.; Taylor, R.J. (1972). On the Assessment of Surface Heat Flux and Evaporation Using Large-Scale Parameters. *Mon. Wea. Rev. 100*, 81-92.

Rabier, F.; Courtier, P.; Pailleux, J.; Talagrand, O.; Vasiljevic, D. (1993). A comparison between four-dimensional variational assimilation and simplified sequential assimilation relying on three-dimensional variational analysis. *Q. J. Roy. Meteorol. Soc. 119*, 845-880.

Raffy, M.; Becker, F. (1986). A stable iterative procedure to obtain soil surface parameters and fluxes from satellite data. *IEEE Trans. Geosci. Remote Sens. 33*, 327-333.

Rango, A. (1994). Application of remote sensing methods to hydrology and water resources. *Hydrol. Sci. J. 39*, 309-320.

Rasool, S.I. (1987). Potential of remote sensing for the study of global change. *Adv. Space Res. 7*, 6-99.

Reginato, R.J.; Jackson, R.D.; Pinter, P.J.JR. (1985). Evapotranspiration calculated from remote multispectral and ground station meteorological data. *Remote Sens. Environ. 18*, 75-89.

Reichle, R.H. (2008). Data assimilation methods in the Earth sciences. *Adv. Water Res. 31*, 1411-1418.

Reichle, R.H. (2002). Extended versus ensemble Kalman filtering for land data assimilation. *J. Hydrometeor. 3*, 728-740.

Reichle, R.H.; McLaughlin, D.B.; Entekhabi, D. (2002). Hydrologic Data assimilation with the ensemble Kalman filter. *Mon. Wea. Rev. 130*, 103-114.

Robinson, A.R.; Lermusiaux, P.F.J. (2000). Overview of data assimilation. *Harvard Reports in Physical/Interdisciplinary*. *62*, 1-13.

Rochdi, N.; Ad, M.; Chelle, R.F. (2006). An assessment of needles clumping within shoots when modeling radiative transfer within homogeneous canopies. *Remote Sens. Environ, 102*, 116-134.

Roerink, G.J.; Menenti, M. (2000). Time series of satellite data: development of new products. *NRSP-2 report* 99-33. pp 101.

Roerink, G.J.; Su, Z.; Menenti, M. (2000a). S-SEBI: a simple remote sensing algorithm to estimate the surface energy balance. Phys. Chem. Earth (B). 25, 147-157.

Roerink, G.J.; Menenti, M.; Verhoff, W. (2000b). Reconstructing cloud free NDVI composites using Fourier analysis of time series. Int. J. Remote Sens., 21, 1911-1917.

Roujean, J. L.; Leroy, M.; Deschamps, P. Y. (1992). A bidirectional reflectance model of the Earth's surface for the correction of remote sensing data. *J. Geophys. Res.* 97, 20,455-20,468.

Running, S.W.; Justice, C.; Salomonson, V.; Hall, D.; Barker, J.; Kaufman, Y.; Strahler, A.; Huete, A.; Muller, J.-P.; Vanderbilt, V.; Wan, Z.; Teillet, P. (1994). Terrestrial remote sensing science and algorithms planned for EOS/MODIS. *Int. J. Remote Sens* 17, 3587-3620.

Sánchez, J.M.; Kustas, W.P.; Caselles, V.; Anderson, M.C. (2008). Modelling surface energy fluxes over maize using a two-source patch model and radiometric soil and canopy temperature observations. *Remote Sens. Environ. 112*, 1130–1143.

Schmugge, T.J.; André, J.C. (1991). Land Surface Evaporation: Measurements and Parameterization. New York: *Springer-Verlag*.

Scott, N.A.; Chédin, A. (1981). A fast line-by-line method for atmospheric absorption computations: The Automatized Atmospheric Absorption Atlas. *J. Appl. Meteorol*, 20, 802-812.

Seguin, B. (1984). Estimation de I'evapotranspiration a partir de I'Infra-rouge thermIque. In Proceedings of 2nd Int. Coll. on spectral signatures of objects in remote sensing, Bordeaux, France, 427-446.

Séguin, B.; Assad, E.; Freteaud, J.P.; Imbernon, J.; Kerr, Y.; Lagouarde, J.P. (1987). Suivi du bilan hydrique à l'aide de la télédétection par satellite. Application au Sénégal, *Report to the EEC-DG8*, Bruxelles.

Seguin, B.; Baelz, S.; Monget, J.M.; Petit, V. (1982). Utilisation de la thermographie IR pour l'estimation de l'évaporation régionale. II: Résultats obtenus à partir de données satellites. *Agrono. 2*, 113–118.

Seguin, B.; Courault, D.; Guérif, M. (1994). Surface temperature and evapotranspiration: Application of local scale methods to regional scales using satellite data. *Remote Sens. Environ. 49*, 287-295.

Seguin, B.; Itier, B. (1983). Using midday surface temperature to estimate daily evaporation from satellite thermal IR data. *Int. J. Remote Sens. 4*, 371-383.

Sellers, P.J.; Hall, F.G.; Asrar, G.; Strebel, D.E.; Murphy, R.E. (1988). The first ISLSCP Field

Experiment (FIFE). *Bull. Amer. Meteorol. Soc.* 69(1), 22-27.

Sellers, P.J.; Heiser, M.D.; Hall, F.G. (1992). Relations between surface conductance and spectral vegetation indices at intermediate (100 m^2 to 15 km^2) length scales. *J. Geophys. Res. 97*, 19033-19059.

Seo, D.J.; Koren, V.; Cajina, N. (2003). Real-Time variational assimilation of hydrologic and hydrometeorological data into operational hydrologic forecasting. *J. Hydrometeor. 4*, 627-641.

Serafini, V.V. (1987). Estimation of the evapotranspiration using surface and satellite data. *Int. J. Remote Sens.* 8, 1547-1562.

Shuttleworth, W.J. (2007). Putting the "vap" into evaporation. *Hydrol. Earth Syst. Sci.11*, 210-244.

Shuttleworth, W.J.; Gurney, R.J. (1990). The theoretical relationship between foliage temperature and canopy resistance in sparse crops. *Q. J. Roy. Meteorol. Soc. 116*, 497–519.

Shuttleworth, W.J.; Gurney, R.J.; Hsu, A.Y.; Ormsby, J.P. (1989). FIFE: The variation in energy partition at surface flux sites Remote Sensing and Large-Scale Global Processes (Proceedings of the IAHS Third Int. Assembly, Baltimore, MD, May 1989). *IAHS Publ.* 186.

Shuttleworth, W.J.; Wallace, J.C. (1985). Evaporation from sparse crops - an energy combination theory. *Q. J. Roy. Meteorol. Soc. 111*, 839-855.

Singh, R.K.; Irmak, A.; Irmak, S.; Martin, D.L. (2008). Application of SEBAL Model for Mapping Evapotranspiration and Estimating Surface Energy Fluxes in South-Central Nebraska. *J. Irrig. Drain. E. 134*, 273-285.

Smolander, S.; Stenberg, P. (2003). A method to account for the shot scale clumping in coniferous canopy reflectance models. *Remote Sens. Environ*, *88*, 363-373.

Sobrino, J.A.; Li, Z.-L.; Stoll, M.P.; Becker, F. (1993). Determination of the surface temperature from ATSR data. *Proceedings of 25th International Symposium on Remote Sensing of Environment held in* Graz, Austria, April 4-8, pp II-19-II-109.

Sobrino, J.A.; Li, Z.-L.; Stoll, M.P.; Becker, F. (1994). Improvements in the split-window technique for land surface temperature determination. *IEEE Trans. Geosci. Remote Sens*. 32(2), 243-253.

Sobrino, J.A; Romaguera, M. (2004). Land surface temperature retrieval from MSG1-SEVIRI data. *Remote Sens. Environ*, 92, 247-254.

Soer, G.J.R. (1980). Estimation of regional evapotranspiration and soil moisture conditions using remotely sensed crop surface temperatures. *Remote Sens. Environ. 9*, 27-45.

Stisen, S.; Sandholt, I.; Nørgaard, A.; Fensholt, R.; Jensen, K.H. (2008). Combining the triangle method with thermal inertia to estimate regional evapotranspiration—Applied to MSG/SEVIRI data in the Senegal River basin. *Remote Sens. Environ. 112*, 1242-1255.

Su Z. (2001). A Surface Energy Balance System (SEBS) for estimation of turbulent heat fluxes from point to continental scale. In: Su, Z.; Jacobs, J.(Eds.), *Advanced Earth Observation—Land Surface Climate*. Publications of the National Remote Sensing Board (BCRS), USP-2. 01-02, 91–108.

Su, Z. (2002). The surface energy balance system (SEBS) for estimation of turbulent heat fluxes.

Hydrol. Earth Syst. Sci. 6, 85-99.

Su, Z. (2005). Hydrological applications of remote sensing. Surface fluxes and other derived variables–surface energy balance. In: M. Anderson, Editor, *Encyclopedia of Hydrol. Sens.* John Wiley and Sons.

Su, Z.; Li, X.; Zhou, Y.; Wan, L.; Wen, J.; Sintonen, K. (2003). Estimating areal evaporation from remote sensing. *Proc. IEEE Int., 2,* 1166-1168.

Sugita, M.; Brutsaert, W. (1991). Daily evaporation over a region from lower boundary layer profiles measured with radiosondes. *Water Resour. Res. 27*, 747-752.

Sun D.; Kafatos, M. (2007). Note on the NDVI-LST relationship and the use of temperature-related drought indices over North America. *Geophys. Res. Lett. 34,* L24406.

Sun, D.; Pinker, R.T. (2003). Estimation of land surface temperature from Geostationary Operational Environmental Satellite (GOES-8). *Journal of Geophysical Research*, 108(D11), 4326, doi: 10.1029/2002JD002422.

Talagrand, O. (1997). Assimilation of observations, an introduction. *J. Meteor. Soc. 75*, 191-209.

Tang, B.H.; Li, Z.-L. (2008a). Retrieval of land surface bidirectional reflectivity in the mid-infrared from MODIS channels 22 and 23. *Int. J. Remote Sens.* 29, 4907-4925.

Tang, B. H.; Li, Z.-L. (2008b). Estimation of instantaneous net surface longwave radiation from MODIS cloud-free data. *Remote Sens. Environ, 112,* 3482-3492.

Tang, B. H. ; Li, Z.-L.; Zhang, R. H. (2006). A direct method for estimating net surface shortwave radiation from MODIS data. *Remote Sens. Environ , 103,* 115-126.

Timmermans, W.J.; Kustas, W.P.; Anderson, M.C.; French, A.N. (2007). An intercomparison of the Surface Energy Balance Algorithm for Land (SEBAL) and the Two-Source Energy Balance (TSEB) modeling schemes. *Remote Sens. Environ. 108,* 369–384.

Thunnissen, H.A.M.; Nieuwenhuis, G.J.A. (1990). A simplified method to estimate regional 24-h evapotranspiration from thermal infrared data. *Remote Sens. Environ. 31,* 211-225.

Todd, R.W.; Evett, S.R.; Howell, T.A. (2000). The Bowen ratio-energy balance method for estimating latent heat flux of irrigated alfalfa evaluated in a semi-arid, advective environment. *Agric. For. Meteorol. 103,* 335–348.

Ulivieri, C.; Castronouvo, M.M.; Francioni, R.; Cardillo, A. (1992). A SW algorithn for estimating land surface temperature from satellites. *Advance Space Res.*14(3), 59-65.

Uppala, S. M.; Kallberg, P. W.; Simmons A. J. et al.. (2005). The ERA-40 re-analysis. *Quart. J. R. Meteorol. Soc.* 131, 2961-3012.

Van den Hurk, B. (2001). Energy balance based surface flux estimation from satellite data, and its application for surface moisture assimilation. *Meteorol. Atmos. Phys. 76*, 43-52.

Venturini, V.; Bisht, G.; Islam, S.; Jiang, L. (2004). Comparison of evaporative fractions estimated from AVHRR and MODIS sensors over South Florida. *Remote Sens. Environ. 93*, 77–86.

Verhoef, A.; De Bruin, H.A.R.; Van Den Hurk, B.J.J.M. (1997). Some practical notes on the parameter kB^{-1} for sparse vegetation. *J. Appl. Meteorol. 36*, 560–572.

Vidal, A. (1991). Atmospheric and emissivity correction of land surface temperature measured from satellite using ground measurements or satellite data. *Int. J. Remote Sens*, 12, 2449-2460.

Walter, J.-M.N.; Fournier, R.A.; Soudani, K.; Meyer, E. (2003). Integrating clumping effects in forest canopy structure: an assessment through hemispherical photographs. *Can. J. Remote Sens***,** *29* (3), 388-410.

Wan, Z. (2008). New refinements and validation of the MODIS land-surface temperature/emissivity products. *Remote Sens. Environ.*112, 59-97.

Wan, Z.; Dozier, J. (1996). A generalized split-window algorithm for retrieving land-surface temperature from space. *IEEE Trans. Geosci. Remote Sens*, Vol.34, No.4, 892-905.

Wang, K.; Li, Z.; Cribb, M. (2006). Estimation of evaporative fraction from a combination of day and night land surface temperatures and NDVI: A new method to determine the Priestley-Taylor parameter. *Remote Sens. Environ. 102*, 293-305.

Wang, W.-M.; Li, Z.-L. Scaling directional gap probability over heterogeneous land surface: influences on the estimates of component temperatures. Remote Sensing of Environment (submitted in 2008).

Wang, W.-M.; Li, Z.-L.; Su, H.-B. (2007). Comparison of leaf angle distribution functions: effects on extinction coeffcient and fraction sunlit foliage. *Agric. For. Meteorol*, *143*, 106-122.

Wanner, W.; Li, X.; Strahler, A. H. (1995). On the derivation of kernels for kernel-driven models of bidirectional reflectance. *J. Geophys. Res.* 100, 21,077-21,089.

Webb E. K. (1970). Profile relationships: The log-linear range, and extension to strong stability. *Q. J. Roy. Meteor. Soc. 96*, 67-90.

Weigand, C.L.; Bartholic, J.F. (1970). Remote sensing in evapotranspiration research on the Great Plains. In the Proceedings of Great Plains Agricultural Council Evapotranspiration Seminar, Texas, USA; pp. 137-180.

Weiss, M.; Baret, F. (1999). Evaluation of canopy biophysical variable retrieval performances from the accumulation of large swath satellite data. *Remote Sens. Environ*, *70*, 293−306.

Weiss, M.; Baret, F.; Smith, G.J.; Jonckheere, I.; Coppin, P. (2004). Review of methods for in situ leaf area index (LAI) determination Part II: Estimation of LAI, errors and sampling. *Agric. For. Meteorol*, *121*, 37-53

Wetzel, P.J.; Atlas, D.; Woodward, R. (1984). Determining soil moisture from geosynchronous satellite infrared data: A feasibility study. *J. Clim. Appl. Meteorol. 23*, 375-391.

Whitehead, V.S.; Johnson, W.R.; Boatright, J.A. (1986). Vegetation assessment using a combination of visible, near-IR, and thermal-IR AVHRR data. *IEEE Trans. Geosci. Remote Sens*. *1*, 107-112.

Wood, E.F.; Su, H.; McCabe, M.; Su, Z. (2003). Estimating Evaporation from Satellite Remote Sensing. Paper presented at the *IGARSS*. *7*, 21-25.

Zhang, L.; Lemeur, R. (1995). Evaluation of daily evapotranspiration estimates from instantaneous measurements. *Agric. For. Meteorol. 74*, 139-154.

Županski, D.; Mesinger, F. (1995). Four-Dimensional variational assimilation of precipitation data. *Mon. Wea. Rev. 123*, 1112-1127.